Stratocumulus Precipitation Properties over the Southern Ocean Observed from Aircraft during the SOCRATES campaign

Litai Kang[1], Roger T Marchand[2], and Robert Wood[2]

[1]Department of Atmospheric Sciences, University of Washington
[2]University of Washington

August 24, 2023

Abstract

Precipitation plays an important role in various processes over the Southern Ocean (SO), ranging from the hydrological cycle to cloud and aerosol processes. The main objective of this study is to characterize SO precipitation properties. We use data from the Southern Ocean Clouds Radiation Aerosol Transport Experimental Study (SOCRATES), and leverage observations from airborne radar, lidar, and in situ probes. For the cold-topped clouds (cloud-top-temperature $< 0°C$), the phase of precipitation with reflectivity > 0 dBZ is predominately ice, while reflectivity $<$ -10 dBZ is predominately liquid. Liquid-phase precipitation properties are retrieved where radar and lidar are zenith-pointing. The power-law relationships between reflectivity (Z) and rain rate (R) are developed, and the derived Z-R relationships show vertical dependence and sensitivity to the intermediate drops (diameters between 10-40 μm). Using derived Z-R relationships, reflectivity-velocity (ZV) retrieval method, and a radar-lidar retrieval method, we derive rain rate and other precipitation properties. The retrieved rain rate from all three methods shows good agreement with in-situ aircraft estimates. Rain rate features the prevalence of light precipitation ($<$0.1 mm hr^{-1}). We examine the vertical distribution of precipitation properties, and found that rain rate, precipitation number concentration, precipitation liquid water all decreases as one gets closer to the surface, while precipitation size and width increases. We also examine how cloud base rain rate (R_{CB}) depends on cloud depth (H) and aerosol concentration (N_a) for particles with diameter greater than 70nm, and we find a linear relationship between R_{CB} and $H^{3.6}N_a^{-1}$.

Stratocumulus Precipitation Properties over the Southern Ocean Observed from Aircraft during the SOCRATES campaign

L. Kang[1], R. T. Marchand [1], and R. Wood[1]

[1] Department of Atmospheric Sciences, University of Washington, Seattle, Washington, USA

Corresponding author: Litai Kang (kanglt@uw.edu)

†Additional author notes should be indicated with symbols (current addresses, for example).

Key Points:

- Liquid-phase precipitation retrievals show good agreement with in situ observations and feature the prevalence of light rain
- Reflectivity to rain rate relationships are developed, showing vertical dependence and sensitivity to the intermediate-sized drops
- The below-cloud precipitation phase with radar reflectivity > 0 dBZ is mostly ice, while radar reflectivity < -10 dBZ is mostly liquid

Abstract

Precipitation plays an important role in various processes over the Southern Ocean (SO), ranging from the hydrological cycle to cloud and aerosol processes. The main objective of this study is to characterize SO precipitation properties. We use data from the Southern Ocean Clouds Radiation Aerosol Transport Experimental Study (SOCRATES), and leverage observations from airborne radar, lidar, and in situ probes. For the cold-topped clouds (cloud-top-temperature < 0°C), the phase of precipitation with reflectivity > 0 dBZ is predominately ice, while reflectivity < -10 dBZ is predominately liquid. Liquid-phase precipitation properties are retrieved where radar and lidar are zenith-pointing. The power-law relationships between reflectivity (Z) and rain rate (R) are developed, and the derived Z-R relationships show vertical dependence and sensitivity to the intermediate drops (diameters between 10-40 μm). Using derived Z-R relationships, reflectivity-velocity (ZV) retrieval method, and a radar-lidar retrieval method, we derive rain rate and other precipitation properties. The retrieved rain rate from all three methods shows good agreement with in-situ aircraft estimates. Rain rate features the prevalence of light precipitation (<0.1 mm hr^{-1}). We examine the vertical distribution of precipitation properties, and found that rain rate, precipitation number concentration, precipitation liquid water all decreases as one gets closer to the surface, while precipitation size and width increases. We also examine how cloud base rain rate (R_{CB}) depends on cloud depth (H) and aerosol concentration (N_a) for particles with diameter greater than 70nm, and we find a linear relationship between R_{CB} and $H^{3.6}\ N_a^{-1}$.

Plain Language Summary

Precipitation plays an important role over the Southern Ocean (SO), such as transferring water from air to ocean, and affect cloud and aerosols (tiny airborne particles). The goal of this study is to characterize SO precipitation properties using aircraft data. Aircraft had instruments that can count the number of droplets, as well as lidar and radar, which are remote sensing devices that use laser light and microwave waves respectively to detect objects. Using information from lidar, we can distinguish precipitation phase, and we found that ice precipitation is more frequent when observed radar reflectivity is larger than certain threshold. We derived relationships between rain rate and radar variable that can be used for future research. We also calculated precipitation properties and found our results compares well with direct measurements from the aircraft. Rain rate we calculated features the prevalence of light precipitation. We also studied how precipitation properties very vertically, and found that as one gets closer to the surface, there is a decrease in precipitation number and water, while there is an increase in the size overall. We also found that rain rate depends on how thick the clouds are and on the number of aerosols.

1 Introduction

Surrounding Antarctica, the Southern Ocean (SO) is the second smallest of the five ocean basins, yet it plays an outsized role in the climate system. The SO is estimated to account for about 75% of the oceanic heat uptake and about 30-40% of the carbon uptake (Frölicher et al., 2015; Khatiwala et al., 2009), and thus act as a strong buffer against climate change. Due to the lack of anthropogenic aerosols, the SO is also a pristine environment, and it has been argued that SO observations can be used as a present-day proxy for pre-industrial conditions as regards trying to constrain anthropogenic aerosol effects (Hamilton et al., 2014; McCoy et al., 2020), which remain a large source of uncertainty in the climate projections (Lee et al., 2016; Bellouin et al., 2020). More generally, SO clouds, especially low clouds, also have attracted much research interest in recent years because of their importance to the global radiative energy budget (Trenberth and Fasullo, 2010; Bodas-Salcedo et al., 2016; Cesana et al., 2022) as well as global cloud feedbacks and global climate sensitivity (Tan et al., 2016; Zelinka et al., 2020; Mülmenstädt et al., 2021).

Precipitation impacts stratocumulus behavior via complex feedbacks that operate on both macrophysical and microphysical scales (Wood, 2012), and has been found to be a key player in the transition of stratocumulus regimes, from closed cells to open cells, and the maintenance of open cells, at least in subtropical stratocumulus (Wang and Feingold, 2009; Yamaguchi and Feingold, 2015; Smalley et al., 2022). Moreover, recent studies highlight the importance of precipitation formation as a dominant sink of cloud condensation nuclei and its control on the cloud droplet number over the SO (McCoy et al., 2020; Kang et al., 2022). Despite the importance of precipitation in low clouds, many climate models and reanalysis data struggle to represent accurately precipitation, including over the SO (Zhou et al., 2021). Mülmenstädt et al., (2021) point out that precipitation biases persist in CMIP6 models, with warm clouds precipitating too frequently, thus shortening the cloud lifetime and underestimating their cooling effect. This problem is especially pernicious for the SO because the error grows in importance, with a reduction in mixed-phase clouds as the climate warms (Bjordal et al., 2020).

Due to the remoteness of SO and a general lack of surface and in situ observations, satellite observations have long been an indispensable tool to study SO precipitation. Arguably the best available source of satellite data on SO precipitation rates is CloudSat (W-band radar), which has greater sensitivity to light precipitation than passive sensors (Tansey et al., 2022, Eastman et al., 2019). CloudSat has provided an unprecedentedly broad picture of SO precipitation: Ellis et al. (2009) showed that the precipitation occurrence frequency peaks around 50°-60°S; Mitrescu et al. (2010) found that the SO has a high occurrence of very light precipitation with rain rates smaller than 1 mm h^{-1} having a frequency of 15%; Mace and Avey (2017) using both CloudSat and Moderate Resolution Imaging Spectroradiometer (MODIS) data found that precipitation processes in SO warm clouds vary seasonally with a stronger precipitation susceptibility to cloud droplet number in winter. Although compared to other satellite measurements, CloudSat better detects light precipitation and is better able to determine the rain rate, CloudSat is nonetheless affected by ground clutter which severely corrupts the reflectivity measurements within about 750 m of the surface (Marchand et al.,2008). CloudSat precipitation retrievals are also largely limited to situations where the measured near-surface (750 to 1000m) reflectivity is larger than -15 dBZ (Haynes et al., 2009), although the precipitation is often observed falling for SO clouds with reflectivity factors less than -15 dBZ (e.g., Mace and Protat 2018). As shown by Tansey et al. (2022), who evaluated CloudSat retrievals using surface precipitation measurements during the Macquarie Island Cloud Radiation Experiment (MICRE), the CloudSat 2C-Precip-Column product misses most precipitation with a precipitation rate less than 0.5 mm hr^{-1}. In addition, CloudSat radar reflectivity measurements provide very limited information regarding the phase of the precipitation. The current operational CloudSat precipitation products categorize precipitation into liquid, snow, or mixed phase based largely on temperature profiles extracted from ECMWF analysis and identifying melting layers, rather than any directly measured quantity.

In the face of biases and uncertainty in satellite retrievals and modeling, precipitation observations from multiple sources such as islands, ships, and aircraft provide us with an important opportunity to obtain a more detailed view of SO precipitation. Such precipitation observations were made in several recent collaborative field campaigns (McFarquhar et al.,2021), including the aforementioned Macquarie Island Cloud Radiation Experiment (MICRE) during 2016-2018, the Clouds Aerosols Precipitation Radiation and atmospheric Composition over the Southern Ocean (CAPRICORN) campaign in 2016 and 2018, the Measurements of Aerosol, Radiation, and Clouds over the Southern Ocean (MARCUS) campaign during 2017-2018, and the Southern Ocean Cloud Radiation and Aerosol Transport Experimental Study (SOCRATES) during Jan-Feb 2018. For example, Tansey et al. (2022) created a 1-year "blended" surface precipitation dataset (which combines W-band radar, tipping buck and disdrometer data) for MICRE and used these data to study the diurnal, synoptic and seasonal variability of near-surface precipitation. These authors found that total accumulation was comprised of about 74% rain, 16% ice or mixed phase precipitation, and 10% small particle precipitation. In a study based on the CAPRICORN datasets. Montoya Duque et al. (2022), applied a K-means clustering technique to radiosonde data to classify the atmosphere into seven thermodynamic clusters, and found that the highest occurrence of surface precipitation was associated with warm frontal clusters and high-latitude cyclone clusters(poleward of the polar front near cyclones), with warm rain dominating in the former and the largest fraction of snow in the latter. Shipborne precipitation observations from CAPRICORN have also been included along with observations from other research vessels in the Ocean Rain and Ice-Phase Precipitation Measurement Network (OceanRAIN), the first global and comprehensive along-track in-situ water cycle surface reference dataset (Klepp et al., 2018). Protat et al. (2019a,b) used OceanRAIN data to investigate discrepancies among satellite products at high latitudes and found large latitudinal and convective-stratiform variability in the drop size distribution (DSD). Protat et al. (2019a) pointed out that the Southern hemisphere high latitudes stood out as regions with a systematically higher frequency of occurrence of light precipitation with rates < 1 mm h^{-1} and difference in the shape parameter μ in the precipitation drop size distribution (DSD), with high-latitude and midlatitude μ ranging from -1 to 1, which is lower than the assumed μ of 2 or 3 in the Global Precipitation Measurement Mission (GPM) rainfall algorithms (Grecu et al., 2016; Seto et al., 2013). Protat et al. (2019b) found that the Southern Hemisphere high latitude (−67.5°S to −45°S), along with Northern Hemisphere polar latitude bands, stood out with a fundamentally different relationship between radar observables and rainfall properties, such as radar reflectivity to rain rate (Z-R) relationship, mainly because of much lower rain rates over the SO, suggesting that specific relationships are needed for these regions.

In this study, we use data collected during SOCRATES to study the precipitation properties of summertime SO stratocumulus, leveraging observations from airborne W-band HIAPER Cloud Radar (HCR), High Spectral Resolution Lidar (HSRL), and in situ probes. In particular we examine occurrence of liquid and ice phase precipitation, and for liquid precipitation we derived precipitation properties such as rain rate, using a hierarchy of retrieval methods from simple Z-R relationships to more complex radar reflectivity-velocity retrieval (ZV retrieval) and radar-lidar retrievals. We also apply the precipitation observations and retrievals to study the in-and-below cloud precipitation properties and rain rate dependence on cloud depth and aerosol concentration.

This paper is organized as follows: Section 2 introduces the datasets, instruments, as well as the analysis and retrieval methods used in this study. Section 3 provides a campaign overview and discusses phase partitioning. Section 4 examines Z-R relationships and precipitation retrievals and compares these remote sensing data to in situ measurements. Section 5 provides a statistical summary of the precipitation properties, and Section 6 explores the relationship of stratocumulus rain rate with cloud depth and aerosol concentration, ending with conclusions in Section 7.

2 Data and Methods

In this section we introduce the data and methods that we use to characterize in-and-below cloud precipitation properties. Section 2.1 describes the SOCRATES campaign sampling strategies, remote sensors (W-band Cloud Radar, HCR, and High Spectral Resolution Lidar, HSRL), and in situ instruments. Section 2.2 describes how we use in situ data to analyze in-cloud and below-cloud precipitation properties, as well as how we estimate Z-R relationships. In section 2.3, we describe reflectivity-velocity (ZV) and radar-lidar retrievals.

2.1 Instrumentation and data

In this study, we use data collected during the SOCRATES campaign to study the precipitation properties of stratocumulus. The SOCRATES campaign happened in January-February 2018 (McFarquhar et al., 2021), when the NSF/NCAR Gulfstream GV aircraft conducted 15 research flights over the SO. After taking off from Hobart (Tasmania), the aircraft typically flew south at high altitude and then descended to just above cloud top for several 10's of minutes, before heading back towards Hobart. On the return, the aircraft would descend into low cloud and sample aerosols, clouds, and precipitation with a repeating series of activities that included in-, below-, and above-cloud level legs (where the aircraft flew at a nearly fixed altitude), as well as sawtooth legs (where the aircraft ascended or descended through the cloud layer). Supplementary Figure S1 shows a schematic of the typical flight, as well as the 15 flight tracks flown during SOCRATES.

To characterize in-and-below cloud precipitation properties, we leverage observations from both in situ probes and remote sensors. Table 1 gives a summary of the instruments we use in this study, along with a primary reference for each instrument. We describe how these in situ probe data are used in Section 2.2.

Table 1. Instruments

Instruments	Measurements	References
Cloud Droplet Probe (CDP)	Size and concentration of hydrometeors with a diameter between 2-50 μm	Lance et al. (2010) https://data.eol.ucar.edu/dataset/552.002
Two-Dimensional Stereo probe (2DS)	Size and concentration of hydrometeors with a diameter between 10-1280 μm	Wu and McFarquhar (2019) https://data.eol.ucar.edu/dataset/552.047
Ultra-High-Sensitivity Aerosol	Aerosols with dry diameters between 60 and 1,000 nm	DMT(2013); Sanchez et al. (2021) https://data.eol.ucar.edu/dataset/552.002

Spectrometer (UHSAS)		
HIAPER Cloud Radar (HCR)	Reflectivity, Doppler velocity, Spectral width, Signal to noise ratio, etc.	Vivekanandan et al. (2015) https://data.eol.ucar.edu/dataset/552.034
High Spectral Resolution Lidar (HSRL)	Backscatter coefficient, Particle Linear Depolarization Ratio, Extinction coefficient, etc.	Eloranta (2005) https://data.eol.ucar.edu/dataset/552.034

Note: For both CDP and 2DS, data is available at 1Hz temporal resolution. CDP data can be found in SOCRATES Navigation, State Parameter, and Microphysics Flight-Level Data. This study uses version 1.4 of this dataset. This study uses version 1.1 of the 2DS dataset. The radar and lidar moments data version 3.1 were processed by NCAR/EOL and 2 Hz (0.5 seconds) temporal resolution and 19 meters range vertical resolution. The operational specifications of HCR and HSRL is available at https://data.eol.ucar.edu/datafile/nph-get/552.034/readme_HCR_HSRL_SOCRATES_2Hz_v3.1.pdf.

Remote sensors include a 94-GHz W-band HIAPER Cloud Radar(HCR) (Vivekanandan et al., 2015) and a 532-nm High Spectral Resolution Lidar (HSRL) (Eloranta, 2005). Based on radar and lidar moments data, we will use retrieval techniques to derive precipitation properties, as detailed in section 2.3. HCR and HSRL were deployed in previous campaigns, such as CSET (e.g. Schwartz et al., 2019). The radar and lidar data were processed by NCAR/EOL at 2 Hz (0.5 seconds) temporal resolution and have 19 m vertical range resolution. A description of the NCAR/EOL data processing and corrections are given in readme files that are distributed with the data (with link in the acknowledgement). This includes a correction of radial velocity for platform motion following Romatschke et al. (2021), in which corrections are applied to the nadir and zenith pointing data separately. For nadir pointing data, radial velocity was corrected following Ellis et al. (2019), where for radial velocity of the surface (assumed to be 0 m/s) is used as a reference to correct the data with a running 3rd degree polynomial filter. A similar method is applied to the zenith pointing data, which are the focus of this paper. But for the zenith pointing data, instead of assuming zero velocity of surface, it is assumed that the cloud top velocities from zenith pointing times are similar to those of the neighboring nadir pointing times. Specifically, cloud top velocities are first calculated for both the nadir pointing data and zenith pointing data, then the difference of the two is used to correct the bias in the zenith pointing velocity data. Figure S2 shows an example of the zenith pointing velocity fields before and after the correction, and Figure S3 shows the averaged nadir pointing and zenith pointing velocity profiles from RF13, demonstrating that correction resulted in consistent velocity profile between nadir pointing data and zenith pointing times.

2.2 In situ Measurements

2.2.1 Droplet size distribution

This study uses in situ measurements mainly from two particle-sizing-instruments: a Cloud Droplet Probe (CDP) and a Two-Dimensional Stereo probe (2DS) as listed in Table 1. We focus on in situ measurement from these legs (as marked in Figure S1): below-cloud level legs, in-cloud level legs, and sawtooth legs (which are further divided into top-half of the cloud, bottom-half of the cloud, and the below-cloud portion as described below). These in situ measurements will be used to derive reflectivity to rain rate relationships (Z-R) relationships (section 4.1), to validate the precipitation retrievals (section 4.3), and to study in-and-below cloud precipitation properties (section 5).

We combine measurements from CDP and 2DS to create combined droplet size distribution (DSD) by using CDP measurements for bins with a diameter < 25μm and 2DS for bins > 50 μm. For drops in the intermediate size range (25–50 μm) we take the larger values of the two probes. After combining the DSD from two probes, we further averaged DSD for different regions and flight segments. Specifically, we examine the top half of the cloud layer from sawtooth legs; the bottom half of the cloud layer from sawtooth legs; the below-cloud portion of the sawtooth legs; the below-cloud level legs in 20s intervals; and in-cloud level legs in 10s intervals. For the purpose of averaging the in-situ data into these categories, the define the aircraft as in-cloud when then liquid water content greater than 0.03 g m^{-3} (Wood et al., 2011; Kang et al., 2021). Because of the limited sampling volumes of the probes, even with averaging, there can be gaps (and large variability) in the DSD distribution for large particles (where the concentrations are sufficient low that the probes become increasingly unlikely to observe these particles). As needed, we fill gaps in the DSD by fitting an exponential curve following Comstock et al. (2004) and extrapolate DSD for larger particles (out to a diameter of 2000 μm).

2.2.2 Precipitation properties

Precipitation properties are derived using the DSD. For different segments, we calculated rain rate (liquid water flux) as:

$$R = 3600 * \frac{\pi}{6}\rho_w \int_{D_{min}}^{\infty} n(D)\, D^3\, v_f(D) dD \tag{1}$$

where ρ_w is the density of liquid water (1000 kg m^{-3}), D is the diameter in of m, 3600 is a scaling factor to convert the unit from kg m^{-2} s^{-1} to mm hr^{-1}, and $v_f(D)$ is the terminal fall velocity (unit of m s^{-1}) of droplets in the range from D to $D+dD$, and $n(D)$ is the drop size distribution (with units of m^{-3} mm^{-1}) . We use the terminal fall velocity model of Beard (1976) for $v_f(D)$ term. D_{min} is the lower limit for the integration, and except where stated otherwise is set to 40 μm. In Section 4.1, we test the importance of smaller droplets with diameter smaller than 40 μm on the liquid water flux(LWF_{total}).

Similarly, precipitation number (N_{precip}) is calculated as:

$$N_{precip} = \int_{D_{min}}^{\infty} n(D)dD \tag{2}$$

Precipitation liquid water content (LWC_{precip}) is calculated as:

$$LWC_{precip} = \frac{\pi}{6}\rho_w \int_{D_{min}}^{\infty} n(D)\, D^3 dD \tag{3}$$

Precipitation liquid water content weighted mean diameter (D_{precip}), which can be thought of as diameter at which half of LWC_{precip} is below and half is above, is calculated as:

$$D_{precip} = \frac{\int_{D_{min}}^{\infty} n(D)\, D^4 dD}{\int_{D_{min}}^{\infty} n(D)\, D^3 dD} \tag{4}$$

Precipitation liquid water content weighted width (σ_{precip}) is calculated as:

$$\sigma_{precip} = \sqrt{\frac{\int_{D_{min}}^{\infty} n(D)\, D^3 (D - D_{precip})^2 dD}{\int_{D_{min}}^{\infty} n(D)\, D^3 dD}} \tag{5}$$

2.2.3 Z-R relationships

To estimate the Z-R relationships from in situ measurements, we calculated radar reflectivity Z and rain rate R, respectively from the in situ droplet size distributions (DSD). Rain rate is calculated as equation 1. Reflectivity is proportional to the sixth moment of the DSD:

$$Z = \int_0^{\infty} n(D)\, D^6\, \gamma_f(D) dD \tag{6}$$

where $n(D)\; dD$ gives number concentrations from diameter D to $D+dD$, $\gamma_f(D)$ is the Mie-to-Rayleigh backscatter ratio (shown in Figure S4, which is the ratio of the backscatter efficiency of Mie scattering for W-band (94-GHz), calculated using the <u>miepython</u> package based on Wiscombe

(1979), and backscatter efficiency of Rayleigh scattering (Bohren & Huffman, 1983). With calculated reflectivity and rain rate from the in situ DSD, the Z-R relationship assumes a traditional power-law of the form:

$$Z = aR^b \tag{7}$$

Where a and b are coefficients, and Z is the independent variable. Equation 7 can also be rearranged as $R = (Z/a)^{1/b}$, which can be used to derive R based on Z observations. Coefficients a and b can be estimated using the least-squares regression in log space following Comstock et al. (2004):

$$logR = \frac{1}{b}\,(-\,log\ a\ +\ log\ Z) \tag{8}$$

We estimated the uncertainty in estimated exponents b and intercepts a that are based on in situ data using bootstrapping. Note that in section 4.1, we also estimated Z-R relationship based on radar observed reflectivity factor and rain rate from radar-lidar retrieval (more details in section 2.3.3), where we use moving blocks bootstrapping method following Wilks (1997) to estimate uncertainty in a and b coefficients, with a block length that close to the enfolding length.

2.3 Precipitation Retrievals based on remote sensors

Precipitation retrievals described in this section use the zenith-pointing data collected when the aircraft was flying level-legs below the cloud. To illustrate, Figure 1a shows the flight track altitude and measured radar reflectivity for research flight 13 (RF13). In panel (a), the potions of the flight track which feature below-cloud-level legs are colored green. Figure 1b-f shows the radar and lidar data in more detail, for the below-cloud level leg starting from 03:40 UTC, which is marked by the grey shading in Figure 1a. In general, retrievals undertaken for below-cloud level legs have the advantage that the zenith pointing lidar data allows one to determine the position of cloud base, as well as providing measurements of the backscatter (Figure 1c) and depolarization ratio (Figure 1d) of the precipitation that has fallen from the cloud and can be used to determine the precipitation phase. We describe the retrieval process in the three subsections that follow: (1) determine the cloud boundaries; (2) determine the phase of precipitation; (3) determine the liquid precipitation microphysical properties (such as the rain rate).

2.3.1 Determine the cloud boundaries

To determine the cloud base, we use the lidar backscatter coefficient β (e.g. Figure 1c) and define the cloud base as the altitude where β first exceeds a threshold of 0.0001 m^{-1} sr^{-1}. The black dots in Figure 1c show the cloud base identified using this threshold. Cloud top for our analysis is based on the radar reflectivity data, which has already been masked for significant detections (above the instrument noise floor). The cloud top is taken simply as the maximum height with a valid reflectivity echo below 3km, as marked by grey dots in Figure 1b-f.

2.3.2 Determine the phase of precipitation below cloud base

With the cloud boundaries identified, the next step is to determine the phase of the precipitation falling from the clouds. Following Mace and Protat (2018), we determine the precipitation phase using the lidar particle linear depolarization ratio (PLDR) (e.g., Figure 1d). The basic concept is that the lidar emits linearly polarized light, and scattering by spherical particles (e.g. liquid drops) does not change the polarization state of the light and thus generates little PLDR, while scattering from non-spherical particles (e.g. ice particles) creates significant depolarization and thus generates measurable increase in PLDR. In this study, for each lidar column, we examined the median of the PLDR over the vertical interval between cloud base to the first useable lidar range gate. For clouds with a cloud top temperature greater than 0, that is for warm clouds whose precipitation must be liquid, we find the below-cloud base PLDR values to be less than 0.03 about 90% of the time, and to be above 0.05 less than 1% of the time(see Figure S5 for overall statistics and Figure S6 for an example case). Thus, for cooler cold-topped clouds (which might precipitate ice), we define the precipitation to be liquid phase when the median PLDR < 0.03; ice precipitation when PLDR > 0.05; and ambiguous phase with PLDR values in between.

2.3.3 Liquid Precipitation retrieval

After determining the cloud base and precipitation phase, we can use a hierarchy of retrieval methods with increasing complexity to derive the precipitation microphysical properties, starting from (1) a simple Z-R relationship approach where only one variable, the radar reflectivity, Z, is available to derive the rain rate, to (2) a ZV retrieval following Mace et al. (2002) and Marchand et al. (2007), where radar reflectivity, Z, and mean Doppler velocity, V, are known to (3) a radar-lidar retrieval following O'Connor et al. (2005) based on three observables: radar reflectivity Z, radar Doppler spectral width σ_d, and lidar backscatter β. We briefly describe the radar-lidar and then the ZV and in this section, and present retrieval results and evaluate the retrievals using in situ observations in Section 4.

The radar-lidar retrieval technique uses three input variables radar reflectivity, Z (Figure 1b), doppler spectral width, σ_d (Figure 1e), and lidar backscatter, β (Figure 1c), to solve for three parameters in an assumed modified gamma distribution (equation 9) for the precipitation drop size distribution. The three parameter are the shape factor μ, the median equivolumetric diameter D_0, and the normalized droplet concentration N_w:

$$n(D) = N_w f(\mu)\left(\frac{D}{D_0}\right)^{\mu} e^{\left[\frac{-(3.67+\mu)D}{D_0}\right]} \tag{9}$$

where D is diameter, and $f(\mu)$ is a function of μ

$$f(\mu) = \frac{6}{3.67^4}\frac{(3.67+\mu)^4}{\Gamma(\mu+4)} \tag{10}$$

where Γ is the gamma function. Integration of the droplet size distribution in (9) will yield the precipitation droplet number concentration, N_{precip}, as in equation 2.

Following O'Connor et al. (2005), one can show that for a fixed value of the shape factor, μ, the ratio of the radar reflectivity to lidar backscatter is proportional to the fourth power of the mean drop size, and the combination of radar reflectivity and lidar backscatter can therefore be used to calculate D_0 and N_w. In the retrieval algorithm, this is done assuming an initial value of $\mu = 0$.

The Doppler spectral width is then forward calculated and μ is increased or decreased in order to match the observed Doppler spectral width (after applying corrections for beam width and turbulent motions). The forward calculations require a model for the hydrometeor terminal fall velocity, for which we use the model of Beard (1976). Once the three distribution parameters are known, it is straightforward to calculate the rain rate, rain liquid water content, and mean rain drop size, etc. using the fall velocity and equation (9). This retrieval technique has been widely used in retrieving drizzle properties (e.g. Ghate & Cadeddu, 2019; Yang et al., 2018), including the CSET campaign with airborne radar and lidar (Schwartz et al., 2019; Sarkar et al., 2021). Our implementation largely follows O'Connor et al. (2005), except for estimation of the contribution from air turbulence to the observed spectral width. Instead of using the horizontal wind speed to estimate the length scale (we note O'Connor et al. (2005) originally developed the retrieval for vertically pointing ground-based radar and lidar), we use the aircraft speed.

In addition to the radar-lidar retrieval technique, we also use a reflectivity-velocity (ZV) retrieval technique (Frisch et al.,1995; Mace et al., 2002; Marchand et al.,2007). The first step in this retrieval is to estimate the precipitation fall velocity from radar measured Doppler velocity, which includes the effect of vertical air motions (i.e., updrafts/drowndraft). We do this follow Orr and Kropfli (1998) and partition the measured Doppler velocities into a set of height and reflectivity bins (for each below-cloud zenith-pointing segment) and average the partitioned Doppler velocity as an estimate for the fall velocity (as a function of height and radar reflectivity). The underlying idea is that at a given altitude and reflectivity, there is a characteristic size distribution (with a characteristic fall velocity) and by averaging the Doppler velocities over a narrow range of reflectivity values, one averages out the effect of the updrafts and downdrafts leaving only the mean fall velocity. In this study we use reflectivity bins are that 2 dBZ wide, and use 200 m vertical bins with 100 m overlap. The results are not particularly sensitive to these choices, as long as there is a healthy number of samples are available in each bin. Following Frisch et al. (1995), it is straight-forward to obtain analytical expressions for distribution parameters D_0 and N_w given the derived fall velocity, measured reflectivity, and an assumed shape factor μ. Except were stated otherwise, we assume shape factor to be 0. One can show that the modified gamma distribution (equation 9) reduces to the exponential distribution when the shape factor is zero. In the radar-lidar retrieval we find retrieved shape factor is often quite small and we will examine and discuss the sensitivity of the ZV retrieval to assumed shape factor values in Section 4.2.

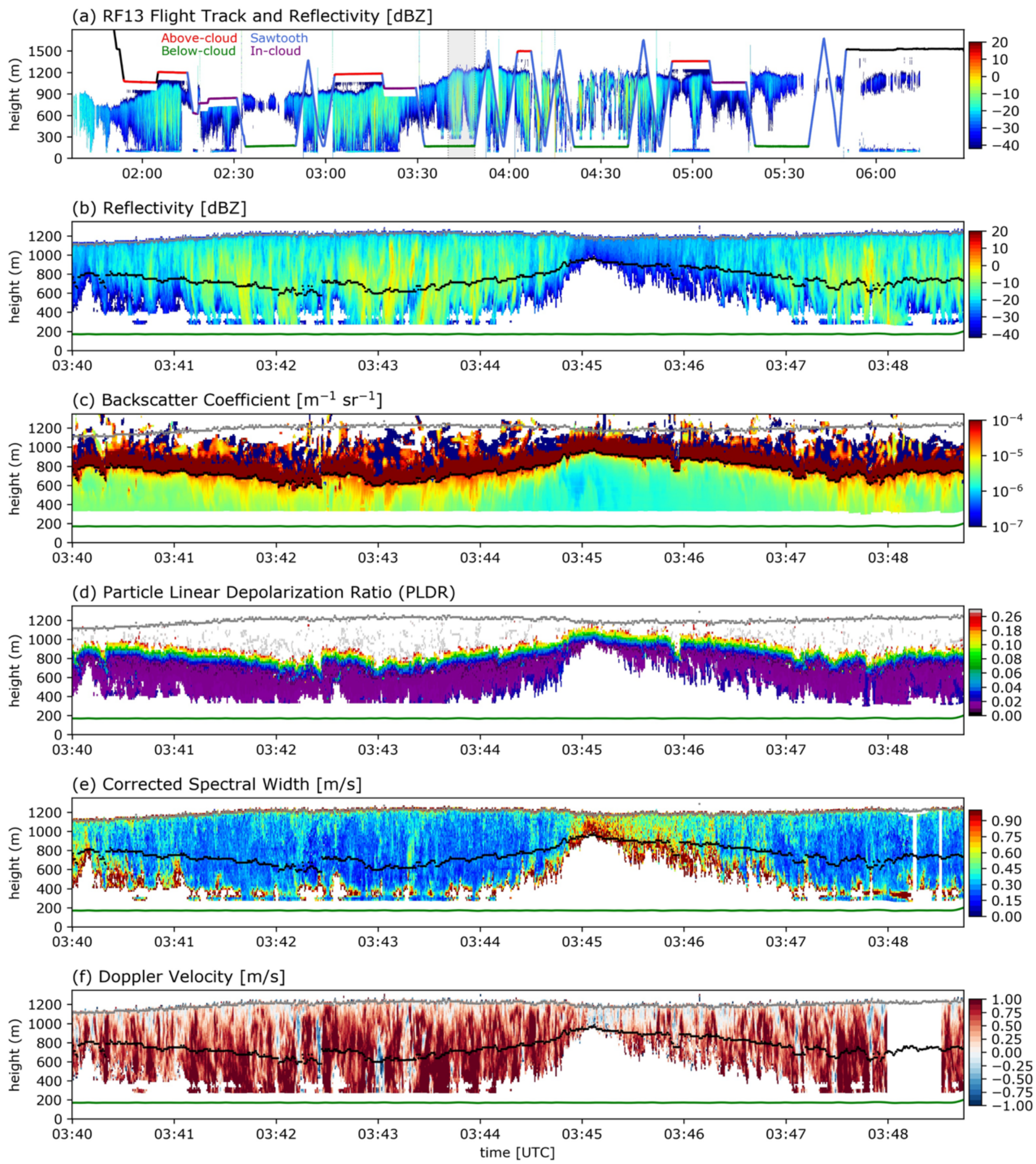

Figure 1. Example radar and lidar data collected during the SOCRATES. Panel a shows the flight tracks and reflectivity fields from research flight 13 (RF13), with different segments color-coded as in Figure S1. The grey shading marks a portion of one below-cloud level leg, and a zoom-in view of the radar and lidar fields for this segment are shown in panels b-f: (b) radar reflectivity; (c) lidar backscatter coefficient; (d) lidar particle linear depolarization ratio; (e) radar spectral width; (f) radar doppler velocity. The grey lines show the estimated cloud top, the black lines show the estimated cloud base, and the green line shows the location of the aircraft.

3 Campaign overview

To get a general sense of the hydrometers (clouds and precipitation) sampled by the airborne W-band radar during the SOCRATES, Figure 2a shows the joint histogram of radar reflectivity with height observed during below-cloud, zenith-pointing periods (i.e. as illustrated in Figure S1). Here the histogram is normalized by the number of radar columns, such that the value in each bin indicates how often hydrometers (cloud and precipitation) have a reflectivity (with +/- 1 dBZ of the given value) in the given altitude/height range; and the sum at each height (row) will gives the hydrometer fraction (Figure 2b).

Note that there is no data to the left of the red line in panel a. This is because of limited radar sensitivity, and as distance increases, the minimum detectable reflectivity value increases. Likewse, there are no data from 0 to 200 meters altitude because the aircraft lowest legs were typically flown at around 100-150 m altitude, and the radar blanking interrupt (the region corresponding to the time when the radar outgoing pulse is being, or has just been, transmitted and the radar system has not yet begun measuring the return power) typically extends about 203 m above this (Schwartz et al., 2019).

The maximum frequency of hydrometers observed by the radar occurred between 700 and 1200 meters, with a hydrometer fraction over 50%. (Note this is not projected area or the fraction of radar columns with a significant echo at any altitude, that value is near 90%). Reflectivity factors larger than -10 dBZ are relatively rare and there is no distinct mode associated with precipitation (that is, no peak with a reflectivity larger than about -20 dBZ). Reflectivity factors larger than -10 dBZ are common of the Southern Ocean (see for example Mace and Protat 2018), but such factors are associated with fronts or convection (including the shallow convection sometimes associated with vigorous open cells) and not typical of the shallow (cloud tops < 2 km) and largely overcast stratocumulus sampled during SOCRATES. Rather there is a single mode or continuum of reflectivity that span reflectivity factors from about -40 dBZ (where there are few if any precipitation sized particles) to values around -10 dBZ (where precipitation is still light with rain rate <1 mm hr^{-1} but can have a substantial impact on cloud condensation nuclei and cloud lifetime, Kang et al.,2022) and a peak below -20 dBZ. Most of this cloud is supercooled. Overall, we find that about 80% of the stratocumulus sampled during SOCRATES had a cloud top temperature < 0°C and cloud depth < 600m (figure not shown), and about 62% of the stratocumulus were precipitating, defined as 3 consecutive radar bins (about 60 meters) below cloud base with a reflectivity greater than -40dBZ. The occurrence of precipitation drops to 34% if a reflectivity threshold of -20 dBZ is applied (in spite of the detections being below cloud base), indicative of very light nature of the precipitation.

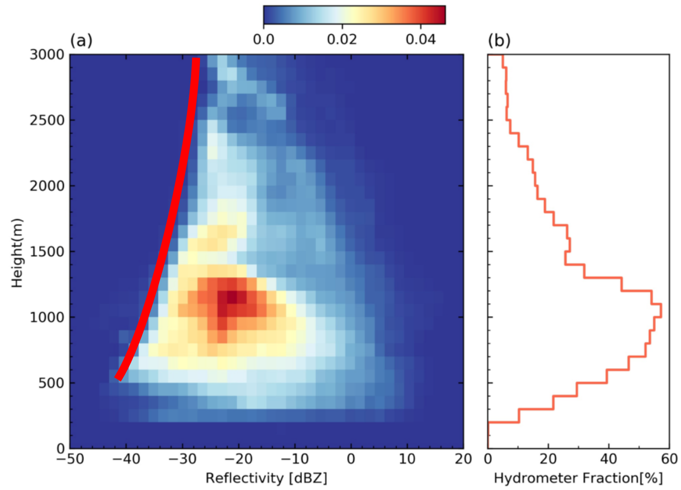

Figure 2. (a) Joint histogram of hydrometer (cloud & precipitation) radar reflectivity with height observed by the airborne W-band radar during below-cloud, zenith-pointing periods (i.e., when aircraft is flying below the cloud, as illustrated in Figure S1). Histogram is normalized by total number of radar "columns" such that the histogram values is the fractional occurrence (see text). (b) hydrometer fraction [%] at each height of all radar "columns". The red line on panel a shows the minimum detectable reflectivity values by HCR as a function of height.

What is the phase of the precipitation sampled during the SOCRATES? As described in Section 2.3.2, we determine the precipitation phase using the lidar particle linear depolarization ratio PLDR (Figure 1d), and interpret the precipitation as liquid phase when PLDR < 0.03; ice phase when PLDR > 0.05; and ambiguous for PLDR values in between. Figure 3a shows that around 60% of the precipitation from the zenith-pointing segments are liquid phase and about 20% of the precipitation are ice phase, with the remaining 20% being ambiguous phase. How does precipitation phase relate to the cloud top temperature? Figure 3b shows the relative occurrence of precipitation in difference phases as a function of cloud top temperature (CTT). For the warm-topped clouds (CTT > 0°C), we expect that all the precipitation should be liquid phase. Temperature is not used in the phase retrieval, and consistent with the discussion in Section 2, the low occurrence of ambiguous or ice phase precipitation with CTT > 0°C is indicative of the low retrieval error. For the cold-topped clouds (CTT <0°C), liquid precipitations still dominate for clouds with CTT between 0 and -10°C, with the ice fraction increasing as temperature decreases. But it is not until about a CTT of -15°C that ice phase appears to dominate. It could be that the apparent peak in ice phase occurrence near -15°C is a result of dendric growth (or secondary ice product associated with dendrites), as dendric growth is known to occur near this temperature (e.g., von Terzi et al., 2022) but there is too little data here to be confident this uptick in ice phase is statistically significant.

An interesting question related to phase is whether or not precipitation phase is related to radar reflectivity. Zhang et al. (2017) have shown that lidar depolarization ratios is correlated with radar reflectivity, and for the SO in particular, Mace and Protat (2018) show that W-band radar reflectivity greater than -10 dBZ is associated with ice-phase hydrometeors (based on CAPRICORN observations). Figure 3c shows the occurrence of the different precipitation phase for cold-topped clouds as a function of reflectivity. Overall, it shows that reflectivity factors less than about -10 dBZ are predominately liquid, while reflectivity factors greater than 0 dBZ is predominately ice. We will discuss this result in more detail in the conclusions.

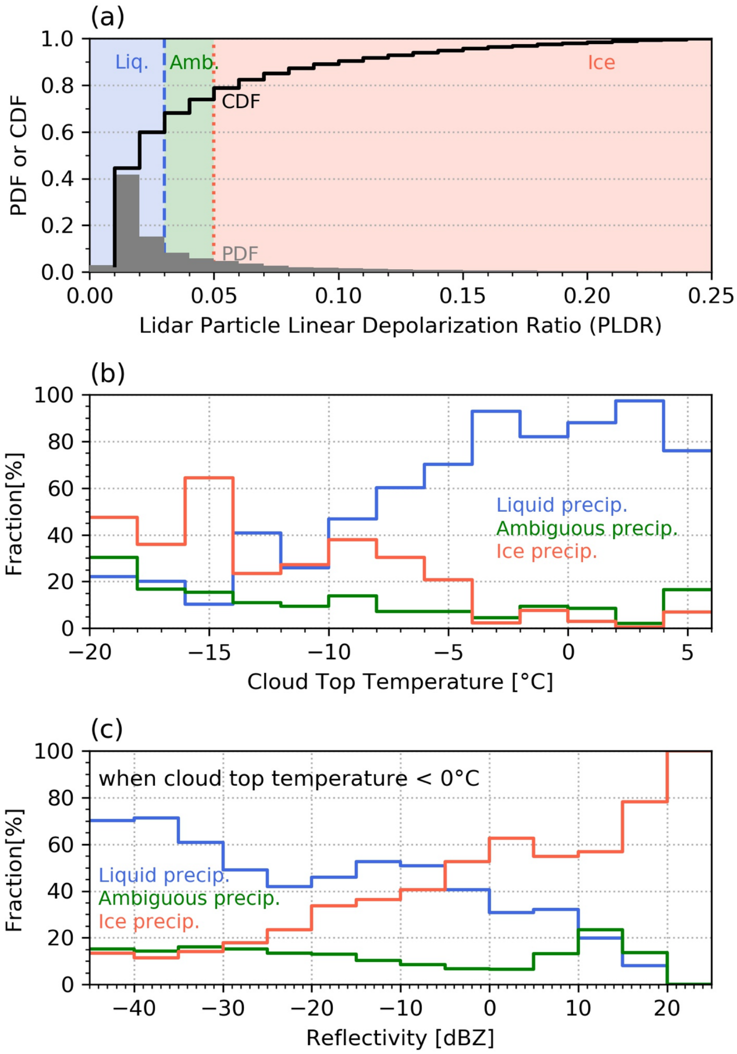

Figure 3. (a) Probability and cumulative density functions for lidar particle linear depolarization ratio (PLDR) for below-cloud precipitation (b) The fraction of liquid, ice, and ambiguous precipitation as a function of cloud top temperature. (c) The fraction of liquid, ice, and ambiguous precipitation as a function of radar reflectivity. To distinguish different precipitation type, liquid precipitation is marked as blue, ice precipitation is marked as red, and ambiguous precipitation is marked as green.

4 Precipitation Retrievals

In this section, we will explore a hierarchy of retrieval methods based on complexity, from (1) the simplest Z-R relationship approach where only one variable reflectivity Z is known, to (2) a ZV retrieval using two variables (reflectivity Z and Doppler velocity V), to (3) a radar-lidar retrievals based on three variables (reflectivity radar reflectivity Z, doppler spectral width σ_d, and lidar backscatter β). In section 4.1, we will develop Z-R relationships based on in situ data. In section 4.2, we will demonstrate the results from ZV and radar-lidar liquid precipitation retrievals using a case example, and in section 4.3, we evaluate these retrievals using in-situ aircraft observations from all the segments where retrievals were performed.

4.1 Reflectivity to rain rate (Z-R) relationships

One objective of this study is to estimate Z-R relationships of the form $\mathrm{Z} = \mathrm{a}R^b$. Z-R relationships are useful and convenient, requiring only one independent variable (reflectivity *Z*) to estimate rain rate *R*. Such relationships have a long history in atmospheric science, and as concerns stratocumulus in particular, relationships have been derived in past studies for stratocumulus over the Eastern Pacific (Comstock et al., 2004), over the north-east Atlantic and in U.K. coastal waters (Wood, 2005), and for nocturnal stratocumulus clouds off the California Coast (VanZanten et al., 2005). More recently, Protat et al. (2019b) estimated Z-R relationships at the surface over the global ocean, including the Southern Ocean, based on surface disdrometer measurements. In this section, we will derive Z-R relationships using SOCRATES aircraft observations following the method presented in Section 2.2.3 and compare our results with previous studies.

Figure 4 shows the Z-R relationships derived using in situ data taken at different locations relative to the cloud layer and surface (see Figure S1 for a schematic). Table 2 lists the corresponding a and b coefficients. In Figure 4a, we only consider droplets with a diameter larger than 40 μm following Comstock et al. (2004), while in Figure 4b, we include all droplets including those droplets with a diameter smaller than 40 μm. We will focus on Figure 4a first. Figure 4a shows that estimated Z-R relationships do have a vertical dependence. The intercept controlled by coefficient *a* increases as one moves from the cloud layer to the surface, while the slope controlled by exponent *b* remains largely unchanged. The vertical dependence of Z-R was also noticed in previous studies (e.g. Comstock et al., 2004; vanZanten et al., 2005). The exponent *b* estimated in Figure 4a ranges from 1.3 to 1.45, with a (one sigma) uncertainty that ranges from 0.5 to about 0.1, based on a bootstrap resampling technique (uncertainties are listed in Table 2). Note the uncertainties in the *a* and *b* coefficients are not independent, but rather are positively correlated such that a larger estimate for the a-value is associated with a larger estimate for the b-values. Table 2 also lists some Z-R relationships estimated from other studies mentioned above. Overall, we find the exponent *b* to be similar to that from Comstock et al. (2004), vanZanten et al. (2005), and many other earlier studies summarized in Rosenfeld and Ulbrich (2003) over other regions and other cloud types. Later in this section we will compare the rain rate derived from Z-R relationships with rain rate derived from two other retrieval methods.

The above analysis is based on the idea that only droplets larger than 40 μm are considered precipitation. But droplets smaller than 40 μm can and do contribute to the flux of liquid water (Nicholls, 1984). What happens if small droplets with a diameter smaller than 40 μm are included when calculating Z and R from in situ DSDs? The results are shown in Figure 4b. Comparing Figure 4a and 4b, one can see that the estimated Z-R relationships is very sensitive to whether one excludes smaller drops, especially for the data collected in the cloud. Differences in the estimated Z-R are less dramatic when using in situ data outside of the cloud (i.e. below-cloud portion of the sawtooth leg and below-cloud level legs).

To explore the importance of the smaller droplets, Figure 5a shows an example of DSDs measured near the top of a cloud, near the bottom cloud and below cloud during one sawtooth leg, as well as a nearby below-cloud level leg (depicted in the bottom panel). The associated liquid water flux distribution $D^3N(D)V(D)$ is shown Figure 5b, and the reflectivity distribution $D^6N(D)$ in Figure 5c. Note as in the microphysical retrievals, here we use the terminal fall velocity model of Beard (1976) for V(D). Below-cloud, small droplets evaporate much more quickly than larger droplets, and most of the contributions to the liquid water flux comes from larger droplets, such that the effect of small droplets on liquid water flux and reflectivity can be largely neglected. We hasten to add, however, this is true not true for the total number concentration (Figure 5a); where small droplets remain more numerous (than droplets above 40 μm), and includes many particles with sizes smaller than 5 μm, which one might consider haze-particles or hydrated-aerosols rather than cloud droplets. Within the cloud layer, small droplets make a large contribution to the liquid water flux and contribute slightly to the reflectivity. Droplets in the diameter range of 10-40 μm contribute 78% of the liquid water flux in the top half of the cloud, and still comprise about half of the water flux in the bottom half of the cloud. Contributions to the reflectivity from droplets in the range of 10-40 μm are smaller than those of larger droplets, but both make a non-trivial contribution.

In short, as Figure 5 and the differences in estimated Z-R in Figure 4a and Figure 4b highlight, the sedimentation of small droplets is (or can be) a significant component of the total liquid water flux in cloud and applying the Z-R relationship derived from only larger particles or from below-cloud measurements effectively ignores the contribution from small particles (and below-cloud Z-R equations should be applied with caution to in-cloud reflectivity measurements and should be expected to underestimate the total liquid water flux).

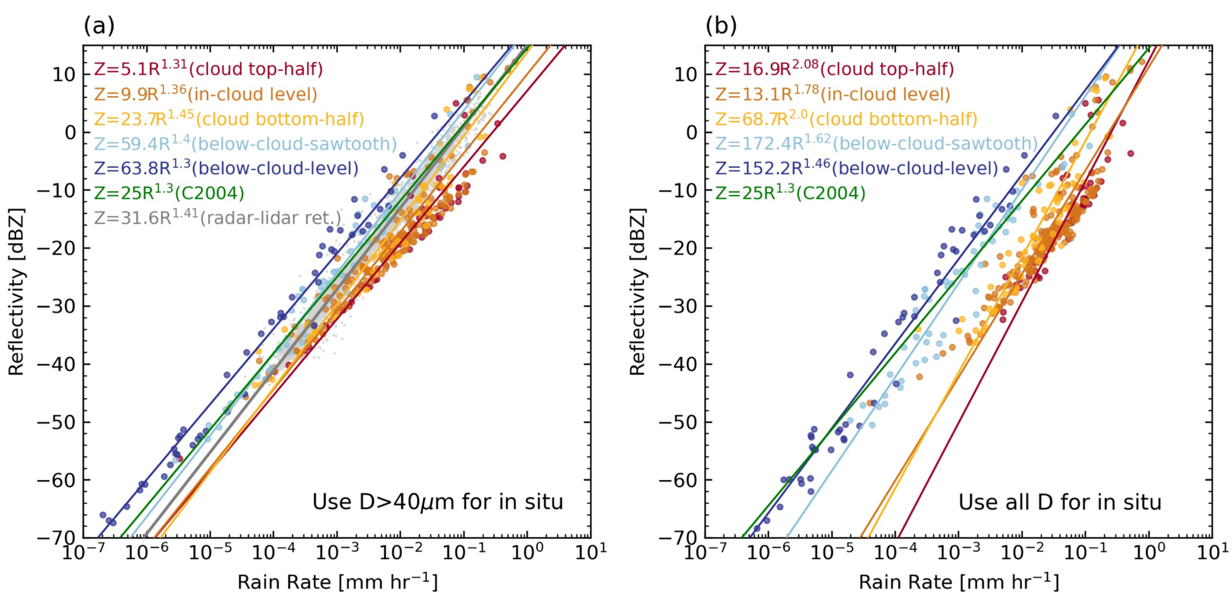

Figure 4. Z-R relationship derived using in situ data and retrievals. Diameter >40um cutoff for the in situ measurements is imposed in panel a, while panel b does not apply any cutoff, and considers all droplet sizes for in situ data.

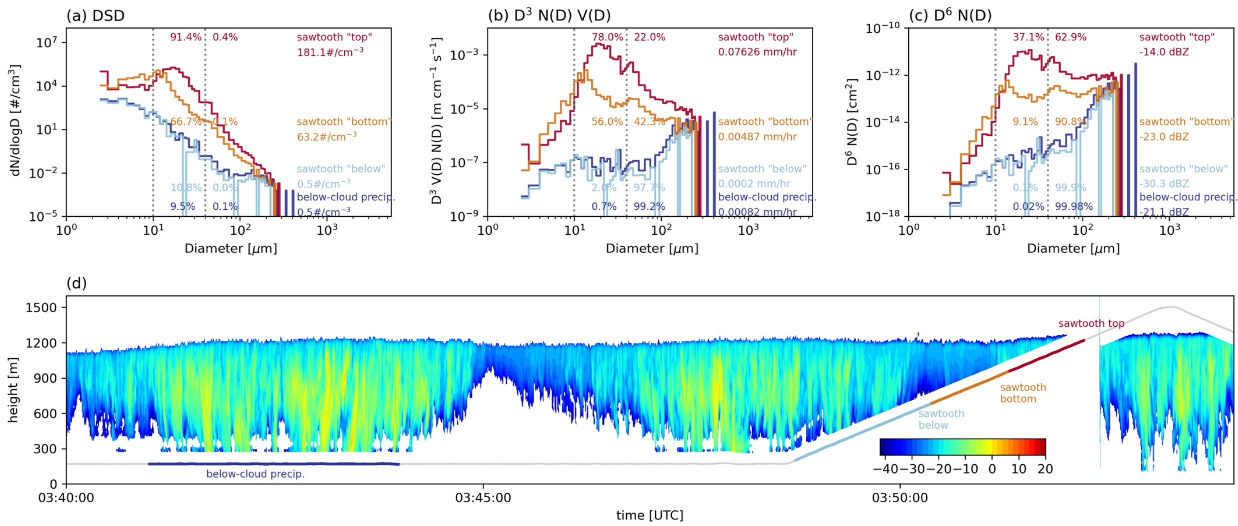

Figure 5. Example case to show the contributions of droplets in different size ranges with in situ measurements taken from different segments: (a) average droplet size distribution; (b) product of diameter cubed, droplet size distribution and terminal fall velocity;(c) product of diameter to the power of six and droplet size distribution; (d) reflectivity field and flight track for this example, the color-coded lines marked the locations of different segments showing in panel a-c. The vertical dashed line in panels a-c is the reference line for 10 μm and 40 μm. The percentage on panel a, b, and c show the contributions from different size range to droplet number concentration, to rain rate, and to reflectivity, respectively.

Table 2. Z-R relationship of the form $Z = aR^b$

Equation	Location	Remarks	Reference
$Z = (5.1 \pm 3.5)\, R^{(1.31 \pm 0.1)}$ $[Z = (16.9 \pm 26.1)\, R^{(2.08 \pm 0.25)}]$	the top half of the cloud layer from the sawtooth leg	Estimated using SOCRATES aircraft in situ measurements with and without the 40µm cutoff, [without given in brackets]	This study
$Z = (9.9 \pm 2.8)\, R^{(1.36 \pm 0.05)}$ $[Z = (13.1 \pm 6.8)\, R^{(1.78 \pm 0.11)}]$	in-cloud level legs		
$Z = (23.7 \pm 11.6)\, R^{(1.45 \pm 0.08)}$ $[Z = (68.7 \pm 68.5)\, R^{(2.0 \pm 0.16)}]$	bottom half of the cloud layer from the sawtooth leg		
$Z = (59.4 \pm 21.4)\, R^{(1.4 \pm 0.04)}$ $[Z = (172.4 \pm 106.7)\, R^{(1.62 \pm 0.06)}]$	the below-cloud portion of the sawtooth leg		
$Z = (63.8 \pm 47.1)\, R^{(1.3 \pm 0.05)}$ $[Z = (152.2 \pm 277.9)\, R^{(1.46 \pm 0.09)}]$	below-cloud level legs.		
$Z = (31.6 \pm 1.4)\, R^{(1.41 \pm 0.007)}$	Cloud base	Estimated using SOCRATES W-band radar measured reflectivity and radar-lidar retrieved rain rate just-below cloud base	
$Z = 25R^{1.3}$	Cloud base	Estimated for stratocumulus over Eastern Pacific	Comstock et al. (2004)
$Z = 12.92\, R^{1.47}$	Cloud base	Estimated using aircraft in situ DSD measurements for nocturnal stratocumulus clouds over California Coast	vanZanten et al. (2005)
$Z = 12.5\, R^{1.18}$	All in-cloud levels	Estimated using aircraft in situ DSD measurements for stratocumulus over the north-east Atlantic and in U.K. coastal waters	Wood (2005)

Note: here uncertainty is estimated using either by bootstrapping (rows 1-5) or moving block bootstrapping (row 6) with the one-sigma uncertainty given after the plus-minus sign. For the Z-R relationship that is estimated using in situ measurements, the Z-R relationship estimated using only larger *droplets, with a diameter greater than 40μm, is listed first, followed by the Z-R relationship estimated using all droplets included those droplets with a diameter smaller than 40 μm. For the equations above, the reflectivity Z is in the unit of mm^6mm^{-3}, and the rain rate is in the unit of mm hr^{-1}. For the equations in the past studies with the form of $R = cZ^d$ or have different units, we rearranged the equation and converted the units to keep the consistency and make it easier to compare. Unless noted, the default band for reflectivity is W-band.*

4.2 ZV retrieval and radar-lidar retrieval

In this subsection, we examine both the ZV retrieval and radar-lidar retrievals using the zenith-pointing remote sensing data collected when the aircraft was flying level-legs below the cloud. We will begin with one case study, compare results from different retrieval methods, and then examine the sensitivity of ZV retrieval results to the assumed shape factor μ. The overall retrieval performance will be evaluated in Section 4.3.

Applying the ZV retrieval (described in Section 2.3.3) to the example presented in Figure 1, the parameters D_0 and N_{precip} can be derived from measured reflectivity Z, assumed shape factor μ, and derived terminal fall velocity. Figure 6a shows the reflectivity-weighted terminal fall velocity, v_t , derived following Orr and Kropfli (1998). Here we see generally larger v_t toward the bottom of the cloud, and in precipitation shafts (regions of relatively high reflectivity extending below cloud base). Figure 6b and 6c shows derived median equivolumetric diameter D_0, and precipitation concentration N_{precip}, assuming μ =0. Not surprisingly, Figure 6b shows that D_0 is larger where v_t is larger, and is about 100-200 μm below cloud base. Figure 6c shows N_{precip} below cloud base is in the order of 10^3~10^5 m^{-3}.

Applying the radar-lidar retrieval technique to the example presented in Figure 1, with three input variables (radar reflectivity Z, doppler spectral with σ_d, and backscatter coefficient β), we can also solve for shape factor μ , median equivolumetric diameter D_0, and precipitation number concentration N_{precip}, as shown in Figure 7. The shape factor μ describes the shape of the DSD (equation 9) and larger μ implies narrower distributions. As in O'Connor et al. (2005), we find large areas with broad DSDs (small μ). Narrow DSDs implied by large μ are typically found underneath the thicker portion of the clouds (and as we will see later have larger rain rates). The median equivolumetric diameter D_0 is mostly between 50-250 μm, with larger sizes occurring where μ is larger. Again, this is similar to what O'Connor et al. (2005) observed and appears to be quite typical for drizzling stratocumulus. Comparing the two retrieval methods, both D_0 and N_{precip} from ZV retrieval (Figure 6) tend to be more spatially homogeneous below cloud base than that from radar-lidar retrieval (Figure 7), and the D_0 from ZV retrieval tends to be smaller than that from radar-lidar retrieval in the precipitation shafts (where the assumption of a small value for the shape factor appears problematic, more on this below).

Once the parameters that determine the DSDs are derived, it is straightforward to calculate other precipitatition properties such as rain rate. Figure 8b and c show the ZV retrieved the rain rate (assuming μ =0) and radar-lidar retrieval retrieved the rain rate. Overall, the two retrieval methods give similar results (mean of rain rate from ZV retrieval is 0.0096 mm hr^{-1}, and mean of rain rate from radar-lidar retrieval is 0.0093 mm hr^{-1}). With derived Z-R relationships from section 4.1, one can also derive rain rate by apply them to the radar reflectivity fields, as shown in Figure 8a, with derived rain rate by applying Z-R relationships shown in Figure 4a from sawtooth-top to the top half of the cloud, from sawtooth-bottom to the bottom half of the cloud; as well as sawtooth-below to area below the cloud base. Overall, the retrieved rain rate has a magnitude that is around 0.001-0.1 mm hr^{-1}. The discontinuity in the rain rate fields in Figure 8a is because three different Z-R relationships are applied to different regions. The difference in Z-R relationships (i.e. with or without D>40 μm cutoff) also results in differences in derived rain rate (Figure S7), especially for the in-cloud portion. Overall, regardless of the retrieval approaches, it can also be seen that higher rain rates tend to occur below the geometrically thicker portion of the clouds, and we will explore the scaling between rain rate and cloud depth further in Section 6.

In Figures 6 and Figure 8b, we assume μ =0 in the ZV retrieval, while retrieved μ from radar-lidar retrieval clearly shows spatial variations (Figure 7a). How will ZV retrieved D_0, N_{precip}, and rain rate vary with assumed μ? Figure S8 shows that the derived D_0 increases with increasing μ values such that mean D_0 just below cloud base is 102 μm when $\mu = 0$, and is 156 μm when $\mu = 10$. In contrast, as shown in Figure S9, the derived N_{precip} decreases significantly with increasing μ values, with mean N_{precip} at cloud base is about 1.2×10^5 m^{-3} when $\mu = 0$, and is 1.2×10^3 m^{-3} when $\mu = 10$. However the derived rain rate (Figure S10) shows relatively little dependence on assumed μ, with rain rate at cloud base decrease slightly from about 0.009 mm hr^{-1} ($\mu = 0$) to about 0.007 mm hr^{-1} ($\mu = 10$). The small sensitivity in rain rate ultimately arises because the liquid water flux is to first order given by the velocity (which is input to the retrieval) times the liquid water content (which is strongly constrained by the reflectivity that is likewise input to the retrieval).

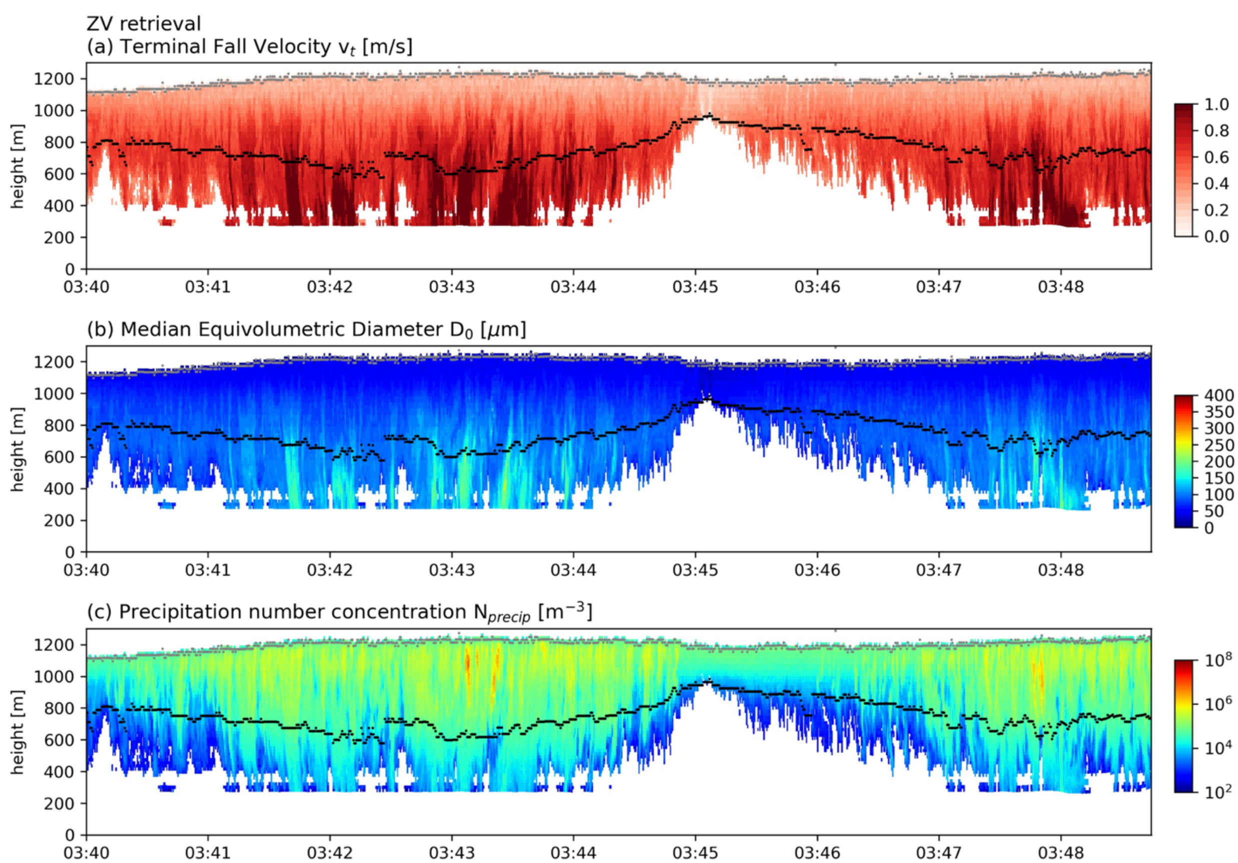

Figure 6. A time-height plot of ZV method retrieved drizzle properties assuming shape factor for the example segment is shown in Figure 1. (a) reflectivity-weighted the terminal fall velocity

v_t; (b) median equivolumetric diameter D_0, and (c) precipitation number concentration N_{precip}. The grey lines show the estimated cloud top, the black lines show the estimated cloud base.

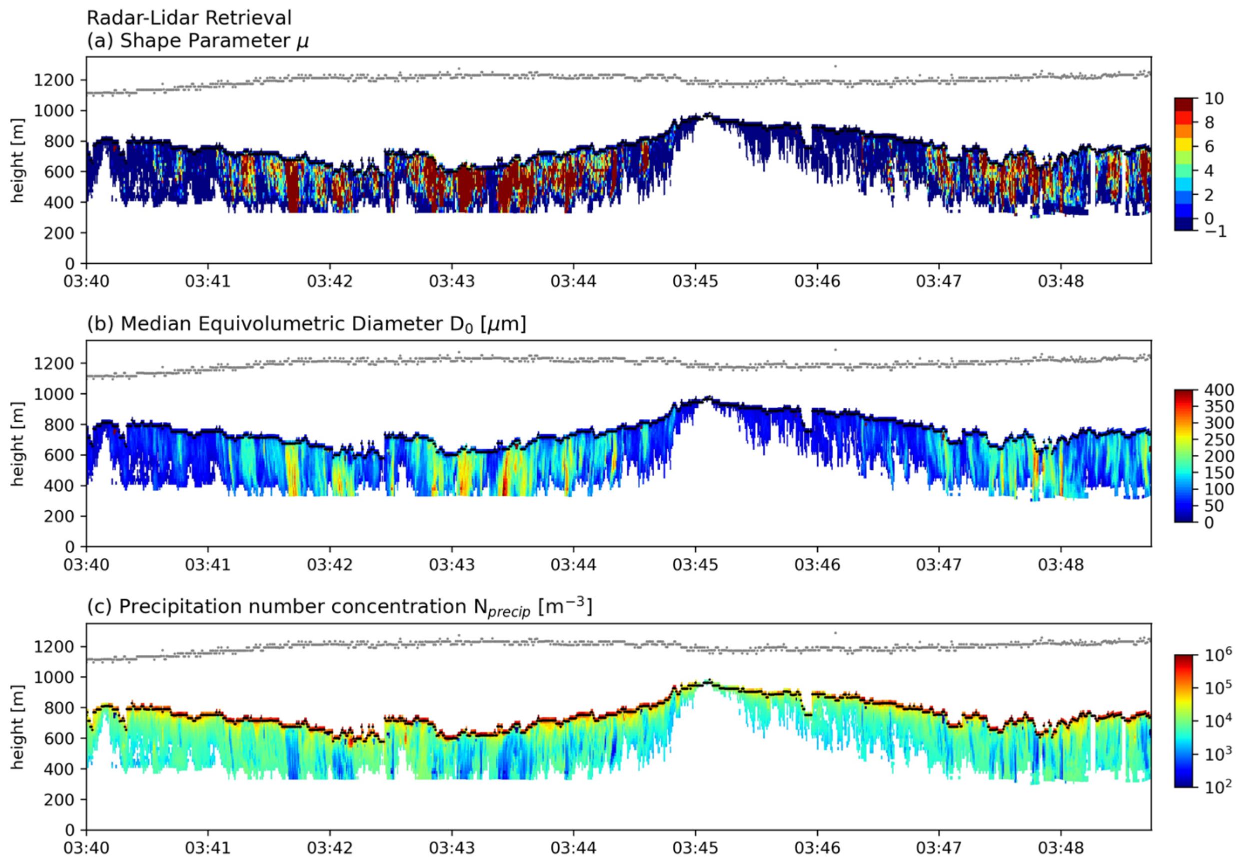

Figure 7. A time-height plot of radar-lidar retrieved drizzle properties for the example segment is shown in Figure 1. Radar-lidar retrieval method derived parameters for modified gamma distribution (a) shape factor μ; (b) median equivolumetric diameter D_0, and (c) precipitation number concentration N_{precip}. The grey lines show the estimated cloud top, the black lines show the estimated cloud base.

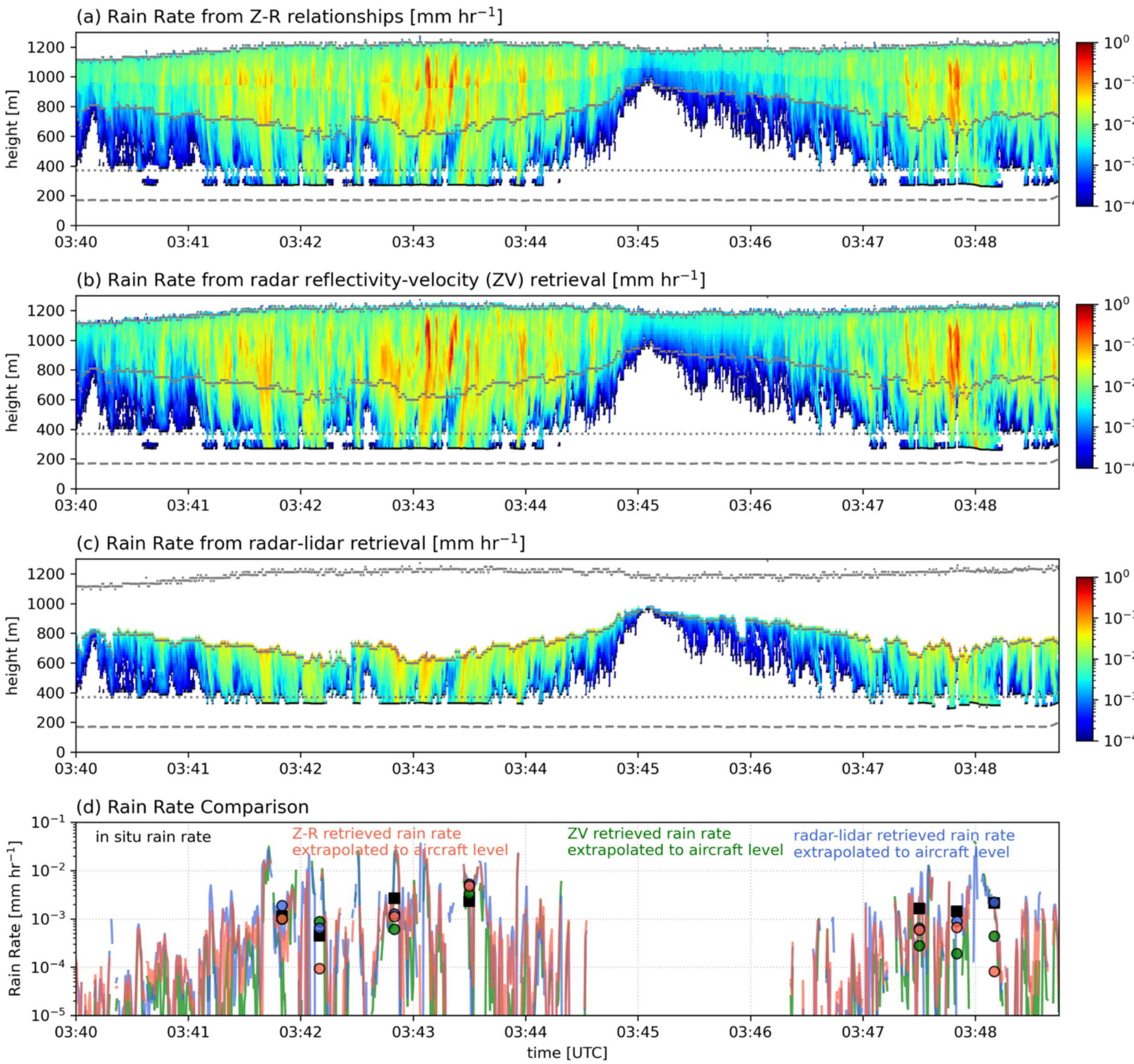

Figure 8. Retrieved rain rate for example case using (a) Z-R relationships (D > 40µm), (b) ZV retrieval technique, and (c) radar-lidar retrieval technique, and (d) their comparisons with in situ estimates. In panels a-c, the dashed grey line shows the location of the aircraft, while the dotted line is a reference line to show 200 meters above the aircraft's location. In panel d the retrieved rain rates were extrapolated to the aircraft level to compare with the in situ data. The pink line shows the rain rate retrieved with Z-R relationships, the green line shows the rain rate retrieved with the ZV retrieval technique, and blue line shows the rain rate retrieved with the radar-lidar retrieval technique. The black squares represent the rain rate estimated with in situ measurements, where rain rates are derived from averaged droplet size distribution (merged CDP and 2DS) over 20 seconds. Over that same time window, the median value of the retrieved rain rate time series was taken, denoted as pink dots (Z-R relationship), green dots (ZV retrieval) and blue dots (radar-lidar retrieval).

4.3 Retrieval validation

How good are the rain rate retrievals? One would think a simple comparison between the retrieved rain rate with in situ measurements from the aircraft could answer this question. But there are a few challenges that need to be overcome.

The first challenge is that retrieved rain rates that are closest to the aircraft level marked as a dashed line around 200 m in Figure 8) are still at least 150 meters away, making it difficult to make a direct comparison. This is because there is a blanking interrupt, a brief period where one needs to wait for the outgoing pulse to exit the radar (or lidar) system and for the effect of strong scattering from nearby objects (clutter) to dissipate. To overcome this difficulty, we extrapolate the retrieved rain rate downwards to the aircraft level by fitting an exponential function to each radar column. The assumption is that the rain rate varies with distance below the cloud base exponentially due to evaporation (Wood, 2005; Comstock et al., 2004). Figure S11 in the supporting information shows an example of rain rate derived from the exponential fit, and demonstrates that the exponentially fitted rain rate shows reasonable agreement with the retrieved rain rate where such is retrieved. Figure 8d compares the extrapolated rain rate from the Z-R relationship (red line), extrapolated rain rate from ZV retrieval (green line), extrapolated rain rate from radar-lidar retrieval (blue line). To further increase our confidence, we only compare the extrapolated rain rate from those periods where the original retrieved rain rate extends to within 200m of the aircraft (i.e. when the rain extends down to dotted reference line). Another challenge is the limited sampling volume of the in situ probes. To overcome this difficulty, we average the in situ DSD over a 20s period, marked as black squares in Figure 8d, and similarly, we also average the corresponding retrievals over the same 20s time window, marked by the red, green and blue dots. It can be seen that the retrieved rain rate shows reasonable agreement with in situ data for this case.

We repeated this analysis for the liquid-precipitation retrievals for all the SOCRATES flights and summarize the results in Figure 9. Overall, the Z-R, ZV, and radar-lidar retrievals compare well with the in situ, with Pearson correlation coefficient of 0.83. 0.88 and 0.68, respectively. Despite the simplicity of the approach, even the rain rate derived from Z-R relationship shows good performance compared to the in situ values, with a fractional difference (difference in 20s medians / average of 20s medians) of only -8.0%. If we estimate the uncertainty in the retrieved rain rate via error propagation, and we estimated the uncertainty in reflectivity as 1.5 dB for reflectivity (following O'Connor et al., 2005) and 10% for lidar backscatter (e.g., Schwartz et al., 2019), we estimate the uncertainty in the radar-lidar retrieved rain rate would be 18%. Similarly, with the uncertainty of 1.5 dB for reflectivity, and 10% uncertainty for terminal fall velocity (see Tansey et al., 2022), we estimate the uncertainty in the ZV retrieved rain rate to be 44%. As for the Z-R relationship (using the below-cloud sawtooth leg relationship), the estimated the uncertainty in rain rate is 38.4%. Relative to the expected uncertainties due simply from uncertainties in the inputs, all three retrievals compare well with the in situ data.

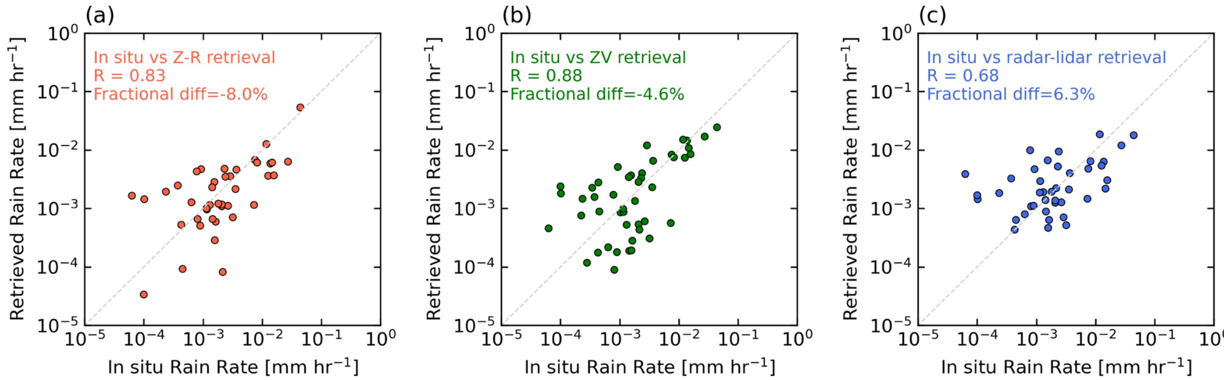

Figure 9. Comparison of in situ estimates with (a) Z-R retrieval, (b) ZV retrieval, and (c) radar-lidar retrieval for the entire campaign. The retrieved rain rates plotted here that were extrapolated to the aircraft level (see Figure 8, S11) to compare with the in situ data. Fractional difference is calculated as the difference between the retrieved and in situ median value divided by the average of the medians.

5 Vertical distribution of precipitation properties

In this section, we will apply the precipitation observations and retrievals to study the vertical distribution of precipitation properties.

Figure 10 shows a violin plot of in situ measured precipitation properties at different altitudes and retrieved precipitation properties below the lidar-inferred cloud base. For each dataset, the white dot represents the median value, while the black bar represents the interquartile range. Perhaps surprisingly rain rate decreases going downward from the top half of the cloud (i.e. the largest rain rates are in the upper portion of the cloud). Medians of rain rate at the cloud top half, cloud bottom half and below the cloud are of 0.021 mm hr^{-1}, 0.008 mm hr^{-1}, and 0.001 mm hr^{-1}. Similar to rain rate, there is also a decrease in precipitation number concentration (N_{precip}) and precipitation liquid water content (LWC_{precip}) moving downward from the top half of the cloud. In contrast, D_{precip} and σ_{precip} increase moving downward, that is bigger particles in the bottom half, and (just) below cloud. Overall, the retrieved precipitation properties (below the cloud base) compare well with the in situ estimates from the sawtooth below-cloud segments.

How do precipitation properties vary below cloud base? Figure 11 provides a more detailed view on the vertical distribution of precipitation properties below cloud base. Here, the column shows rain rate, N_{precip}, LWC_{precip}, D_{precip}, and σ_{precip}, respectively. The first two rows are histograms for radar-lidar and ZV retrievals, respectively. The last row is a box plot that summarizes both retrievals by binning the data vertically every 100 meters. Here, we only consider data in those radar columns where rain extend at least 400m below cloud base. Overall, both the mean rain rate and LWC_{precip} decrease exponentially with distance (as the change in the position of the distribution peak is roughly linear with distance on a log-scale). Both retrievals have similar values and rates of decrease (panel k and panel m). The e-folding distance over which the rain rate decrease to 1/e

(37%) of its initial value is about 260m for radar-lidar retrieval and 340 m for ZV retrieval. N_{precip} also decreases with distance, but we find the radar-lidar retrieval decreases more rapidly within the 200m below the cloud base, and the ZV retrieval shows higher N_{precip} than radar-lidar retrieval at different levels. This is consistent with (a result of) assuming a shape factor of zero in the ZV retrievals. The mean D_{precip} and σ_{precip} both increase with distance. Compared to radar-lidar retrieved D_{precip}, ZV retrieved D_{precip} is smaller overall (again consistent with the assumed shape factor), and has much less spread (variation) at any given altitude. Figure 10d shows that radar-lidar retrieved D_{precip} compare better with the in situ estimated D_{precip} from the below-cloud portion of the sawtooth legs than the ZV retrieved D_{precip}.

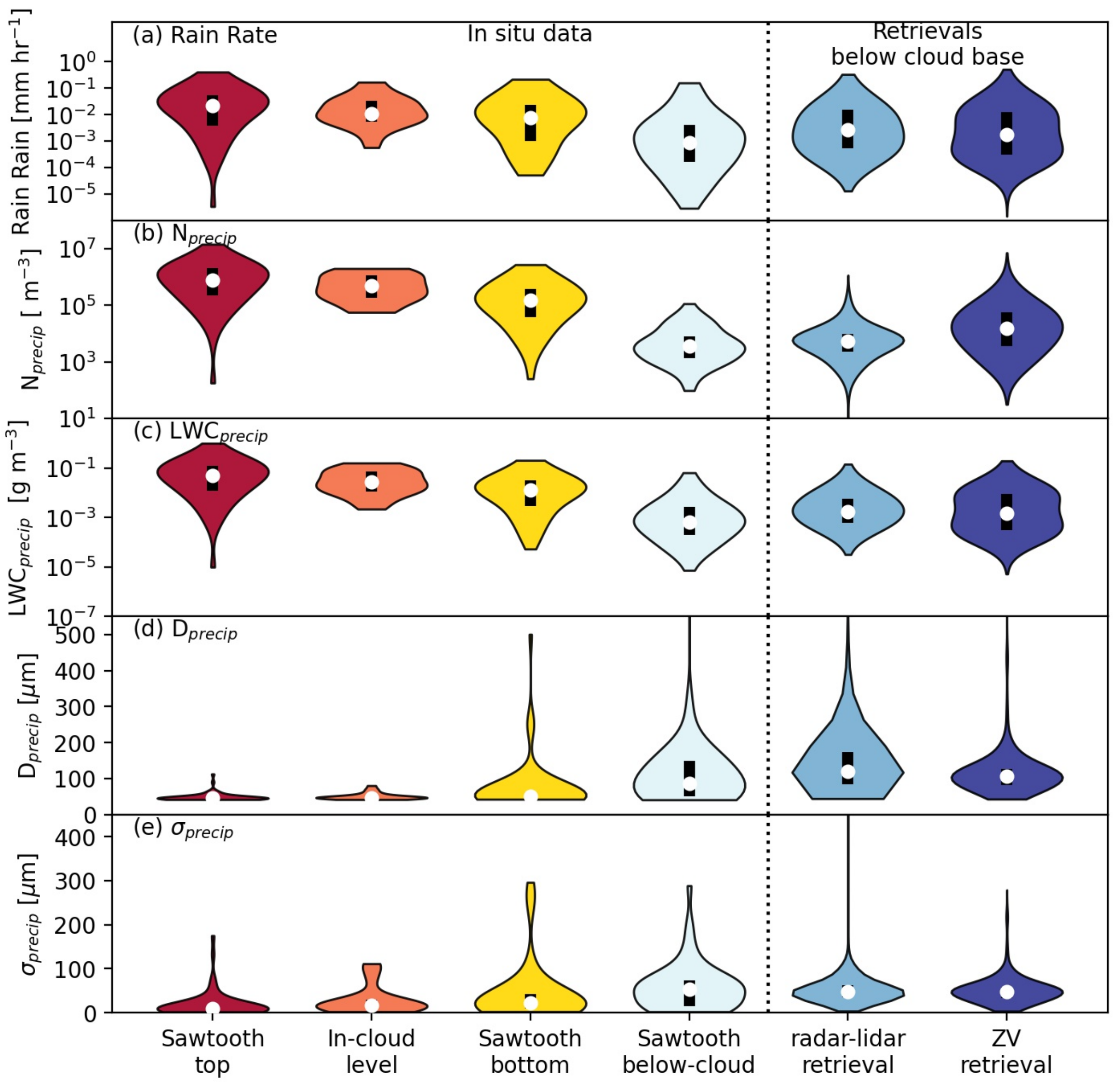

Figure 10. Violin plot for in situ measured precipitation properties at different altitudes and retrieved precipitation properties below cloud base: (a) rain rate (or precipitation liquid water flux), (b) precipitation number concentration N_{precip}, (c) precipitation liquid water content LWC_{precip}, (d) precipitation liquid water content weighted mean diameter D_{precip}, (e) precipitation liquid water content weighted width σ_{precip}. A violin plot can be regarded as a hybrid of a boxplot

and a kernel density plot. For each dataset, the white dot represents the median value, while the black bar represents the interquartile range, and the outer shape is the kernel density estimation to show the distribution of the data. In situ measured precipitation properties are from these legs (as marked in Figure S1): the top half of the cloud layer from sawtooth legs (sawtooth top); the bottom half of the cloud layer from sawtooth legs (sawtooth bottom); the below-cloud portion of the sawtooth legs (sawtooth below-cloud); and in-cloud level legs.

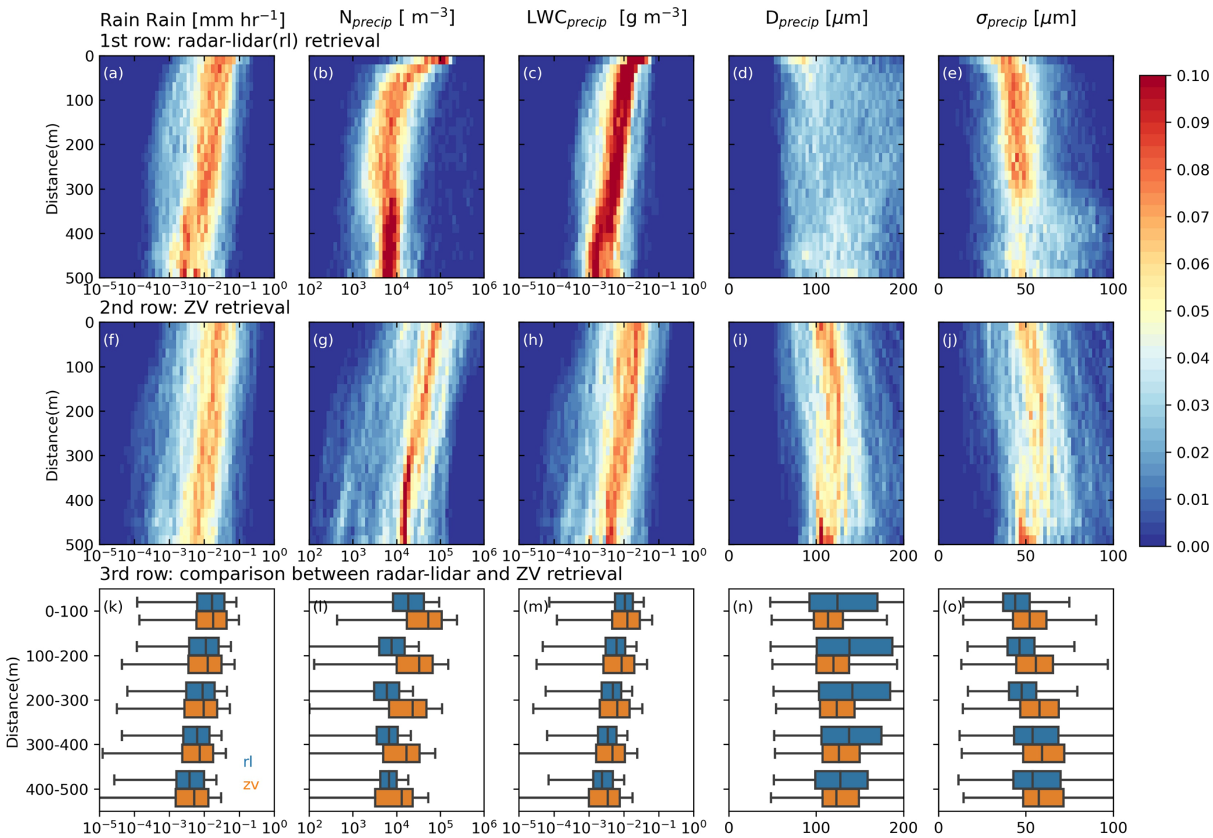

Figure 11. Vertical distributions of below-cloud-base precipitation properties from retrievals (each column is rain rate, N_{precip}, LWC_{precip}. D_{precip}, σ_{precip} respectively). The first and second row is the histogram of retrieved precipitation properties below-cloud-base (data are normalized at each level), and y axis is the distance away from the cloud-base. First row is the results from radar-lidar retrievals, the second row is the results from ZV retrievals. The last row is the box plot that summarized the data in the first two rows by binned the data vertically every 100 meters, where blue boxes are from radar-lidar retrievals, and orange boxes are from ZV retrievals.

6 Rain rate dependence on cloud depth and aerosol concentration

In this section, we examine the degree to which precipitation can be diagnosed from cloud depth and cloud droplet or aerosol number concentration in the form (e.g. Comstock et al., 2004; Terai et al.,2012; Mann et al., 2014)

$$R_{CB} = k\, H^{\alpha}\, N^{\beta} \tag{11}$$

where N is usually the cloud droplet (N_d) or aerosol number concentrations (N_a), and H is cloud depth or liquid water path, and R_{CB} is rain rate at cloud base. To our knowledge, such a relationship has not been examined over the SO, except by Mace and Avey (2007) who used satellite retrievals. To examine this relationship over the SO, we use radar-lidar retrieved rain rate for R_{CB} , use the difference between cloud top and cloud base for H, and use accumulation mode aerosol concentrations with diameters larger than 70 nm from UHSAS for N_a.

First, we broadly examine the rain rate dependence on either cloud depth or aerosol concentration, individually. Figure 12a shows a joint histogram of rain rate at cloud base and cloud depth. The histogram shows that rain rate (at cloud base) scales with cloud depth, such that thicker clouds are associated with higher rain rates. This is consistent with previous studies (e.g. vanZanten et al., 2005; Pawlowska and Brenguier, 2003; Geoffroy et al., 2008). And to demonstrate the rain rate dependence on aerosol concentration, Figure 12b shows the probability density function of rain rate partitioned for conditions with low aerosol concentrations (lower than the first quartile, marked as blue) and high aerosol concentrations (higher than the third quartile, marked as red). Figure 12b shows that overall higher aerosol concentrations are associated with lower rain rates, consistent with aerosol suppression of precipitation.

How does rain rate relate to both cloud depth and aerosol concentration? To derive the coefficients in equation (11), we divided cloud depth (H) up to 600m into 6 bins, and divided aerosol concentrations (N_a) into 4 bins, and calculated the median rain rate for each H and N_a pair. Then we performed linear least square regression on the natural logarithms of data from these 24 bins (Figure 12c). The derived relationship is $R_{CB} = 1.73 \times 10^{-10}\, H^{3.6}\, N_a^{-1}$, with H in m, N_a in cm^{-3}, and R_{CB} in mm hr^{-1}. Using bootstrap resampling technique, we estimate that the exponent α (one sigma uncertainty) for H range from 3.4 to 3.9, while the exponent β for N_a range from -1.3 to -0.8. The relationship we derive here is broadly similar to previous studies for stratocumulus in other regions. Exponent α for cloud depth typically is about 3 (vanZanten et al., 2005; Pawlowska and Brenguier, 2003; Lu et al., 2009), and the exponent β for number concentration (cloud droplet concentration or cloud condensation nuclei) typically ranges between -1.75 to -0.66 (vanZanten et al 2005; Mann et al., 2014; Lu et al., 2009; Comstock et al., 2004). The exponent β of -1 for aerosol concentration we derived here is smaller than exponent β of -0.32 in Mace and Avey (2017, hereafter M17), estimated using satellite-estimated cloud droplet number concentration, liquid water path, and rain rate for the SO. We will discuss this difference further at the of the next section.

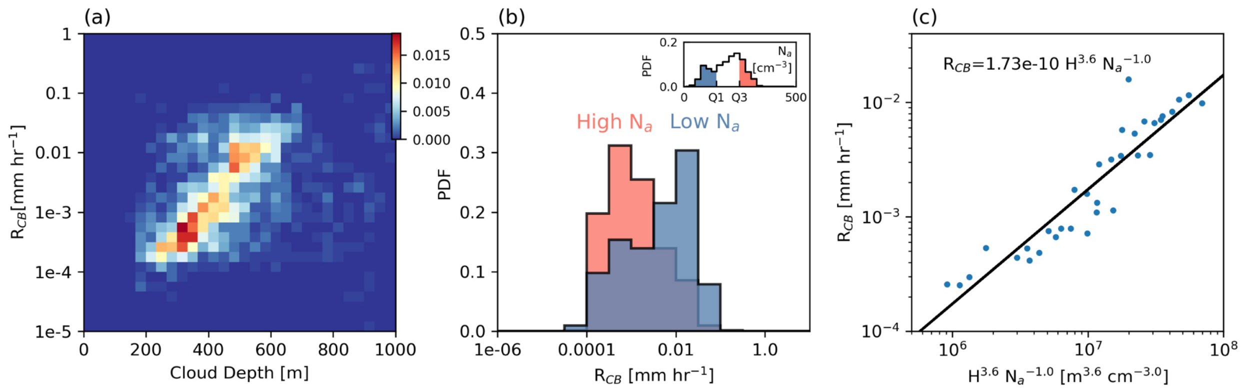

Figure 12. (a) Histogram of rain rate plotted as a function of cloud depth. (b) The probability density function of rain rate for conditions with low aerosol concentrations (lower than the first quartile, marked as blue) and high aerosol concentrations (higher than the third quartile, marked as red). (c) The rain rate at the cloud base is plotted as a function of the cloud depth, H, and aerosol concentration, N_a. Here H and N_a are the middle points for each cloud depth and aerosol concentration bin, while the rain rate at the cloud base is taken as the median value of rain rates in each cloud depth and aerosol concentration bin. The solid line shows the parametrization described in the main text.

7 Conclusions

In this study, we examine in-and-below-cloud precipitation properties for stratocumulus over the Southern Ocean (SO), leveraging data collected from airborne W-band Cloud Radar (HCR), High Spectral Resolution Lidar (HSRL), and various in situ probes during the Southern Ocean Clouds Radiation Aerosol Transport Experimental Study (SOCRATES) in January-February 2018.

Overall, we find that about 60% of the stratocumulus were precipitating, and about 80% of the stratocumulus to be cold-topped (with a cloud top temperature < 0°C) based on periods where the aircraft were flying below cloud and the radar and lidar pointing toward zenith. We determine the precipitation phase using the lidar particle linear depolarization ratio PLDR and find that about 60% of the precipitation is liquid phase, and about 20% of the precipitation is ice phase, with the remaining 20% being ambiguous. While we can not rule out the possibility that any individual ambiguous cases is pure liquid, most of such cases are likely to have ice or mixed phase precipitation present. Further, for cold-topped cloud, we find that when the reflectivity factor is less than about -10 dBZ, the precipitation is predominately liquid, while reflectivity factors greater than 0 dBZ, precipitation is predominately ice. This results is similar to what was found by Mace and Protat (2018) based on CAPRICORN data the during March-April 2016, as well as a recent study by Tansey et al. (2023) based on surface data collected at Macquarie Island (54.5 °S) between March and November 2016. The SOCRATES data, collected in the Southern Hemisphere Summer, in January and February 2018, suggest this relationship is likely characteristic of SO low clouds through the year, and suggests that the measured reflectivity factor might be used as a proxy to determine the precipitation phase for *cold-topped Southern Ocean stratocumulus* with CloudSat (or other "radar only") retrievals where no other information is available to constrain the precipitation phase.

For liquid-phase precipitation, we performed retrievals for precipitation rain rate and other microphysical parameters based on cloud radar and lidar, with the goal to testing a hierarchy of retrieval methods, from the simplest Z-R relationship approach where only radar reflectivity (Z) is used to estimate the rain rate, to a reflectivity-velocity (ZV) retrieval where there are two observables (inputs to the retrieval), to a radar-lidar retrieval with three observables. Our evaluation show that rain rate from the Z-R, ZV, and radar-lidar retrievals all compare well with the in situ, with Pearson correlation coefficient of 0.83. 0.88 and. 0.68, and fractional difference (difference between the retrieved and in situ median value divided by the average of the medians) of only -8.0%, -4.6%, and 6.3%, respectively. In addition to rain rate, ZV and radar-lidar retrievals can retrieve other precipitation properties, such as, precipitation number concentration, precipitation liquid water content, number concentration, size and width. The overall statistics and distribution of these retrieved precipitation properties below the cloud base, also compare well with in situ estimates from the sawtooth below-cloud segments. This good performance gives us some confidence in using these retrieval techniques for SO stratocumulus, including in our recently published manuscript that examines coalescence scavenging in SO stratocumulus [Kang et al., 2022].

Despite the good retrieval performance overall, there are important caveats. When developing the power-law relationships between reflectivity (Z) and rain rate (R) following $Z = aR^b$ we found the b exponent varied little with altitude and had a value around 1.3 to 1.4. This is similar to values obtained in previous studies for stratocumulus in other regions (Comstock et al., 2004; vanZanten et al., 2005). The a coefficient, on the other hand, increases as one moves from the cloud layer to the surface. In general, one can derived a power-law relationship between Z and R based on the assumption of a modified gamma distribution (e.g., Rosenfeld and Ulbrich 2003) and doing so shows that one should expected the a coefficient to depend on the total droplet number concentration. Given the vertical variations in the precipitation droplet number concentration (see Figures 10 and 11), the vertical variation in the a coefficient is not surprising. But such also hints that the a coefficient may well vary with the accumulation mode aerosol concentration or other factors than control the cloud droplet number concentration. So Z-R relationships should be used with some caution in studies intending to establish relationships between rain rates and aerosols. We also find that the derived the derived Z-R relationships are sensitive to whether ones exclude drops with diameters around 10-40 μm when in cloud, because these drops make a non-trivial contribution to drizzle flux, as perhaps first noted by Nicholls (1984). Our analysis suggests that below-cloud Z-R equations should be applied with caution to in-cloud reflectivity measurements, and should be expected to underestimate the total liquid water flux in cloud.

Comparing the ZV retrieval with radar-lidar retrieval shows that both retrievals capture the mean vertical structure of precipitation microphysics below cloud. Based on in situ data and retrievals, we found that rain rate, precipitation number concentration (N_{precip}), precipitation liquid water (LWC_{precip}) all decreases as one get closer to the surface, while precipitation liquid water content weighted mean diameter (D_{precip}) and width(σ_{precip}) increases. The e-folding distance over which the rain rate decrease to 1/e (37%) of its initial value is about 260m for radar-lidar retrieval and 340 m for ZV retrieval. However, we find that both D_0 and N_{precip} from the ZV retrieval have less spatial variability than that from the radar-lidar retrieval, and assuming a shape factor of $\mu = 0$, results in the ZV retrieved mean D_0 being a bit too small and N_{precip} being too large as compared to the radar-lidar retrieval. This is because the shape factor is not constant and in particular, because the shape factor in the stronger precipitation shafts below the thicker portion of the clouds should be larger than zero (because the precipitation DSD is narrower with a more well defined peaked rather than a broad exponential-like distribution).

This study also explored rain rate dependence on cloud depth and aerosol concentration. Rain rate at cloud base (R_{CB}) increases with cloud depth (H) and decreases with aerosol concentration (N_a). Using a least-squares regression, we found R_{CB} varies as $H^{3.6}\ N_a^{-1}$, which is broadly consistent with estimates for stratocumulus in previous studies over other regions (vanZanten et al., 2005; Pawlowska & Brenguier, 2003; Lu et al., 2009; Mann et al., 2014; Lu et al., 2009; Comstock et al., 2004). However as noted in section 6, our results differ with the satellite-based estimates for the SO by Mace and Avey (2007), hereafter M17, who suggest an exponent of -0.32 for the aerosol concentration based on satellite retrievals. M17 also noted that their estimates differ from previous studies in other regions. There are a variety of potential reasons for the different results in our study and in M17. The first obvious reason is different data sources. Our study used in situ measured N_a and retrieved rain rate with airborne radar and lidar measurements, while M17 used N_d, liquid water path and rain rate derived from MODIS and Cloudsat based on an optimal estimation algorithm. Another reason might be different cloud populations; where in our study about 80% of the clouds are cold-topped, M17 restricted their analysis to warm-topped clouds. Data collected during the Macquarie Island Cloud and Radiation Experiment (MICRE), suggest that warm topped SO clouds are geometrically thinner and closer to the surface than cold-topped clouds [Tansey et al., 2023, submitted]. As-is, we end this study here, leaving a regime-dependent analysis of precipitation susceptibility for a future study. As more data is collected, including in future campaigns such as the upcoming Clouds And Precipitation Experiment at Kennaook (CAPE-K) that will begin in March 2024, the aerosol sensitivity of low altitude SO clouds is certain to be focus of future multi- or cross-experiments studies.

Acknowledgments

This work was supported by the U.S. National Science Foundation on grant AGS-2124993. We would like to thank the contribution from the many individuals and teams associated with the NCAR Earth Observing Laboratory, SOCRATES Science and Aircraft Instrument Teams. We thank Dr. Ulrike Romatschke for helping with radar data processing. We also would like to thank open-source codes such as miepython and CloudnetPy.

Open Research

The authors would like to acknowledge the SOCRATES Project for providing data through the SOCRATES Data Archive Center (SDAC) at NCAR's Earth Observing Laboratory: (1) low rate (1 Hz) navigation, state parameter, and microphysics flight-level data (contain data from many probes, including CDP and UHSAS) version 1.4 https://data.eol.ucar.edu/dataset/552.002; (2) 2DS data version 1.1 (1 Hz) https://data.eol.ucar.edu/dataset/552.047; (3) HCR radar and HSRL lidar moments data (2 Hz) https://data.eol.ucar.edu/dataset/552.034. Miepython is avaliable at https://miepython.readthedocs.io/en/latest/.

References

Arabzadeh, A., Ehsani, M. R., Guan, B., Heflin, S., & Behrangi, A. (2020). Global Intercomparison of Atmospheric Rivers Precipitation in Remote Sensing and Reanalysis Products. *Journal of Geophysical Research: Atmospheres*, *125*(21), e2020JD033021. https://doi.org/10.1029/2020JD033021

Bai, H., Gong, C., Wang, M., Zhang, Z., & L'Ecuyer, T. (2018). Estimating precipitation susceptibility in warm marine clouds using multi-sensor aerosol and cloud products from A-Train satellites. *Atmospheric Chemistry and Physics*, *18*(3), 1763–1783. https://doi.org/10.5194/acp-18-1763-2018

Beard, K. V. (1976). Terminal Velocity and Shape of Cloud and Precipitation Drops Aloft. *Journal of the Atmospheric Sciences*, *33*(5), 851–864. https://doi.org/10.1175/1520-0469(1976)033<0851:TVASOC>2.0.CO;2

Behrangi, A., Lebsock, M., Wong, S., & Lambrigtsen, B. (2012). On the quantification of oceanic rainfall using spaceborne sensors. *Journal of Geophysical Research: Atmospheres*, *117*(D20). https://doi.org/10.1029/2012JD017979

Behrangi, A., Stephens, G., Adler, R. F., Huffman, G. J., Lambrigtsen, B., & Lebsock, M. (2014). An Update on the Oceanic Precipitation Rate and Its Zonal Distribution in Light of Advanced Observations from Space. *Journal of Climate*, *27*(11), 3957–3965. https://doi.org/10.1175/JCLI-D-13-00679.1

Bellouin, N., Quaas, J., Gryspeerdt, E., Kinne, S., Stier, P., Watson-Parris, D., et al. (2020). Bounding Global Aerosol Radiative Forcing of Climate Change. *Reviews of Geophysics*, *58*(1), e2019RG000660. https://doi.org/10.1029/2019RG000660

Bjordal, J., Storelvmo, T., Alterskjær, K., & Carlsen, T. (2020). Equilibrium climate sensitivity above 5 °C plausible due to state-dependent cloud feedback. Nature Geoscience, 13(11), 718–721. https://doi.org/10.1038/s41561-020-00649-1

Bodas-Salcedo, A., Hill, P. G., Furtado, K., Williams, K. D., Field, P. R., Manners, J. C., et al. (2016). Large Contribution of Supercooled Liquid Clouds to the Solar Radiation Budget of the Southern Ocean. *Journal of Climate*, *29*(11), 4213–4228. https://doi.org/10.1175/JCLI-D-15-0564.1

Bohren, C. F., & Huffman, D. R. (1983). Absorption and scattering of light by small particles. Weinheim: Wiley : Wiley Online Library.

Bromwich, D. H., Nicolas, J. P., & Monaghan, A. J. (2011). An Assessment of Precipitation Changes over Antarctica and the Southern Ocean since 1989 in Contemporary Global Reanalyses. *Journal of Climate*, *24*(16), 4189–4209. https://doi.org/10.1175/2011JCLI4074.1

Cesana, G. V., Khadir, T., Chepfer, H., & Chiriaco, M. (2022). Southern Ocean Solar Reflection Biases in CMIP6 Models Linked to Cloud Phase and Vertical Structure Representations. *Geophysical Research Letters*, *49*(22), e2022GL099777. https://doi.org/10.1029/2022GL099777

Comstock, K. K., Wood, R., Yuter, S. E., & Bretherton, C. S. (2004). Reflectivity and rain rate in and below drizzling stratocumulus. *Quarterly Journal of the Royal Meteorological Society*, *130*(603), 2891–2918. https://doi.org/10.1256/qj.03.187

de Lavergne, C., Palter, J. B., Galbraith, E. D., Bernardello, R., & Marinov, I. (2014). Cessation of deep convection in the open Southern Ocean under anthropogenic climate change. *Nature Climate Change*, *4*(4), 278–282. https://doi.org/10.1038/nclimate2132

DMT. (2013). Ultra high sensitivity aerosol spectrometer (UHSAS) Operator Manual.

Eastman, R., Lebsock, M., & Wood, R. (2019). Warm Rain Rates from AMSR-E 89-GHz Brightness Temperatures Trained Using CloudSat Rain-Rate Observations. Journal of Atmospheric and Oceanic Technology, 36(6), 1033–1051. https://doi.org/10.1175/JTECH-D-18-0185.1

Ellis, S. M., Tsai, P., Burghart, C., Romatschke, U., Dixon, M., Vivekanandan, J., et al. (2019). Use of the Earth's Surface as a Reference to Correct Airborne Nadir-Looking Radar Radial Velocity Measurements for Platform Motion. Journal of Atmospheric and Oceanic Technology, 36(7), 1343–1360. https://doi.org/10.1175/JTECH-D-19-0019.1

Ellis, T. D., L'Ecuyer, T., Haynes, J. M., & Stephens, G. L. (2009). How often does it rain over the global oceans? The perspective from CloudSat. *Geophysical Research Letters*, *36*(3). https://doi.org/10.1029/2008GL036728

Eloranta, E. E. (2005). High Spectral Resolution Lidar. In C. Weitkamp (Ed.), *Lidar: Range-Resolved Optical Remote Sensing of the Atmosphere* (pp. 143–163). New York, NY: Springer. https://doi.org/10.1007/0-387-25101-4_5

Feingold, G., McComiskey, A., Rosenfeld, D., & Sorooshian, A. (2013). On the relationship between cloud contact time and precipitation susceptibility to aerosol. *Journal of Geophysical Research: Atmospheres*, *118*(18), 10,544-10,554. https://doi.org/10.1002/jgrd.50819

Frisch, A. S., Fairall, C. W., & Snider, J. B. (1995). Measurement of Stratus Cloud and Drizzle Parameters in ASTEX with a Kα-Band Doppler Radar and a Microwave Radiometer. *Journal of the Atmospheric Sciences*, *52*(16), 2788–2799. https://doi.org/10.1175/1520-0469(1995)052<2788:MOSCAD>2.0.CO;2

Frölicher, T. L., Sarmiento, J. L., Paynter, D. J., Dunne, J. P., Krasting, J. P., & Winton, M. (2015). Dominance of the Southern Ocean in Anthropogenic Carbon and Heat Uptake in CMIP5 Models. *Journal of Climate*, *28*(2), 862–886. https://doi.org/10.1175/JCLI-D-14-00117.1

Fyfe, J. C., Gillett, N. P., & Marshall, G. J. (2012). Human influence on extratropical Southern Hemisphere summer precipitation. *Geophysical Research Letters*, *39*(23). https://doi.org/10.1029/2012GL054199

Ghate, V. P., & Cadeddu, M. P. (2019). Drizzle and turbulence below closed cellular marine stratocumulus clouds. Journal of Geophysical Research-Atmospheres, 124(11), 2018JD030141. https://doi.org/10.1029/2018JD030141

Grecu, M., Olson, W. S., Munchak, S. J., Ringerud, S., Liao, L., Haddad, Z., et al. (2016). The GPM Combined Algorithm. *Journal of Atmospheric and Oceanic Technology*, *33*(10), 2225–2245. https://doi.org/10.1175/JTECH-D-16-0019.1

Hamilton, D. S., Lee, L. A., Pringle, K. J., Reddington, C. L., Spracklen, D. V., & Carslaw, K. S. (2014). Occurrence of pristine aerosol environments on a polluted planet. *Proceedings of the National Academy of Sciences*, *111*(52), 18466–18471. https://doi.org/10.1073/pnas.1415440111

Hayden, L., & Liu, C. (2018). A Multiyear Analysis of Global Precipitation Combining CloudSat and GPM Precipitation Retrievals. *Journal of Hydrometeorology*, *19*(12), 1935–1952. https://doi.org/10.1175/JHM-D-18-0053.1

Haynes, J. M., L'Ecuyer, T. S., Stephens, G. L., Miller, S. D., Mitrescu, C., Wood, N. B., & Tanelli, S. (2009). Rainfall retrieval over the ocean with spaceborne W-band radar.

Journal of Geophysical Research: Atmospheres, *114*(D8). https://doi.org/10.1029/2008JD009973

Kang, L., Marchand, R. T., Wood, R., & McCoy, I. L. (2022). Coalescence Scavenging Drives Droplet Number Concentration in Southern Ocean Low Clouds. *Geophysical Research Letters*, *49*(7), e2022GL097819. https://doi.org/10.1029/2022GL097819

Kang, L., Marchand, R., & Smith, W. (2021). Evaluation of MODIS and Himawari-8 Low Clouds Retrievals Over the Southern Ocean With In Situ Measurements From the SOCRATES Campaign. *Earth and Space Science*, *8*(3), e2020EA001397. https://doi.org/10.1029/2020EA001397

Khatiwala, S., Primeau, F., & Hall, T. (2009). Reconstruction of the history of anthropogenic CO2 concentrations in the ocean. *Nature*, *462*(7271), 346–349. https://doi.org/10.1038/nature08526

Klepp, C., Michel, S., Protat, A., Burdanowitz, J., Albern, N., Kähnert, M., et al. (2018). OceanRAIN, a new in-situ shipboard global ocean surface-reference dataset of all water cycle components. *Scientific Data*, *5*(1), 180122. https://doi.org/10.1038/sdata.2018.122

Lance, S., Brock, C. A., Rogers, D., & Gordon, J. A. (2010). Water droplet calibration of the Cloud Droplet Probe (CDP) and in-flight performance in liquid, ice and mixed-phase clouds during ARCPAC. *Atmospheric Measurement Techniques*, *3*(6), 1683–1706. https://doi.org/10.5194/amt-3-1683-2010

Lang, F., Huang, Y., Siems, S. T., & Manton, M. J. (2018). Characteristics of the Marine Atmospheric Boundary Layer Over the Southern Ocean in Response to the Synoptic Forcing. *Journal of Geophysical Research: Atmospheres*, *123*(15), 7799–7820. https://doi.org/10.1029/2018JD028700

Lee, L. A., Reddington, C. L., & Carslaw, K. S. (2016). On the relationship between aerosol model uncertainty and radiative forcing uncertainty. *Proceedings of the National Academy of Sciences*, *113*(21), 5820–5827. https://doi.org/10.1073/pnas.1507050113

Lu, M.-L., Sorooshian, A., Jonsson, H. H., Feingold, G., Flagan, R. C., & Seinfeld, J. H. (2009). Marine stratocumulus aerosol-cloud relationships in the MASE-II experiment: Precipitation susceptibility in eastern Pacific marine stratocumulus. *Journal of Geophysical Research: Atmospheres*, *114*(D24). https://doi.org/10.1029/2009JD012774

Mace, G. G., & Avey, S. (2017). Seasonal variability of warm boundary layer cloud and precipitation properties in the Southern Ocean as diagnosed from A-Train data. Journal of Geophysical Research: Atmospheres, 122(2), 1015–1032. https://doi.org/10.1002/2016JD025348

Mace, G. G., & Protat, A. (2018). Clouds over the Southern Ocean as Observed from the R/V Investigator during CAPRICORN. Part I: Cloud Occurrence and Phase Partitioning. Journal of Applied Meteorology and Climatology, 57(8), 1783–1803. https://doi.org/10.1175/JAMC-D-17-0194.1

Mace, G. G., Heymsfield, A. J., & Poellot, M. R. (2002). On retrieving the microphysical properties of cirrus clouds using the moments of the millimeter-wavelength Doppler spectrum. *Journal of Geophysical Research: Atmospheres*, *107*(D24), AAC 22-1-AAC 22-26. https://doi.org/10.1029/2001JD001308

Mann, J. A. L., Christine Chiu, J., Hogan, R. J., O'Connor, E. J., L'Ecuyer, T. S., Stein, T. H. M., & Jefferson, A. (2014). Aerosol impacts on drizzle properties in warm clouds from ARM Mobile Facility maritime and continental deployments. *Journal of Geophysical Research: Atmospheres*, *119*(7), 4136–4148. https://doi.org/10.1002/2013JD021339

Manton, M. J., Huang, Y., & Siems, S. T. (2020). Variations in Precipitation across the Southern Ocean. *Journal of Climate*, *33*(24), 10653–10670. https://doi.org/10.1175/JCLI-D-20-0120.1

Marchand, R. T., Ackerman, T. P., & Moroney, C. (2007). An assessment of Multiangle Imaging Spectroradiometer (MISR) stereo-derived cloud top heights and cloud top winds using ground-based radar, lidar, and microwave radiometers. *Journal of Geophysical Research: Atmospheres*, *112*(D6). https://doi.org/10.1029/2006JD007091

Marchand, R., Mace, G. G., Ackerman, T., & Stephens, G. (2008). Hydrometeor Detection Using Cloudsat—An Earth-Orbiting 94-GHz Cloud Radar. *Journal of Atmospheric and Oceanic Technology*, *25*(4), 519–533. https://doi.org/10.1175/2007JTECHA1006.1

McCoy, I. L., McCoy, D. T., Wood, R., Regayre, L., Watson-Parris, D., Grosvenor, D. P., et al. (2020). The hemispheric contrast in cloud microphysical properties constrains aerosol forcing. *Proceedings of the National Academy of Sciences of the United States of America*, *117*(32), 18998–19006. https://doi.org/10.1073/pnas.1922502117

McFarquhar, G. M., Bretherton, C. S., Marchand, R., Protat, A., DeMott, P. J., Alexander, S. P., et al. (2021). Observations of Clouds, Aerosols, Precipitation, and Surface Radiation over the Southern Ocean: An Overview of CAPRICORN, MARCUS, MICRE, and SOCRATES. *Bulletin of the American Meteorological Society*, *102*(4), E894–E928. https://doi.org/10.1175/BAMS-D-20-0132.1

Mitrescu, C., L'Ecuyer, T., Haynes, J., Miller, S., & Turk, J. (2010). CloudSat Precipitation Profiling Algorithm—Model Description. *Journal of Applied Meteorology and Climatology*, *49*(5), 991–1003. https://doi.org/10.1175/2009JAMC2181.1

Mohrmann, J., Wood, R., McGibbon, J., Eastman, R., & Luke, E. (2018). Drivers of Seasonal Variability in Marine Boundary Layer Aerosol Number Concentration Investigated Using a Steady State Approach. *Journal of Geophysical Research: Atmospheres*, *123*(2), 1097–1112. https://doi.org/10.1002/2017JD027443

Montoya Duque, E., Huang, Y., Siems, S. T., May, P. T., Protat, A., & McFarquhar, G. M. (2022). A Characterization of Clouds and Precipitation Over the Southern Ocean From Synoptic to Micro Scales During the CAPRICORN Field Campaigns. *Journal of Geophysical Research: Atmospheres*, *127*(17), e2022JD036796. https://doi.org/10.1029/2022JD036796

Mülmenstädt, J., Salzmann, M., Kay, J. E., Zelinka, M. D., Ma, P.-L., Nam, C., et al. (2021). An underestimated negative cloud feedback from cloud lifetime changes. *Nature Climate Change*, *11*(6), 508–513. https://doi.org/10.1038/s41558-021-01038-1

NCAR/EOL HCR Team. 2022. SOCRATES: NCAR HCR radar moments data. Version 3.1. UCAR/NCAR - Earth Observing Laboratory. https://doi.org/10.5065/D68914PH.

Nicholls, S. (1984). The dynamics of stratocumulus: Aircraft observations and comparisons with a mixed layer model. Quarterly Journal of the Royal Meteorological Society, 110(466), 783–820. https://doi.org/10.1002/qj.49711046603

Nicolas, J. P., & Bromwich, D. H. (2011). Precipitation Changes in High Southern Latitudes from Global Reanalyses: A Cautionary Tale. *Surveys in Geophysics*, *32*(4), 475–494. https://doi.org/10.1007/s10712-011-9114-6

O'Connor, E. J., Hogan, R. J., & Illingworth, A. J. (2005). Retrieving Stratocumulus Drizzle Parameters Using Doppler Radar and Lidar. *Journal of Applied Meteorology and Climatology*, *44*(1), 14–27. https://doi.org/10.1175/JAM-2181.1

Orr, B. W., & Kropfli, R. A. (1999). A Method for Estimating Particle Fall Velocities from Vertically Pointing Doppler Radar. *Journal of Atmospheric and Oceanic Technology*, *16*(1), 29–37. https://doi.org/10.1175/1520-0426(1999)016<0029:AMFEPF>2.0.CO;2

Pauling, A. G., Bitz, C. M., Smith, I. J., & Langhorne, P. J. (2016). The Response of the Southern Ocean and Antarctic Sea Ice to Freshwater from Ice Shelves in an Earth System Model. *Journal of Climate*, *29*(5), 1655–1672. https://doi.org/10.1175/JCLI-D-15-0501.1

Pawlowska, H., & Brenguier, J.-L. (2003). An observational study of drizzle formation in stratocumulus clouds for general circulation model (GCM) parameterizations. *Journal of Geophysical Research: Atmospheres*, *108*(D15). https://doi.org/10.1029/2002JD002679

Protat, A., Klepp, C., Louf, V., Petersen, W. A., Alexander, S. P., Barros, A., et al. (2019a). The Latitudinal Variability of Oceanic Rainfall Properties and Its Implication for Satellite Retrievals: 1. Drop Size Distribution Properties. *Journal of Geophysical Research: Atmospheres*, *124*(23), 13291–13311. https://doi.org/10.1029/2019JD031010

Protat, A., Klepp, C., Louf, V., Petersen, W. A., Alexander, S. P., Barros, A., et al. (2019b). The Latitudinal Variability of Oceanic Rainfall Properties and Its Implication for Satellite Retrievals: 1. Drop Size Distribution Properties. *Journal of Geophysical Research: Atmospheres*, *124*(23), 13291–13311. https://doi.org/10.1029/2019JD031010

Romatschke, U., Dixon, M., Tsai, P., Loew, E., Vivekanandan, J., Emmett, J., & Rilling, R. (2021). The NCAR Airborne 94-GHz Cloud Radar: Calibration and Data Processing. Data, 6(6), 66. https://doi.org/10.3390/data6060066

Rosenfeld, D., & Ulbrich, C. W. (2003). Cloud Microphysical Properties, Processes, and Rainfall Estimation Opportunities. *Meteorological Monographs*, *30*(52), 237–258. https://doi.org/10.1175/0065-9401(2003)030<0237:CMPPAR>2.0.CO;2

Sanchez, K. J., Roberts, G. C., Saliba, G., Russell, L. M., Twohy, C., Reeves, J. M., et al. (2021). Measurement report: Cloud processes and the transport of biological emissions affect southern ocean particle and cloud condensation nuclei concentrations. *Atmospheric Chemistry and Physics*, *21*(5), 3427–3446. https://doi.org/10.5194/acp-21-3427-2021

Sarkar, M., Zuidema, P., & Ghate, V. (2021). Clarifying Remotely Retrieved Precipitation of Shallow Marine Clouds from the NSF/NCAR Gulfstream V. *Journal of Atmospheric and Oceanic Technology*, *38*(9), 1657–1670. https://doi.org/10.1175/JTECH-D-20-0166.1

Sarmiento, J. L., Hughes, T. M. C., Stouffer, R. J., & Manabe, S. (1998). Simulated response of the ocean carbon cycle to anthropogenic climate warming. *Nature*, *393*(6682), 245–249. https://doi.org/10.1038/30455

Sassen, K., & Liao, L. (1996). Estimation of Cloud Content by W-Band Radar. *Journal of Applied Meteorology and Climatology*, *35*(6), 932–938. https://doi.org/10.1175/1520-0450(1996)035<0932:EOCCBW>2.0.CO;2

Schwartz, M. C., Ghate, V. P., Albrecht, B. A., Zuidema, P., Cadeddu, M. P., Vivekanandan, J., et al. (2019). Merged Cloud and Precipitation Dataset from the HIAPER GV for the Cloud System Evolution in the Trades (CSET) Campaign. *Journal of Atmospheric and Oceanic Technology*, *36*(6), 921–940. https://doi.org/10.1175/JTECH-D-18-0111.1

Seto, S., Iguchi, T., & Oki, T. (2013). The Basic Performance of a Precipitation Retrieval Algorithm for the Global Precipitation Measurement Mission's Single/Dual-Frequency Radar Measurements. *IEEE Transactions on Geoscience and Remote Sensing*, *51*(12), 5239–5251. https://doi.org/10.1109/TGRS.2012.2231686

Smalley, K. M., Lebsock, M. D., Eastman, R., Smalley, M., & Witte, M. K. (2022). A Lagrangian analysis of pockets of open cells over the southeastern Pacific. *Atmospheric Chemistry and Physics*, *22*(12), 8197–8219. https://doi.org/10.5194/acp-22-8197-2022

Stephens, G. L., L'Ecuyer, T., Forbes, R., Gettelmen, A., Golaz, J.-C., Bodas-Salcedo, A., et al. (2010). Dreary state of precipitation in global models. *Journal of Geophysical Research: Atmospheres*, *115*(D24). https://doi.org/10.1029/2010JD014532

Swart, N. C., Gille, S. T., Fyfe, J. C., & Gillett, N. P. (2018). Recent Southern Ocean warming and freshening driven by greenhouse gas emissions and ozone depletion. *Nature Geoscience*, *11*(11), 836–841. https://doi.org/10.1038/s41561-018-0226-1

Tan, I., Storelvmo, T., & Zelinka, M. D. (2016). Observational constraints on mixed-phase clouds imply higher climate sensitivity. *Science*, *352*(6282), 224–227. https://doi.org/10.1126/science.aad5300

Tansey, E., Marchand, R. T., Alexander, S. P., Klekociuk, A. R., & Protat, A. (2023). Southern Ocean low cloud and precipitation phase observed during the Macquarie Island Cloud and Radiation Experiment (MICRE) (preprint). Preprints. https://doi.org/10.22541/essoar.168394768.89694625/v1

Tansey, E., Marchand, R., Protat, A., Alexander, S. P., & Ding, S. (2022). Southern Ocean Precipitation Characteristics Observed From CloudSat and Ground Instrumentation During the Macquarie Island Cloud & Radiation Experiment (MICRE): April 2016 to March 2017. *Journal of Geophysical Research: Atmospheres*, *127*(5), e2021JD035370. https://doi.org/10.1029/2021JD035370

Terai, C. R., Wood, R., Leon, D. C., & Zuidema, P. (2012). Does precipitation susceptibility vary with increasing cloud thickness in marine stratocumulus? *Atmospheric Chemistry and Physics*, *12*(10), 4567–4583. https://doi.org/10.5194/acp-12-4567-2012

Trenberth, K. E., & Fasullo, J. T. (2010). Simulation of Present-Day and Twenty-First-Century Energy Budgets of the Southern Oceans. *Journal of Climate*, *23*(2), 440–454. https://doi.org/10.1175/2009JCLI3152.1

UCAR/NCAR - Earth Observing Laboratory. 2022. SOCRATES: Low Rate (LRT - 1 sps) Navigation, State Parameter, and Microphysics Flight-Level Data. Version 1.4. UCAR/NCAR - Earth Observing Laboratory. https://doi.org/10.5065/D6M32TM9.

Vali, G., Kelly, R. D., French, J., Haimov, S., Leon, D., McIntosh, R. E., & Pazmany, A. (1998). Finescale Structure and Microphysics of Coastal Stratus. *Journal of the Atmospheric Sciences*, *55*(24), 3540–3564. https://doi.org/10.1175/1520-0469(1998)055<3540:FSAMOC>2.0.CO;2

vanZanten, M. C., Stevens, B., Vali, G., & Lenschow, D. H. (2005). Observations of Drizzle in Nocturnal Marine Stratocumulus. *Journal of the Atmospheric Sciences*, *62*(1), 88–106. https://doi.org/10.1175/JAS-3355.1

Vivekanandan, J., Ellis, S., Tsai, P., Loew, E., Lee, W.-C., Emmett, J., et al. (2015). A wing pod-based millimeter wavelength airborne cloud radar. *Geoscientific Instrumentation, Methods and Data Systems*, *4*(2), 161–176. https://doi.org/10.5194/gi-4-161-2015

von Terzi, L., Dias Neto, J., Ori, D., Myagkov, A., & Kneifel, S. (2022). Ice microphysical processes in the dendritic growth layer: a statistical analysis combining multi-frequency and polarimetric Doppler cloud radar observations. *Atmospheric Chemistry and Physics*, *22*(17), 11795–11821. https://doi.org/10.5194/acp-22-11795-2022

Wang, H., & Feingold, G. (2009). Modeling Mesoscale Cellular Structures and Drizzle in Marine Stratocumulus. Part I: Impact of Drizzle on the Formation and Evolution of Open

Cells. *Journal of the Atmospheric Sciences*, *66*(11), 3237–3256. https://doi.org/10.1175/2009JAS3022.1

Wilks, D. S. (1997). Resampling Hypothesis Tests for Autocorrelated Fields. *Journal of Climate*, *10*(1), 65–82. https://doi.org/10.1175/1520-0442(1997)010<0065:RHTFAF>2.0.CO;2

Wiscombe, J. (1979). Mie Scattering Calculations: Advances in Technique and Fast, Vector-speed Computer Codes. https://doi.org/10.5065/D6ZP4414

Wood, R. (2005). Drizzle in Stratiform Boundary Layer Clouds. Part II: Microphysical Aspects. *Journal of the Atmospheric Sciences*, *62*(9), 3034–3050. https://doi.org/10.1175/JAS3530.1

Wood, R., Bretherton, C. S., Leon, D., Clarke, A. D., Zuidema, P., Allen, G., & Coe, H. (2011). An aircraft case study of the spatial transition from closed to open mesoscale cellular convection over the Southeast Pacific. *Atmospheric Chemistry and Physics*, *11*(5), 2341–2370. https://doi.org/10.5194/acp-11-2341-2011

Wu, W., McFarquhar, G. 2019. NSF/NCAR GV HIAPER 2D-S Particle Size Distribution (PSD) Product Data. Version 1.1. UCAR/NCAR - Earth Observing Laboratory. https://doi.org/10.26023/8HMG-WQP3-XA0X.

Yamaguchi, T., & Feingold, G. (2015). On the relationship between open cellular convective cloud patterns and the spatial distribution of precipitation. *Atmospheric Chemistry and Physics*, *15*(3), 1237–1251. https://doi.org/10.5194/acp-15-1237-2015

Yang, F., Luke, E. P., Kollias, P., Kostinski, A. B., & Vogelmann, A. M. (2018). Scaling of drizzle virga depth with cloud thickness for marine stratocumulus clouds. Geophysical Research Letters, 45(8), 3746–3753. https://doi.org/10.1029/2018GL077145

Zelinka, M. D., Myers, T. A., McCoy, D. T., Po-Chedley, S., Caldwell, P. M., Ceppi, P., et al. (2020). Causes of Higher Climate Sensitivity in CMIP6 Models. *Geophysical Research Letters*, *47*(1), e2019GL085782. https://doi.org/10.1029/2019GL085782

Zhang, D., Wang, Z., Luo, T., Yin, Y., & Flynn, C. (2017). The occurrence of ice production in slightly supercooled Arctic stratiform clouds as observed by ground-based remote sensors at the ARM NSA site. *Journal of Geophysical Research: Atmospheres*, *122*(5), 2867–2877. https://doi.org/10.1002/2016JD026226

Zhou, X., Atlas, R., McCoy, I. L., Bretherton, C. S., Bardeen, C., Gettelman, A., et al. (2021). Evaluation of Cloud and Precipitation Simulations in CAM6 and AM4 Using Observations Over the Southern Ocean. *Earth and Space Science*, *8*(2), e2020EA001241. https://doi.org/10.1029/2020EA001241

Stratocumulus Precipitation Properties over the Southern Ocean Observed from Aircraft during the SOCRATES campaign

L. Kang[1], R. T. Marchand [1], and R. Wood[1]

[1] Department of Atmospheric Sciences, University of Washington, Seattle, Washington, USA

Corresponding author: Litai Kang (kanglt@uw.edu)

†Additional author notes should be indicated with symbols (current addresses, for example).

Key Points:

- Liquid-phase precipitation retrievals show good agreement with in situ observations and feature the prevalence of light rain
- Reflectivity to rain rate relationships are developed, showing vertical dependence and sensitivity to the intermediate-sized drops
- The below-cloud precipitation phase with radar reflectivity > 0 dBZ is mostly ice, while radar reflectivity < -10 dBZ is mostly liquid

Abstract

Precipitation plays an important role in various processes over the Southern Ocean (SO), ranging from the hydrological cycle to cloud and aerosol processes. The main objective of this study is to characterize SO precipitation properties. We use data from the Southern Ocean Clouds Radiation Aerosol Transport Experimental Study (SOCRATES), and leverage observations from airborne radar, lidar, and in situ probes. For the cold-topped clouds (cloud-top-temperature < 0°C), the phase of precipitation with reflectivity > 0 dBZ is predominately ice, while reflectivity < -10 dBZ is predominately liquid. Liquid-phase precipitation properties are retrieved where radar and lidar are zenith-pointing. The power-law relationships between reflectivity (Z) and rain rate (R) are developed, and the derived Z-R relationships show vertical dependence and sensitivity to the intermediate drops (diameters between 10-40 μm). Using derived Z-R relationships, reflectivity-velocity (ZV) retrieval method, and a radar-lidar retrieval method, we derive rain rate and other precipitation properties. The retrieved rain rate from all three methods shows good agreement with in-situ aircraft estimates. Rain rate features the prevalence of light precipitation (<0.1 mm hr^{-1}). We examine the vertical distribution of precipitation properties, and found that rain rate, precipitation number concentration, precipitation liquid water all decreases as one gets closer to the surface, while precipitation size and width increases. We also examine how cloud base rain rate (R_{CB}) depends on cloud depth (H) and aerosol concentration (N_a) for particles with diameter greater than 70nm, and we find a linear relationship between R_{CB} and $H^{3.6}\ N_a^{-1}$.

Plain Language Summary

Precipitation plays an important role over the Southern Ocean (SO), such as transferring water from air to ocean, and affect cloud and aerosols (tiny airborne particles). The goal of this study is to characterize SO precipitation properties using aircraft data. Aircraft had instruments that can count the number of droplets, as well as lidar and radar, which are remote sensing devices that use laser light and microwave waves respectively to detect objects. Using information from lidar, we can distinguish precipitation phase, and we found that ice precipitation is more frequent when observed radar reflectivity is larger than certain threshold. We derived relationships between rain rate and radar variable that can be used for future research. We also calculated precipitation properties and found our results compares well with direct measurements from the aircraft. Rain rate we calculated features the prevalence of light precipitation. We also studied how precipitation properties very vertically, and found that as one gets closer to the surface, there is a decrease in precipitation number and water, while there is an increase in the size overall. We also found that rain rate depends on how thick the clouds are and on the number of aerosols.

1 Introduction

Surrounding Antarctica, the Southern Ocean (SO) is the second smallest of the five ocean basins, yet it plays an outsized role in the climate system. The SO is estimated to account for about 75% of the oceanic heat uptake and about 30-40% of the carbon uptake (Frölicher et al., 2015; Khatiwala et al., 2009), and thus act as a strong buffer against climate change. Due to the lack of anthropogenic aerosols, the SO is also a pristine environment, and it has been argued that SO observations can be used as a present-day proxy for pre-industrial conditions as regards trying to constrain anthropogenic aerosol effects (Hamilton et al., 2014; McCoy et al., 2020), which remain a large source of uncertainty in the climate projections (Lee et al., 2016; Bellouin et al., 2020). More generally, SO clouds, especially low clouds, also have attracted much research interest in recent years because of their importance to the global radiative energy budget (Trenberth and Fasullo, 2010; Bodas-Salcedo et al., 2016; Cesana et al., 2022) as well as global cloud feedbacks and global climate sensitivity (Tan et al., 2016; Zelinka et al., 2020; Mülmenstädt et al., 2021).

Precipitation impacts stratocumulus behavior via complex feedbacks that operate on both macrophysical and microphysical scales (Wood, 2012), and has been found to be a key player in the transition of stratocumulus regimes, from closed cells to open cells, and the maintenance of open cells, at least in subtropical stratocumulus (Wang and Feingold, 2009; Yamaguchi and Feingold, 2015; Smalley et al., 2022). Moreover, recent studies highlight the importance of precipitation formation as a dominant sink of cloud condensation nuclei and its control on the cloud droplet number over the SO (McCoy et al., 2020; Kang et al., 2022). Despite the importance of precipitation in low clouds, many climate models and reanalysis data struggle to represent accurately precipitation, including over the SO (Zhou et al., 2021). Mülmenstädt et al., (2021) point out that precipitation biases persist in CMIP6 models, with warm clouds precipitating too frequently, thus shortening the cloud lifetime and underestimating their cooling effect. This problem is especially pernicious for the SO because the error grows in importance, with a reduction in mixed-phase clouds as the climate warms (Bjordal et al., 2020).

Due to the remoteness of SO and a general lack of surface and in situ observations, satellite observations have long been an indispensable tool to study SO precipitation. Arguably the best available source of satellite data on SO precipitation rates is CloudSat (W-band radar), which has greater sensitivity to light precipitation than passive sensors (Tansey et al., 2022, Eastman et al., 2019). CloudSat has provided an unprecedentedly broad picture of SO precipitation: Ellis et al. (2009) showed that the precipitation occurrence frequency peaks around 50°-60°S; Mitrescu et al. (2010) found that the SO has a high occurrence of very light precipitation with rain rates smaller than 1 mm h^{-1} having a frequency of 15%; Mace and Avey (2017) using both CloudSat and Moderate Resolution Imaging Spectroradiometer (MODIS) data found that precipitation processes in SO warm clouds vary seasonally with a stronger precipitation susceptibility to cloud droplet number in winter. Although compared to other satellite measurements, CloudSat better detects light precipitation and is better able to determine the rain rate, CloudSat is nonetheless affected by ground clutter which severely corrupts the reflectivity measurements within about 750 m of the surface (Marchand et al.,2008). CloudSat precipitation retrievals are also largely limited to situations where the measured near-surface (750 to 1000m) reflectivity is larger than -15 dBZ (Haynes et al., 2009), although the precipitation is often observed falling for SO clouds with reflectivity factors less than -15 dBZ (e.g., Mace and Protat 2018). As shown by Tansey et al. (2022), who evaluated CloudSat retrievals using surface precipitation measurements during the Macquarie Island Cloud Radiation Experiment (MICRE), the CloudSat 2C-Precip-Column product misses most precipitation with a precipitation rate less than 0.5 mm hr^{-1}. In addition, CloudSat radar reflectivity measurements provide very limited information regarding the phase of the precipitation. The current operational CloudSat precipitation products categorize precipitation into liquid, snow, or mixed phase based largely on temperature profiles extracted from ECMWF analysis and identifying melting layers, rather than any directly measured quantity.

In the face of biases and uncertainty in satellite retrievals and modeling, precipitation observations from multiple sources such as islands, ships, and aircraft provide us with an important opportunity to obtain a more detailed view of SO precipitation. Such precipitation observations were made in several recent collaborative field campaigns (McFarquhar et al.,2021), including the aforementioned Macquarie Island Cloud Radiation Experiment (MICRE) during 2016-2018, the Clouds Aerosols Precipitation Radiation and atmospheric Composition over the Southern Ocean (CAPRICORN) campaign in 2016 and 2018, the Measurements of Aerosol, Radiation, and Clouds over the Southern Ocean (MARCUS) campaign during 2017-2018, and the Southern Ocean Cloud Radiation and Aerosol Transport Experimental Study (SOCRATES) during Jan-Feb 2018. For example, Tansey et al. (2022) created a 1-year "blended" surface precipitation dataset (which combines W-band radar, tipping buck and disdrometer data) for MICRE and used these data to study the diurnal, synoptic and seasonal variability of near-surface precipitation. These authors found that total accumulation was comprised of about 74% rain, 16% ice or mixed phase precipitation, and 10% small particle precipitation. In a study based on the CAPRICORN datasets. Montoya Duque et al. (2022), applied a K-means clustering technique to radiosonde data to classify the atmosphere into seven thermodynamic clusters, and found that the highest occurrence of surface precipitation was associated with warm frontal clusters and high-latitude cyclone clusters(poleward of the polar front near cyclones), with warm rain dominating in the former and the largest fraction of snow in the latter. Shipborne precipitation observations from CAPRICORN have also been included along with observations from other research vessels in the Ocean Rain and Ice-Phase Precipitation Measurement Network (OceanRAIN), the first global and comprehensive along-track in-situ water cycle surface reference dataset (Klepp et al., 2018). Protat et al. (2019a,b) used OceanRAIN data to investigate discrepancies among satellite products at high latitudes and found large latitudinal and convective-stratiform variability in the drop size distribution (DSD). Protat et al. (2019a) pointed out that the Southern hemisphere high latitudes stood out as regions with a systematically higher frequency of occurrence of light precipitation with rates < 1 mm h^{-1} and difference in the shape parameter μ in the precipitation drop size distribution (DSD), with high-latitude and midlatitude μ ranging from -1 to 1, which is lower than the assumed μ of 2 or 3 in the Global Precipitation Measurement Mission (GPM) rainfall algorithms (Grecu et al., 2016; Seto et al., 2013). Protat et al. (2019b) found that the Southern Hemisphere high latitude (−67.5°S to −45°S), along with Northern Hemisphere polar latitude bands, stood out with a fundamentally different relationship between radar observables and rainfall properties, such as radar reflectivity to rain rate (Z-R) relationship, mainly because of much lower rain rates over the SO, suggesting that specific relationships are needed for these regions.

In this study, we use data collected during SOCRATES to study the precipitation properties of summertime SO stratocumulus, leveraging observations from airborne W-band HIAPER Cloud Radar (HCR), High Spectral Resolution Lidar (HSRL), and in situ probes. In particular we examine occurrence of liquid and ice phase precipitation, and for liquid precipitation we derived precipitation properties such as rain rate, using a hierarchy of retrieval methods from simple Z-R relationships to more complex radar reflectivity-velocity retrieval (ZV retrieval) and radar-lidar retrievals. We also apply the precipitation observations and retrievals to study the in-and-below cloud precipitation properties and rain rate dependence on cloud depth and aerosol concentration.

This paper is organized as follows: Section 2 introduces the datasets, instruments, as well as the analysis and retrieval methods used in this study. Section 3 provides a campaign overview and discusses phase partitioning. Section 4 examines Z-R relationships and precipitation retrievals and compares these remote sensing data to in situ measurements. Section 5 provides a statistical summary of the precipitation properties, and Section 6 explores the relationship of stratocumulus rain rate with cloud depth and aerosol concentration, ending with conclusions in Section 7.

2 Data and Methods

In this section we introduce the data and methods that we use to characterize in-and-below cloud precipitation properties. Section 2.1 describes the SOCRATES campaign sampling strategies, remote sensors (W-band Cloud Radar, HCR, and High Spectral Resolution Lidar, HSRL), and in situ instruments. Section 2.2 describes how we use in situ data to analyze in-cloud and below-cloud precipitation properties, as well as how we estimate Z-R relationships. In section 2.3, we describe reflectivity-velocity (ZV) and radar-lidar retrievals.

2.1 Instrumentation and data

In this study, we use data collected during the SOCRATES campaign to study the precipitation properties of stratocumulus. The SOCRATES campaign happened in January-February 2018 (McFarquhar et al., 2021), when the NSF/NCAR Gulfstream GV aircraft conducted 15 research flights over the SO. After taking off from Hobart (Tasmania), the aircraft typically flew south at high altitude and then descended to just above cloud top for several 10's of minutes, before heading back towards Hobart. On the return, the aircraft would descend into low cloud and sample aerosols, clouds, and precipitation with a repeating series of activities that included in-, below-, and above-cloud level legs (where the aircraft flew at a nearly fixed altitude), as well as sawtooth legs (where the aircraft ascended or descended through the cloud layer). Supplementary Figure S1 shows a schematic of the typical flight, as well as the 15 flight tracks flown during SOCRATES.

To characterize in-and-below cloud precipitation properties, we leverage observations from both in situ probes and remote sensors. Table 1 gives a summary of the instruments we use in this study, along with a primary reference for each instrument. We describe how these in situ probe data are used in Section 2.2.

Table 1. Instruments

Instruments	Measurements	References
Cloud Droplet Probe (CDP)	Size and concentration of hydrometeors with a diameter between 2-50 μm	Lance et al. (2010) https://data.eol.ucar.edu/dataset/552.002
Two-Dimensional Stereo probe (2DS)	Size and concentration of hydrometeors with a diameter between 10-1280 μm	Wu and McFarquhar (2019) https://data.eol.ucar.edu/dataset/552.047
Ultra-High-Sensitivity Aerosol	Aerosols with dry diameters between 60 and 1,000 nm	DMT(2013); Sanchez et al. (2021) https://data.eol.ucar.edu/dataset/552.002

Spectrometer (UHSAS)		
HIAPER Cloud Radar (HCR)	Reflectivity, Doppler velocity, Spectral width, Signal to noise ratio, etc.	Vivekanandan et al. (2015) https://data.eol.ucar.edu/dataset/552.034
High Spectral Resolution Lidar (HSRL)	Backscatter coefficient, Particle Linear Depolarization Ratio, Extinction coefficient, etc.	Eloranta (2005) https://data.eol.ucar.edu/dataset/552.034

Note: For both CDP and 2DS, data is available at 1Hz temporal resolution. CDP data can be found in SOCRATES Navigation, State Parameter, and Microphysics Flight-Level Data. This study uses version 1.4 of this dataset. This study uses version 1.1 of the 2DS dataset. The radar and lidar moments data version 3.1 were processed by NCAR/EOL and 2 Hz (0.5 seconds) temporal resolution and 19 meters range vertical resolution. The operational specifications of HCR and HSRL is available at https://data.eol.ucar.edu/datafile/nph-get/552.034/readme_HCR_HSRL_SOCRATES_2Hz_v3.1.pdf.

Remote sensors include a 94-GHz W-band HIAPER Cloud Radar(HCR) (Vivekanandan et al., 2015) and a 532-nm High Spectral Resolution Lidar (HSRL) (Eloranta, 2005). Based on radar and lidar moments data, we will use retrieval techniques to derive precipitation properties, as detailed in section 2.3. HCR and HSRL were deployed in previous campaigns, such as CSET (e.g. Schwartz et al., 2019). The radar and lidar data were processed by NCAR/EOL at 2 Hz (0.5 seconds) temporal resolution and have 19 m vertical range resolution. A description of the NCAR/EOL data processing and corrections are given in readme files that are distributed with the data (with link in the acknowledgement). This includes a correction of radial velocity for platform motion following Romatschke et al. (2021), in which corrections are applied to the nadir and zenith pointing data separately. For nadir pointing data, radial velocity was corrected following Ellis et al. (2019), where for radial velocity of the surface (assumed to be 0 m/s) is used as a reference to correct the data with a running 3rd degree polynomial filter. A similar method is applied to the zenith pointing data, which are the focus of this paper. But for the zenith pointing data, instead of assuming zero velocity of surface, it is assumed that the cloud top velocities from zenith pointing times are similar to those of the neighboring nadir pointing times. Specifically, cloud top velocities are first calculated for both the nadir pointing data and zenith pointing data, then the difference of the two is used to correct the bias in the zenith pointing velocity data. Figure S2 shows an example of the zenith pointing velocity fields before and after the correction, and Figure S3 shows the averaged nadir pointing and zenith pointing velocity profiles from RF13, demonstrating that correction resulted in consistent velocity profile between nadir pointing data and zenith pointing times.

2.2 In situ Measurements

2.2.1 Droplet size distribution

This study uses in situ measurements mainly from two particle-sizing-instruments: a Cloud Droplet Probe (CDP) and a Two-Dimensional Stereo probe (2DS) as listed in Table 1. We focus on in situ measurement from these legs (as marked in Figure S1): below-cloud level legs, in-cloud level legs, and sawtooth legs (which are further divided into top-half of the cloud, bottom-half of the cloud, and the below-cloud portion as described below). These in situ measurements will be used to derive reflectivity to rain rate relationships (Z-R) relationships (section 4.1), to validate the precipitation retrievals (section 4.3), and to study in-and-below cloud precipitation properties (section 5).

We combine measurements from CDP and 2DS to create combined droplet size distribution (DSD) by using CDP measurements for bins with a diameter < 25μm and 2DS for bins > 50 μm. For drops in the intermediate size range (25–50 μm) we take the larger values of the two probes. After combining the DSD from two probes, we further averaged DSD for different regions and flight segments. Specifically, we examine the top half of the cloud layer from sawtooth legs; the bottom half of the cloud layer from sawtooth legs; the below-cloud portion of the sawtooth legs; the below-cloud level legs in 20s intervals; and in-cloud level legs in 10s intervals. For the purpose of averaging the in-situ data into these categories, the define the aircraft as in-cloud when then liquid water content greater than 0.03 g m^{-3} (Wood et al., 2011; Kang et al., 2021). Because of the limited sampling volumes of the probes, even with averaging, there can be gaps (and large variability) in the DSD distribution for large particles (where the concentrations are sufficient low that the probes become increasingly unlikely to observe these particles). As needed, we fill gaps in the DSD by fitting an exponential curve following Comstock et al. (2004) and extrapolate DSD for larger particles (out to a diameter of 2000 μm).

2.2.2 Precipitation properties

Precipitation properties are derived using the DSD. For different segments, we calculated rain rate (liquid water flux) as:

$$R = 3600 * \frac{\pi}{6}\rho_w \int_{D_{min}}^{\infty} n(D)\, D^3\, v_f(D) dD \qquad (1)$$

where ρ_w is the density of liquid water (1000 kg m^{-3}), D is the diameter in of m, 3600 is a scaling factor to convert the unit from kg m^{-2} s^{-1} to mm hr^{-1}, and $v_f(D)$ is the terminal fall velocity (unit of m s^{-1}) of droplets in the range from D to $D+dD$, and $n(D)$ is the drop size distribution (with units of m^{-3} mm^{-1}) . We use the terminal fall velocity model of Beard (1976) for $v_f(D)$ term. D_{min} is the lower limit for the integration, and except where stated otherwise is set to 40 μm. In Section 4.1, we test the importance of smaller droplets with diameter smaller than 40 μm on the liquid water flux(LWF_{total}).

Similarly, precipitation number (N_{precip}) is calculated as:

$$N_{precip} = \int_{D_{min}}^{\infty} n(D)dD \tag{2}$$

Precipitation liquid water content (LWC_{precip}) is calculated as:

$$LWC_{precip} = \frac{\pi}{6}\rho_w \int_{D_{min}}^{\infty} n(D)\, D^3 dD \tag{3}$$

Precipitation liquid water content weighted mean diameter (D_{precip}), which can be thought of as diameter at which half of LWC_{precip} is below and half is above, is calculated as:

$$D_{precip} = \frac{\int_{D_{min}}^{\infty} n(D)\, D^4 dD}{\int_{D_{min}}^{\infty} n(D)\, D^3 dD} \tag{4}$$

Precipitation liquid water content weighted width (σ_{precip}) is calculated as:

$$\sigma_{precip} = \sqrt{\frac{\int_{D_{min}}^{\infty} n(D)\, D^3 (D - D_{precip})^2 dD}{\int_{D_{min}}^{\infty} n(D)\, D^3 dD}} \tag{5}$$

2.2.3 Z-R relationships

To estimate the Z-R relationships from in situ measurements, we calculated radar reflectivity Z and rain rate R, respectively from the in situ droplet size distributions (DSD). Rain rate is calculated as equation 1. Reflectivity is proportional to the sixth moment of the DSD:

$$Z = \int_0^{\infty} n(D)\, D^6\, \gamma_f(D) dD \tag{6}$$

where $n(D)\ dD$ gives number concentrations from diameter D to $D+dD$, $\gamma_f(D)$ is the Mie-to-Rayleigh backscatter ratio (shown in Figure S4, which is the ratio of the backscatter efficiency of Mie scattering for W-band (94-GHz), calculated using the miepython package based on Wiscombe

(1979), and backscatter efficiency of Rayleigh scattering (Bohren & Huffman, 1983). With calculated reflectivity and rain rate from the in situ DSD, the Z-R relationship assumes a traditional power-law of the form:

$$Z = aR^b \tag{7}$$

Where a and b are coefficients, and Z is the independent variable. Equation 7 can also be rearranged as $R = (Z/a)^{1/b}$, which can be used to derive R based on Z observations. Coefficients a and b can be estimated using the least-squares regression in log space following Comstock et al. (2004):

$$logR = \frac{1}{b}\left(-\,log\ a\ +\ log\ Z\right) \tag{8}$$

We estimated the uncertainty in estimated exponents b and intercepts a that are based on in situ data using bootstrapping. Note that in section 4.1, we also estimated Z-R relationship based on radar observed reflectivity factor and rain rate from radar-lidar retrieval (more details in section 2.3.3), where we use moving blocks bootstrapping method following Wilks (1997) to estimate uncertainty in a and b coefficients, with a block length that close to the enfolding length.

2.3 Precipitation Retrievals based on remote sensors

Precipitation retrievals described in this section use the zenith-pointing data collected when the aircraft was flying level-legs below the cloud. To illustrate, Figure 1a shows the flight track altitude and measured radar reflectivity for research flight 13 (RF13). In panel (a), the potions of the flight track which feature below-cloud-level legs are colored green. Figure 1b-f shows the radar and lidar data in more detail, for the below-cloud level leg starting from 03:40 UTC, which is marked by the grey shading in Figure 1a. In general, retrievals undertaken for below-cloud level legs have the advantage that the zenith pointing lidar data allows one to determine the position of cloud base, as well as providing measurements of the backscatter (Figure 1c) and depolarization ratio (Figure 1d) of the precipitation that has fallen from the cloud and can be used to determine the precipitation phase. We describe the retrieval process in the three subsections that follow: (1) determine the cloud boundaries; (2) determine the phase of precipitation; (3) determine the liquid precipitation microphysical properties (such as the rain rate).

2.3.1 Determine the cloud boundaries

To determine the cloud base, we use the lidar backscatter coefficient β (e.g. Figure 1c) and define the cloud base as the altitude where β first exceeds a threshold of 0.0001 m^{-1} sr^{-1}. The black dots in Figure 1c show the cloud base identified using this threshold. Cloud top for our analysis is based on the radar reflectivity data, which has already been masked for significant detections (above the instrument noise floor). The cloud top is taken simply as the maximum height with a valid reflectivity echo below 3km, as marked by grey dots in Figure 1b-f.

2.3.2 Determine the phase of precipitation below cloud base

With the cloud boundaries identified, the next step is to determine the phase of the precipitation falling from the clouds. Following Mace and Protat (2018), we determine the precipitation phase using the lidar particle linear depolarization ratio (PLDR) (e.g., Figure 1d). The basic concept is that the lidar emits linearly polarized light, and scattering by spherical particles (e.g. liquid drops) does not change the polarization state of the light and thus generates little PLDR, while scattering from non-spherical particles (e.g. ice particles) creates significant depolarization and thus generates measurable increase in PLDR. In this study, for each lidar column, we examined the median of the PLDR over the vertical interval between cloud base to the first useable lidar range gate. For clouds with a cloud top temperature greater than 0, that is for warm clouds whose precipitation must be liquid, we find the below-cloud base PLDR values to be less than 0.03 about 90% of the time, and to be above 0.05 less than 1% of the time(see Figure S5 for overall statistics and Figure S6 for an example case). Thus, for cooler cold-topped clouds (which might precipitate ice), we define the precipitation to be liquid phase when the median PLDR < 0.03; ice precipitation when PLDR > 0.05; and ambiguous phase with PLDR values in between.

2.3.3 Liquid Precipitation retrieval

After determining the cloud base and precipitation phase, we can use a hierarchy of retrieval methods with increasing complexity to derive the precipitation microphysical properties, starting from (1) a simple Z-R relationship approach where only one variable, the radar reflectivity, Z, is available to derive the rain rate, to (2) a ZV retrieval following Mace et al. (2002) and Marchand et al. (2007), where radar reflectivity, Z, and mean Doppler velocity, V, are known to (3) a radar-lidar retrieval following O'Connor et al. (2005) based on three observables: radar reflectivity Z, radar Doppler spectral width σ_d, and lidar backscatter β. We briefly describe the radar-lidar and then the ZV and in this section, and present retrieval results and evaluate the retrievals using in situ observations in Section 4.

The radar-lidar retrieval technique uses three input variables radar reflectivity, Z (Figure 1b), doppler spectral width, σ_d (Figure 1e), and lidar backscatter, β (Figure 1c), to solve for three parameters in an assumed modified gamma distribution (equation 9) for the precipitation drop size distribution. The three parameter are the shape factor μ, the median equivolumetric diameter D_0, and the normalized droplet concentration N_w:

$$n(D) = N_w f(\mu)(\frac{D}{D_0})^{\mu} e^{[\frac{-(3.67+\mu)D}{D_0}]} \tag{9}$$

where D is diameter, and $f(\mu)$ is a function of μ

$$f(\mu) = \frac{6}{3.67^4}\frac{(3.67+\mu)^4}{\Gamma(\mu+4)} \tag{10}$$

where Γ is the gamma function. Integration of the droplet size distribution in (9) will yield the precipitation droplet number concentration, N_{precip}, as in equation 2.

Following O'Connor et al. (2005), one can show that for a fixed value of the shape factor, μ, the ratio of the radar reflectivity to lidar backscatter is proportional to the fourth power of the mean drop size, and the combination of radar reflectivity and lidar backscatter can therefore be used to calculate D_0 and N_w. In the retrieval algorithm, this is done assuming an initial value of $\mu = 0$.

The Doppler spectral width is then forward calculated and μ is increased or decreased in order to match the observed Doppler spectral width (after applying corrections for beam width and turbulent motions). The forward calculations require a model for the hydrometeor terminal fall velocity, for which we use the model of Beard (1976). Once the three distribution parameters are known, it is straightforward to calculate the rain rate, rain liquid water content, and mean rain drop size, etc. using the fall velocity and equation (9). This retrieval technique has been widely used in retrieving drizzle properties (e.g. Ghate & Cadeddu, 2019; Yang et al., 2018), including the CSET campaign with airborne radar and lidar (Schwartz et al., 2019; Sarkar et al., 2021). Our implementation largely follows O'Connor et al. (2005), except for estimation of the contribution from air turbulence to the observed spectral width. Instead of using the horizontal wind speed to estimate the length scale (we note O'Connor et al. (2005) originally developed the retrieval for vertically pointing ground-based radar and lidar), we use the aircraft speed.

In addition to the radar-lidar retrieval technique, we also use a reflectivity-velocity (ZV) retrieval technique (Frisch et al.,1995; Mace et al., 2002; Marchand et al.,2007). The first step in this retrieval is to estimate the precipitation fall velocity from radar measured Doppler velocity, which includes the effect of vertical air motions (i.e., updrafts/drowndraft). We do this follow Orr and Kropfli (1998) and partition the measured Doppler velocities into a set of height and reflectivity bins (for each below-cloud zenith-pointing segment) and average the partitioned Doppler velocity as an estimate for the fall velocity (as a function of height and radar reflectivity). The underlying idea is that at a given altitude and reflectivity, there is a characteristic size distribution (with a characteristic fall velocity) and by averaging the Doppler velocities over a narrow range of reflectivity values, one averages out the effect of the updrafts and downdrafts leaving only the mean fall velocity. In this study we use reflectivity bins are that 2 dBZ wide, and use 200 m vertical bins with 100 m overlap. The results are not particularly sensitive to these choices, as long as there is a healthy number of samples are available in each bin. Following Frisch et al. (1995), it is straight-forward to obtain analytical expressions for distribution parameters D_0 and N_w given the derived fall velocity, measured reflectivity, and an assumed shape factor μ. Except were stated otherwise, we assume shape factor to be 0. One can show that the modified gamma distribution (equation 9) reduces to the exponential distribution when the shape factor is zero. In the radar-lidar retrieval we find retrieved shape factor is often quite small and we will examine and discuss the sensitivity of the ZV retrieval to assumed shape factor values in Section 4.2.

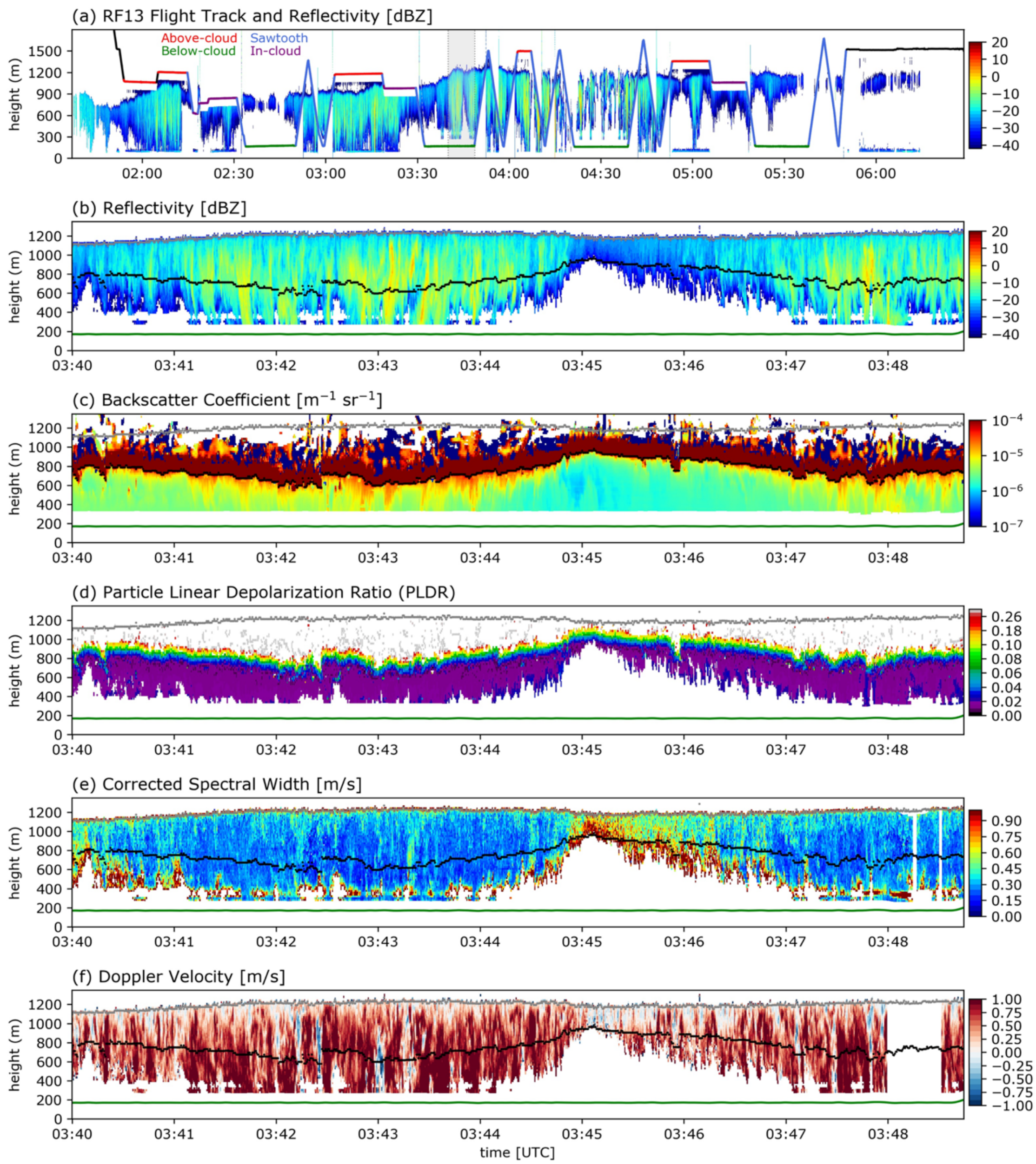

Figure 1. Example radar and lidar data collected during the SOCRATES. Panel a shows the flight tracks and reflectivity fields from research flight 13 (RF13), with different segments color-coded as in Figure S1. The grey shading marks a portion of one below-cloud level leg, and a zoom-in view of the radar and lidar fields for this segment are shown in panels b-f: (b) radar reflectivity; (c) lidar backscatter coefficient; (d) lidar particle linear depolarization ratio; (e) radar spectral width; (f) radar doppler velocity. The grey lines show the estimated cloud top, the black lines show the estimated cloud base, and the green line shows the location of the aircraft.

3 Campaign overview

To get a general sense of the hydrometers (clouds and precipitation) sampled by the airborne W-band radar during the SOCRATES, Figure 2a shows the joint histogram of radar reflectivity with height observed during below-cloud, zenith-pointing periods (i.e. as illustrated in Figure S1). Here the histogram is normalized by the number of radar columns, such that the value in each bin indicates how often hydrometers (cloud and precipitation) have a reflectivity (with +/- 1 dBZ of the given value) in the given altitude/height range; and the sum at each height (row) will gives the hydrometer fraction (Figure 2b).

Note that there is no data to the left of the red line in panel a. This is because of limited radar sensitivity, and as distance increases, the minimum detectable reflectivity value increases. Likewse, there are no data from 0 to 200 meters altitude because the aircraft lowest legs were typically flown at around 100-150 m altitude, and the radar blanking interrupt (the region corresponding to the time when the radar outgoing pulse is being, or has just been, transmitted and the radar system has not yet begun measuring the return power) typically extends about 203 m above this (Schwartz et al., 2019).

The maximum frequency of hydrometers observed by the radar occurred between 700 and 1200 meters, with a hydrometer fraction over 50%. (Note this is not projected area or the fraction of radar columns with a significant echo at any altitude, that value is near 90%). Reflectivity factors larger than -10 dBZ are relatively rare and there is no distinct mode associated with precipitation (that is, no peak with a reflectivity larger than about -20 dBZ). Reflectivity factors larger than -10 dBZ are common of the Southern Ocean (see for example Mace and Protat 2018), but such factors are associated with fronts or convection (including the shallow convection sometimes associated with vigorous open cells) and not typical of the shallow (cloud tops < 2 km) and largely overcast stratocumulus sampled during SOCRATES. Rather there is a single mode or continuum of reflectivity that span reflectivity factors from about -40 dBZ (where there are few if any precipitation sized particles) to values around -10 dBZ (where precipitation is still light with rain rate <1 mm hr^{-1} but can have a substantial impact on cloud condensation nuclei and cloud lifetime, Kang et al.,2022) and a peak below -20 dBZ. Most of this cloud is supercooled. Overall, we find that about 80% of the stratocumulus sampled during SOCRATES had a cloud top temperature < 0°C and cloud depth < 600m (figure not shown), and about 62% of the stratocumulus were precipitating, defined as 3 consecutive radar bins (about 60 meters) below cloud base with a reflectivity greater than -40dBZ. The occurrence of precipitation drops to 34% if a reflectivity threshold of -20 dBZ is applied (in spite of the detections being below cloud base), indicative of very light nature of the precipitation.

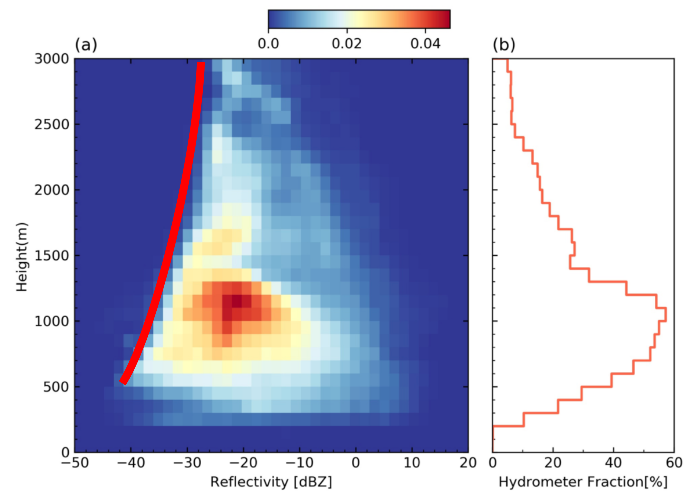

Figure 2. (a) Joint histogram of hydrometer (cloud & precipitation) radar reflectivity with height observed by the airborne W-band radar during below-cloud, zenith-pointing periods (i.e., when aircraft is flying below the cloud, as illustrated in Figure S1). Histogram is normalized by total number of radar "columns" such that the histogram values is the fractional occurrence (see text). (b) hydrometer fraction [%] at each height of all radar "columns". The red line on panel a shows the minimum detectable reflectivity values by HCR as a function of height.

What is the phase of the precipitation sampled during the SOCRATES? As described in Section 2.3.2, we determine the precipitation phase using the lidar particle linear depolarization ratio PLDR (Figure 1d), and interpret the precipitation as liquid phase when PLDR < 0.03; ice phase when PLDR > 0.05; and ambiguous for PLDR values in between. Figure 3a shows that around 60% of the precipitation from the zenith-pointing segments are liquid phase and about 20% of the precipitation are ice phase, with the remaining 20% being ambiguous phase. How does precipitation phase relate to the cloud top temperature? Figure 3b shows the relative occurrence of precipitation in difference phases as a function of cloud top temperature (CTT). For the warm-topped clouds (CTT > 0°C), we expect that all the precipitation should be liquid phase. Temperature is not used in the phase retrieval, and consistent with the discussion in Section 2, the low occurrence of ambiguous or ice phase precipitation with CTT > 0°C is indicative of the low retrieval error. For the cold-topped clouds (CTT <0°C), liquid precipitations still dominate for clouds with CTT between 0 and -10°C, with the ice fraction increasing as temperature decreases. But it is not until about a CTT of -15°C that ice phase appears to dominate. It could be that the apparent peak in ice phase occurrence near -15°C is a result of dendric growth (or secondary ice product associated with dendrites), as dendric growth is known to occur near this temperature (e.g., von Terzi et al., 2022) but there is too little data here to be confident this uptick in ice phase is statistically significant.

An interesting question related to phase is whether or not precipitation phase is related to radar reflectivity. Zhang et al. (2017) have shown that lidar depolarization ratios is correlated with radar reflectivity, and for the SO in particular, Mace and Protat (2018) show that W-band radar reflectivity greater than -10 dBZ is associated with ice-phase hydrometeors (based on CAPRICORN observations). Figure 3c shows the occurrence of the different precipitation phase for cold-topped clouds as a function of reflectivity. Overall, it shows that reflectivity factors less than about -10 dBZ are predominately liquid, while reflectivity factors greater than 0 dBZ is predominately ice. We will discuss this result in more detail in the conclusions.

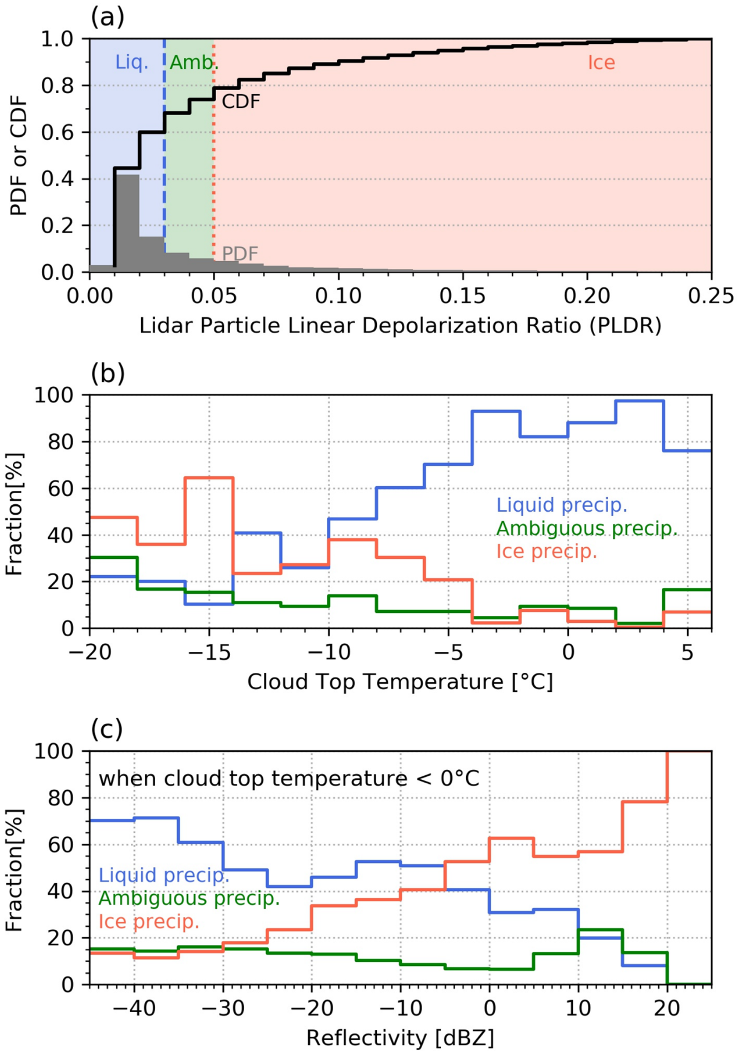

Figure 3. (a) Probability and cumulative density functions for lidar particle linear depolarization ratio (PLDR) for below-cloud precipitation (b) The fraction of liquid, ice, and ambiguous precipitation as a function of cloud top temperature. (c) The fraction of liquid, ice, and ambiguous precipitation as a function of radar reflectivity. To distinguish different precipitation type, liquid precipitation is marked as blue, ice precipitation is marked as red, and ambiguous precipitation is marked as green.

4 Precipitation Retrievals

In this section, we will explore a hierarchy of retrieval methods based on complexity, from (1) the simplest Z-R relationship approach where only one variable reflectivity Z is known, to (2) a ZV retrieval using two variables (reflectivity Z and Doppler velocity V), to (3) a radar-lidar retrievals based on three variables (reflectivity radar reflectivity Z, doppler spectral width σ_d, and lidar backscatter β). In section 4.1, we will develop Z-R relationships based on in situ data. In section 4.2, we will demonstrate the results from ZV and radar-lidar liquid precipitation retrievals using a case example, and in section 4.3, we evaluate these retrievals using in-situ aircraft observations from all the segments where retrievals were performed.

4.1 Reflectivity to rain rate (Z-R) relationships

One objective of this study is to estimate Z-R relationships of the form $\mathrm{Z} = \mathrm{a}R^{b}$. Z-R relationships are useful and convenient, requiring only one independent variable (reflectivity *Z*) to estimate rain rate *R*. Such relationships have a long history in atmospheric science, and as concerns stratocumulus in particular, relationships have been derived in past studies for stratocumulus over the Eastern Pacific (Comstock et al., 2004), over the north-east Atlantic and in U.K. coastal waters (Wood, 2005), and for nocturnal stratocumulus clouds off the California Coast (VanZanten et al., 2005). More recently, Protat et al. (2019b) estimated Z-R relationships at the surface over the global ocean, including the Southern Ocean, based on surface disdrometer measurements. In this section, we will derive Z-R relationships using SOCRATES aircraft observations following the method presented in Section 2.2.3 and compare our results with previous studies.

Figure 4 shows the Z-R relationships derived using in situ data taken at different locations relative to the cloud layer and surface (see Figure S1 for a schematic). Table 2 lists the corresponding a and b coefficients. In Figure 4a, we only consider droplets with a diameter larger than 40 μm following Comstock et al. (2004), while in Figure 4b, we include all droplets including those droplets with a diameter smaller than 40 μm. We will focus on Figure 4a first. Figure 4a shows that estimated Z-R relationships do have a vertical dependence. The intercept controlled by coefficient *a* increases as one moves from the cloud layer to the surface, while the slope controlled by exponent *b* remains largely unchanged. The vertical dependence of Z-R was also noticed in previous studies (e.g. Comstock et al., 2004; vanZanten et al., 2005). The exponent *b* estimated in Figure 4a ranges from 1.3 to 1.45, with a (one sigma) uncertainty that ranges from 0.5 to about 0.1, based on a bootstrap resampling technique (uncertainties are listed in Table 2). Note the uncertainties in the *a* and *b* coefficients are not independent, but rather are positively correlated such that a larger estimate for the a-value is associated with a larger estimate for the b-values. Table 2 also lists some Z-R relationships estimated from other studies mentioned above. Overall, we find the exponent *b* to be similar to that from Comstock et al. (2004), vanZanten et al. (2005), and many other earlier studies summarized in Rosenfeld and Ulbrich (2003) over other regions and other cloud types. Later in this section we will compare the rain rate derived from Z-R relationships with rain rate derived from two other retrieval methods.

The above analysis is based on the idea that only droplets larger than 40 μm are considered precipitation. But droplets smaller than 40 μm can and do contribute to the flux of liquid water (Nicholls, 1984). What happens if small droplets with a diameter smaller than 40 μm are included when calculating Z and R from in situ DSDs? The results are shown in Figure 4b. Comparing Figure 4a and 4b, one can see that the estimated Z-R relationships is very sensitive to whether one excludes smaller drops, especially for the data collected in the cloud. Differences in the estimated Z-R are less dramatic when using in situ data outside of the cloud (i.e. below-cloud portion of the sawtooth leg and below-cloud level legs).

To explore the importance of the smaller droplets, Figure 5a shows an example of DSDs measured near the top of a cloud, near the bottom cloud and below cloud during one sawtooth leg, as well as a nearby below-cloud level leg (depicted in the bottom panel). The associated liquid water flux distribution $D^3N(D)V(D)$ is shown Figure 5b, and the reflectivity distribution $D^6N(D)$ in Figure 5c. Note as in the microphysical retrievals, here we use the terminal fall velocity model of Beard (1976) for V(D). Below-cloud, small droplets evaporate much more quickly than larger droplets, and most of the contributions to the liquid water flux comes from larger droplets, such that the effect of small droplets on liquid water flux and reflectivity can be largely neglected. We hasten to add, however, this is true not true for the total number concentration (Figure 5a); where small droplets remain more numerous (than droplets above 40 μm), and includes many particles with sizes smaller than 5 μm, which one might consider haze-particles or hydrated-aerosols rather than cloud droplets. Within the cloud layer, small droplets make a large contribution to the liquid water flux and contribute slightly to the reflectivity. Droplets in the diameter range of 10-40 μm contribute 78% of the liquid water flux in the top half of the cloud, and still comprise about half of the water flux in the bottom half of the cloud. Contributions to the reflectivity from droplets in the range of 10-40 μm are smaller than those of larger droplets, but both make a non-trivial contribution.

In short, as Figure 5 and the differences in estimated Z-R in Figure 4a and Figure 4b highlight, the sedimentation of small droplets is (or can be) a significant component of the total liquid water flux in cloud and applying the Z-R relationship derived from only larger particles or from below-cloud measurements effectively ignores the contribution from small particles (and below-cloud Z-R equations should be applied with caution to in-cloud reflectivity measurements and should be expected to underestimate the total liquid water flux).

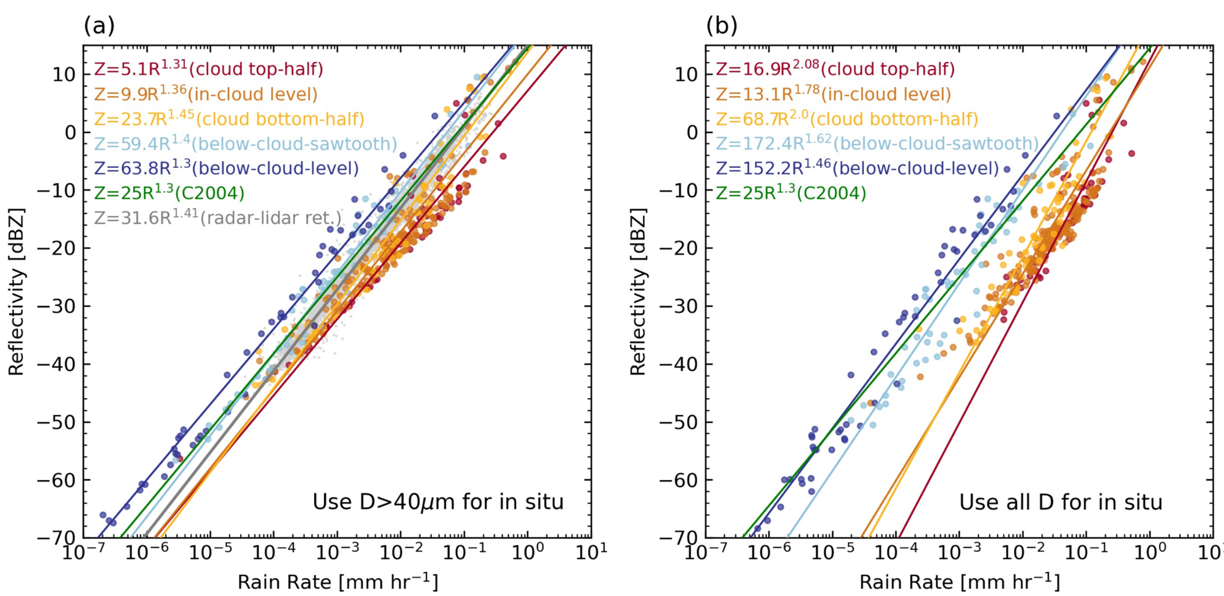

Figure 4. Z-R relationship derived using in situ data and retrievals. Diameter >40um cutoff for the in situ measurements is imposed in panel a, while panel b does not apply any cutoff, and considers all droplet sizes for in situ data.

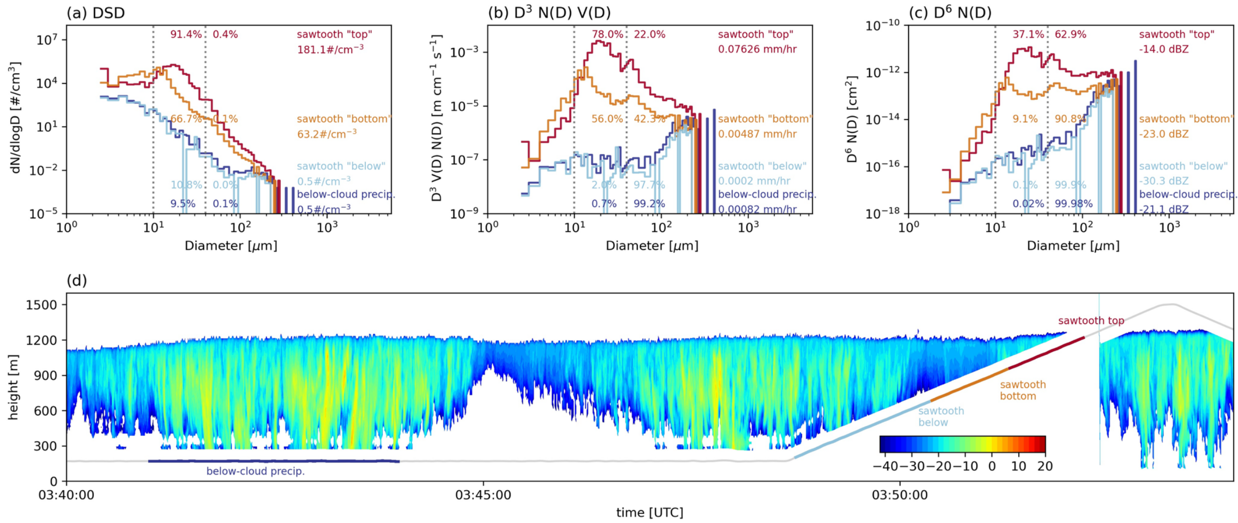

Figure 5. Example case to show the contributions of droplets in different size ranges with in situ measurements taken from different segments: (a) average droplet size distribution; (b) product of diameter cubed, droplet size distribution and terminal fall velocity;(c) product of diameter to the power of six and droplet size distribution; (d) reflectivity field and flight track for this example, the color-coded lines marked the locations of different segments showing in panel a-c. The vertical dashed line in panels a-c is the reference line for 10 μm and 40 μm. The percentage on panel a, b, and c show the contributions from different size range to droplet number concentration, to rain rate, and to reflectivity, respectively.

Table 2. Z-R relationship of the form $Z = aR^b$

Equation	Location	Remarks	Reference
$Z = (5.1 \pm 3.5)\, R^{(1.31 \pm 0.1)}$ $[Z = (16.9 \pm 26.1)\, R^{(2.08 \pm 0.25)}]$	the top half of the cloud layer from the sawtooth leg	Estimated using SOCRATES aircraft in situ measurements with and without the 40µm cutoff, [without given in brackets]	This study
$Z = (9.9 \pm 2.8)\, R^{(1.36 \pm 0.05)}$ $[Z = (13.1 \pm 6.8)\, R^{(1.78 \pm 0.11)}]$	in-cloud level legs		
$Z = (23.7 \pm 11.6)\, R^{(1.45 \pm 0.08)}$ $[Z = (68.7 \pm 68.5)\, R^{(2.0 \pm 0.16)}]$	bottom half of the cloud layer from the sawtooth leg		
$Z = (59.4 \pm 21.4)\, R^{(1.4 \pm 0.04)}$ $[Z = (172.4 \pm 106.7)\, R^{(1.62 \pm 0.06)}]$	the below-cloud portion of the sawtooth leg		
$Z = (63.8 \pm 47.1)\, R^{(1.3 \pm 0.05)}$ $[Z = (152.2 \pm 277.9)\, R^{(1.46 \pm 0.09)}]$	below-cloud level legs.		
$Z = (31.6 \pm 1.4)\, R^{(1.41 \pm 0.007)}$	Cloud base	Estimated using SOCRATES W-band radar measured reflectivity and radar-lidar retrieved rain rate just-below cloud base	
$Z = 25R^{1.3}$	Cloud base	Estimated for stratocumulus over Eastern Pacific	Comstock et al. (2004)
$Z = 12.92\, R^{1.47}$	Cloud base	Estimated using aircraft in situ DSD measurements for nocturnal stratocumulus clouds over California Coast	vanZanten et al. (2005)
$Z = 12.5\, R^{1.18}$	All in-cloud levels	Estimated using aircraft in situ DSD measurements for stratocumulus over the north-east Atlantic and in U.K. coastal waters	Wood (2005)

Note: here uncertainty is estimated using either by bootstrapping (rows 1-5) or moving block bootstrapping (row 6) with the one-sigma uncertainty given after the plus-minus sign. For the Z-R relationship that is estimated using in situ measurements, the Z-R relationship estimated using only larger *droplets, with a diameter greater than 40μm, is listed first, followed by the Z-R relationship estimated using all droplets included those droplets with a diameter smaller than 40 μm. For the equations above, the reflectivity Z is in the unit of mm^6mm^{-3}, and the rain rate is in the unit of mm hr^{-1}. For the equations in the past studies with the form of $R = cZ^d$ or have different units, we rearranged the equation and converted the units to keep the consistency and make it easier to compare. Unless noted, the default band for reflectivity is W-band.*

4.2 ZV retrieval and radar-lidar retrieval

In this subsection, we examine both the ZV retrieval and radar-lidar retrievals using the zenith-pointing remote sensing data collected when the aircraft was flying level-legs below the cloud. We will begin with one case study, compare results from different retrieval methods, and then examine the sensitivity of ZV retrieval results to the assumed shape factor μ. The overall retrieval performance will be evaluated in Section 4.3.

Applying the ZV retrieval (described in Section 2.3.3) to the example presented in Figure 1, the parameters D_0 and N_{precip} can be derived from measured reflectivity Z, assumed shape factor μ, and derived terminal fall velocity. Figure 6a shows the reflectivity-weighted terminal fall velocity, v_t , derived following Orr and Kropfli (1998). Here we see generally larger v_t toward the bottom of the cloud, and in precipitation shafts (regions of relatively high reflectivity extending below cloud base). Figure 6b and 6c shows derived median equivolumetric diameter D_0, and precipitation concentration N_{precip}, assuming μ =0. Not surprisingly, Figure 6b shows that D_0 is larger where v_t is larger, and is about 100-200 μm below cloud base. Figure 6c shows N_{precip} below cloud base is in the order of 10^3~10^5 m^{-3}.

Applying the radar-lidar retrieval technique to the example presented in Figure 1, with three input variables (radar reflectivity Z, doppler spectral with σ_d, and backscatter coefficient β), we can also solve for shape factor μ , median equivolumetric diameter D_0, and precipitation number concentration N_{precip}, as shown in Figure 7. The shape factor μ describes the shape of the DSD (equation 9) and larger μ implies narrower distributions. As in O'Connor et al. (2005), we find large areas with broad DSDs (small μ). Narrow DSDs implied by large μ are typically found underneath the thicker portion of the clouds (and as we will see later have larger rain rates). The median equivolumetric diameter D_0 is mostly between 50-250 μm, with larger sizes occurring where μ is larger. Again, this is similar to what O'Connor et al. (2005) observed and appears to be quite typical for drizzling stratocumulus. Comparing the two retrieval methods, both D_0 and N_{precip} from ZV retrieval (Figure 6) tend to be more spatially homogeneous below cloud base than that from radar-lidar retrieval (Figure 7), and the D_0 from ZV retrieval tends to be smaller than that from radar-lidar retrieval in the precipitation shafts (where the assumption of a small value for the shape factor appears problematic, more on this below).

Once the parameters that determine the DSDs are derived, it is straightforward to calculate other precipitatition properties such as rain rate. Figure 8b and c show the ZV retrieved the rain rate (assuming μ =0) and radar-lidar retrieval retrieved the rain rate. Overall, the two retrieval methods give similar results (mean of rain rate from ZV retrieval is 0.0096 mm hr^{-1}, and mean of rain rate from radar-lidar retrieval is 0.0093 mm hr^{-1}). With derived Z-R relationships from section 4.1, one can also derive rain rate by apply them to the radar reflectivity fields, as shown in Figure 8a, with derived rain rate by applying Z-R relationships shown in Figure 4a from sawtooth-top to the top half of the cloud, from sawtooth-bottom to the bottom half of the cloud; as well as sawtooth-below to area below the cloud base. Overall, the retrieved rain rate has a magnitude that is around 0.001-0.1 mm hr^{-1}. The discontinuity in the rain rate fields in Figure 8a is because three different Z-R relationships are applied to different regions. The difference in Z-R relationships (i.e. with or without D>40 μm cutoff) also results in differences in derived rain rate (Figure S7), especially for the in-cloud portion. Overall, regardless of the retrieval approaches, it can also be seen that higher rain rates tend to occur below the geometrically thicker portion of the clouds, and we will explore the scaling between rain rate and cloud depth further in Section 6.

In Figures 6 and Figure 8b, we assume μ =0 in the ZV retrieval, while retrieved μ from radar-lidar retrieval clearly shows spatial variations (Figure 7a). How will ZV retrieved D_0, N_{precip}, and rain rate vary with assumed μ? Figure S8 shows that the derived D_0 increases with increasing μ values such that mean D_0 just below cloud base is 102 μm when $\mu = 0$, and is 156 μm when $\mu = 10$. In contrast, as shown in Figure S9, the derived N_{precip} decreases significantly with increasing μ values, with mean N_{precip} at cloud base is about 1.2×10^5 m^{-3} when $\mu = 0$, and is 1.2×10^3 m^{-3} when $\mu = 10$. However the derived rain rate (Figure S10) shows relatively little dependence on assumed μ, with rain rate at cloud base decrease slightly from about 0.009 mm hr^{-1} ($\mu = 0$) to about 0.007 mm hr^{-1} ($\mu = 10$). The small sensitivity in rain rate ultimately arises because the liquid water flux is to first order given by the velocity (which is input to the retrieval) times the liquid water content (which is strongly constrained by the reflectivity that is likewise input to the retrieval).

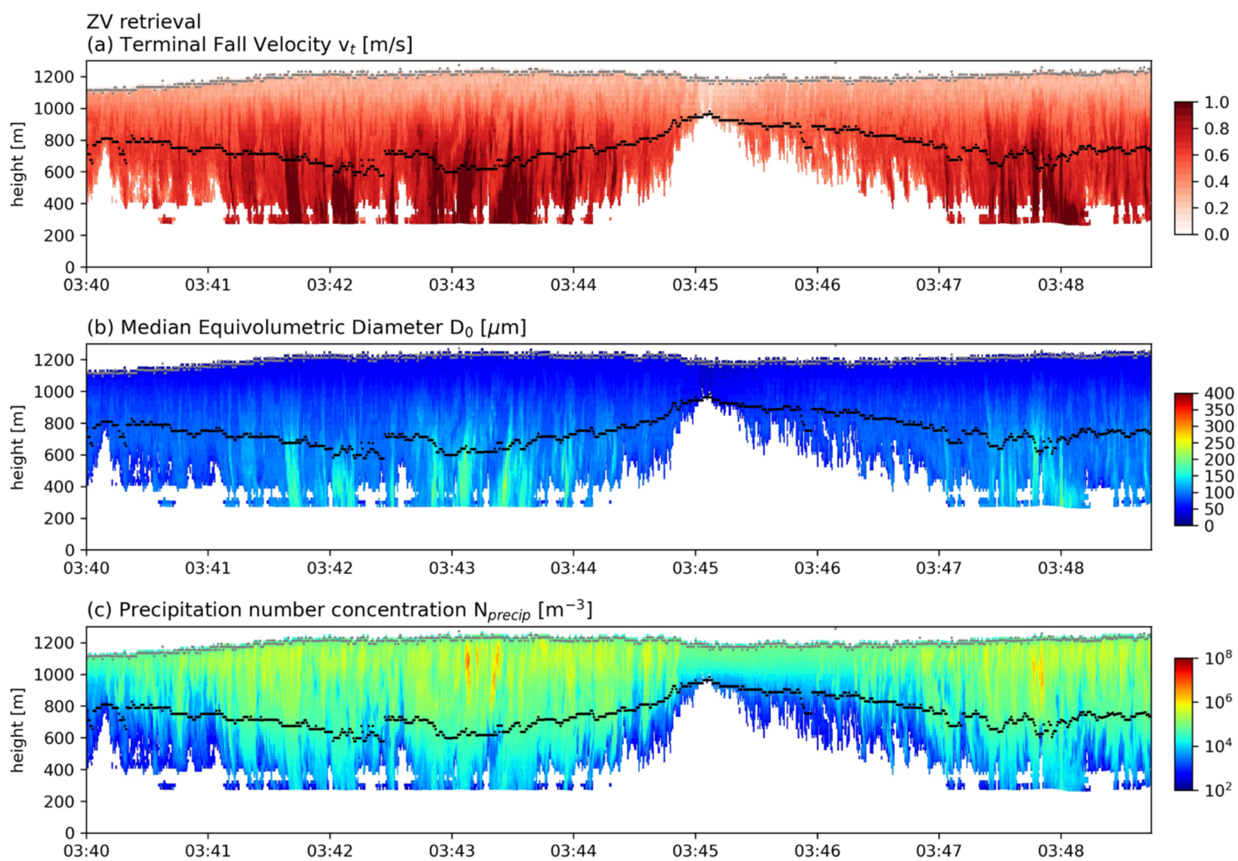

Figure 6. A time-height plot of ZV method retrieved drizzle properties assuming shape factor for the example segment is shown in Figure 1. (a) reflectivity-weighted the terminal fall velocity

v_t; (b) median equivolumetric diameter D_0, and (c) precipitation number concentration N_{precip}. The grey lines show the estimated cloud top, the black lines show the estimated cloud base.

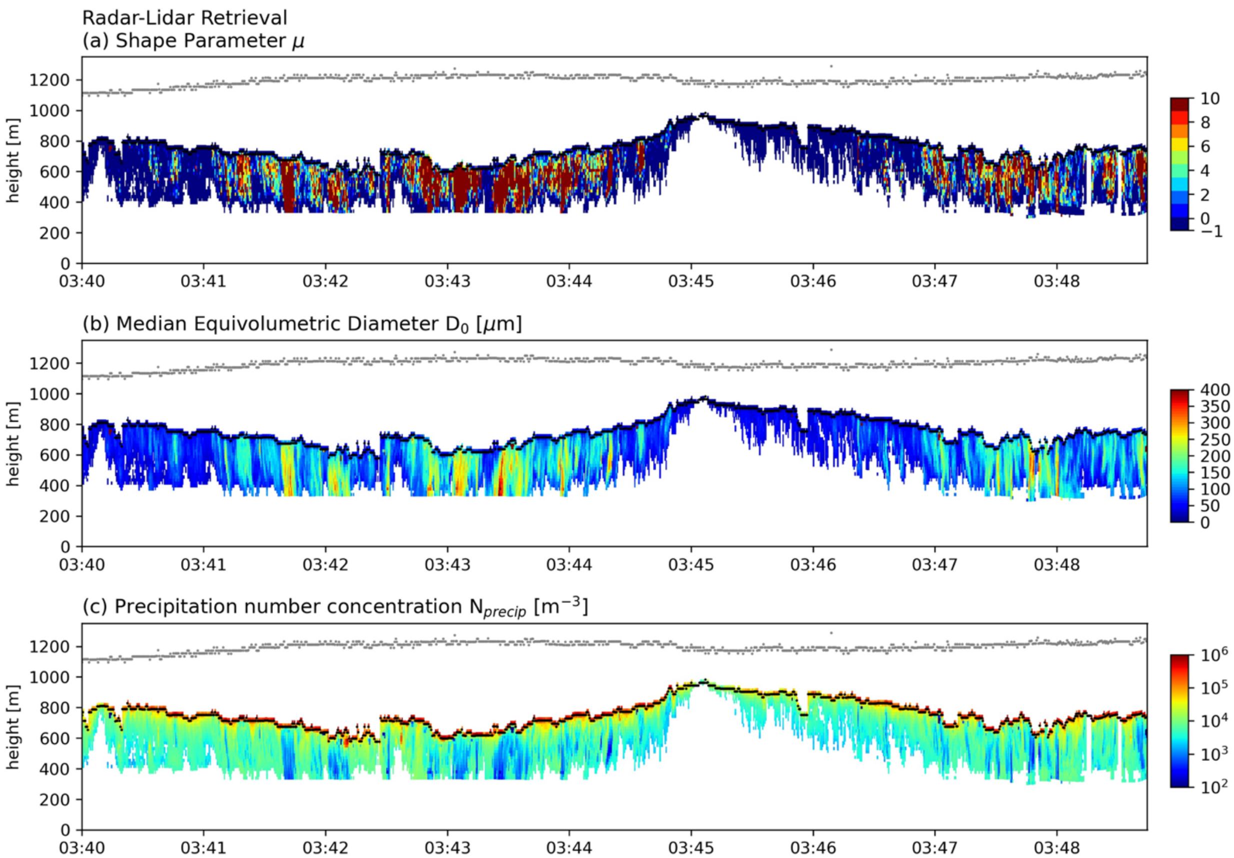

Figure 7. A time-height plot of radar-lidar retrieved drizzle properties for the example segment is shown in Figure 1. Radar-lidar retrieval method derived parameters for modified gamma distribution (a) shape factor μ; (b) median equivolumetric diameter D_0, and (c) precipitation number concentration N_{precip}. The grey lines show the estimated cloud top, the black lines show the estimated cloud base.

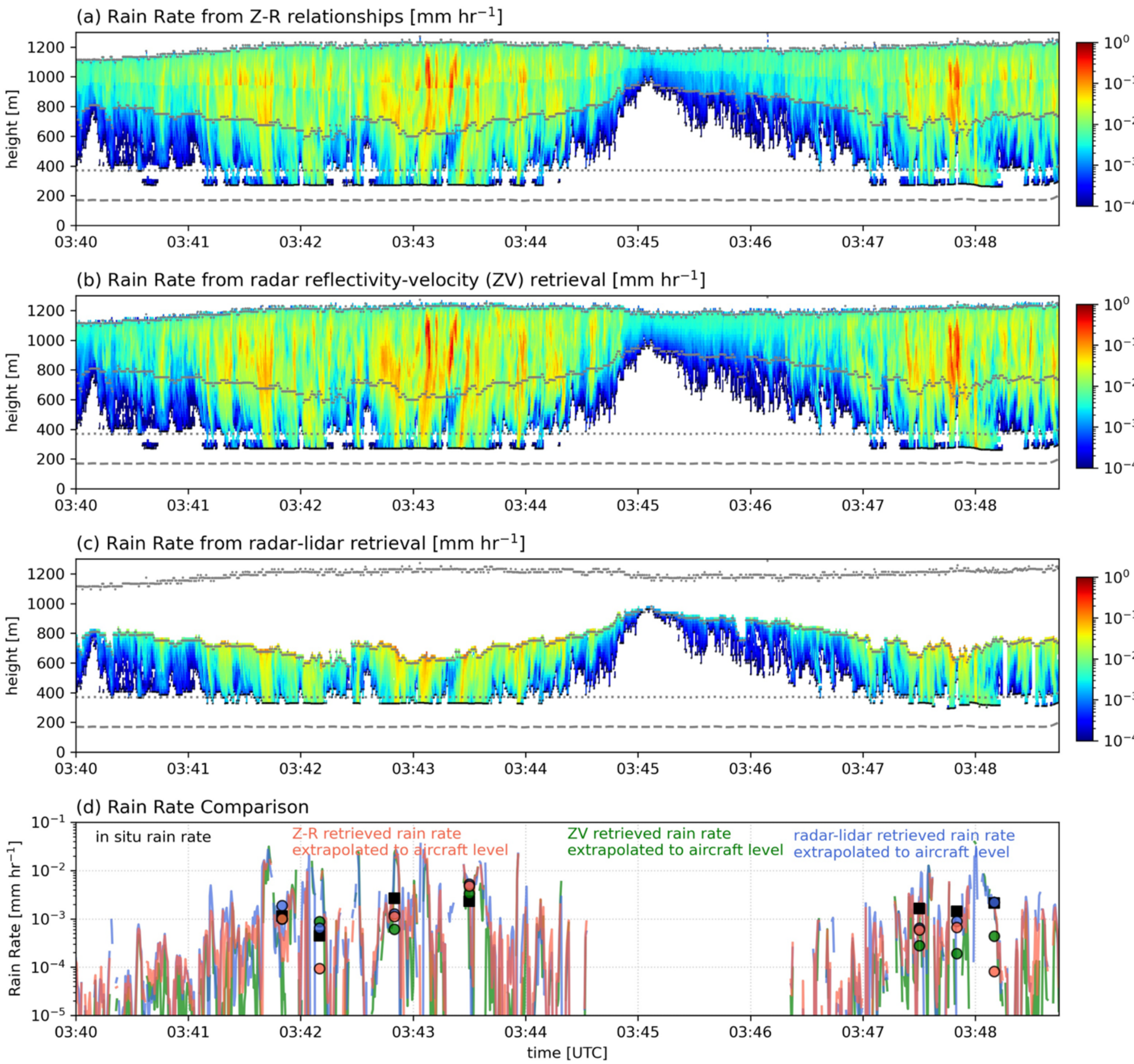

Figure 8. Retrieved rain rate for example case using (a) Z-R relationships (D > 40μm), (b) ZV retrieval technique, and (c) radar-lidar retrieval technique, and (d) their comparisons with in situ estimates. In panels a-c, the dashed grey line shows the location of the aircraft, while the dotted line is a reference line to show 200 meters above the aircraft's location. In panel d the retrieved rain rates were extrapolated to the aircraft level to compare with the in situ data. The pink line shows the rain rate retrieved with Z-R relationships, the green line shows the rain rate retrieved with the ZV retrieval technique, and blue line shows the rain rate retrieved with the radar-lidar retrieval technique. The black squares represent the rain rate estimated with in situ measurements, where rain rates are derived from averaged droplet size distribution (merged CDP and 2DS) over 20 seconds. Over that same time window, the median value of the retrieved rain rate time series was taken, denoted as pink dots (Z-R relationship), green dots (ZV retrieval) and blue dots (radar-lidar retrieval).

4.3 Retrieval validation

How good are the rain rate retrievals? One would think a simple comparison between the retrieved rain rate with in situ measurements from the aircraft could answer this question. But there are a few challenges that need to be overcome.

The first challenge is that retrieved rain rates that are closest to the aircraft level marked as a dashed line around 200 m in Figure 8) are still at least 150 meters away, making it difficult to make a direct comparison. This is because there is a blanking interrupt, a brief period where one needs to wait for the outgoing pulse to exit the radar (or lidar) system and for the effect of strong scattering from nearby objects (clutter) to dissipate. To overcome this difficulty, we extrapolate the retrieved rain rate downwards to the aircraft level by fitting an exponential function to each radar column. The assumption is that the rain rate varies with distance below the cloud base exponentially due to evaporation (Wood, 2005; Comstock et al., 2004). Figure S11 in the supporting information shows an example of rain rate derived from the exponential fit, and demonstrates that the exponentially fitted rain rate shows reasonable agreement with the retrieved rain rate where such is retrieved. Figure 8d compares the extrapolated rain rate from the Z-R relationship (red line), extrapolated rain rate from ZV retrieval (green line), extrapolated rain rate from radar-lidar retrieval (blue line). To further increase our confidence, we only compare the extrapolated rain rate from those periods where the original retrieved rain rate extends to within 200m of the aircraft (i.e. when the rain extends down to dotted reference line). Another challenge is the limited sampling volume of the in situ probes. To overcome this difficulty, we average the in situ DSD over a 20s period, marked as black squares in Figure 8d, and similarly, we also average the corresponding retrievals over the same 20s time window, marked by the red, green and blue dots. It can be seen that the retrieved rain rate shows reasonable agreement with in situ data for this case.

We repeated this analysis for the liquid-precipitation retrievals for all the SOCRATES flights and summarize the results in Figure 9. Overall, the Z-R, ZV, and radar-lidar retrievals compare well with the in situ, with Pearson correlation coefficient of 0.83. 0.88 and 0.68, respectively. Despite the simplicity of the approach, even the rain rate derived from Z-R relationship shows good performance compared to the in situ values, with a fractional difference (difference in 20s medians / average of 20s medians) of only -8.0%. If we estimate the uncertainty in the retrieved rain rate via error propagation, and we estimated the uncertainty in reflectivity as 1.5 dB for reflectivity (following O'Connor et al., 2005) and 10% for lidar backscatter (e.g., Schwartz et al., 2019), we estimate the uncertainty in the radar-lidar retrieved rain rate would be 18%. Similarly, with the uncertainty of 1.5 dB for reflectivity, and 10% uncertainty for terminal fall velocity (see Tansey et al., 2022), we estimate the uncertainty in the ZV retrieved rain rate to be 44%. As for the Z-R relationship (using the below-cloud sawtooth leg relationship), the estimated the uncertainty in rain rate is 38.4%. Relative to the expected uncertainties due simply from uncertainties in the inputs, all three retrievals compare well with the in situ data.

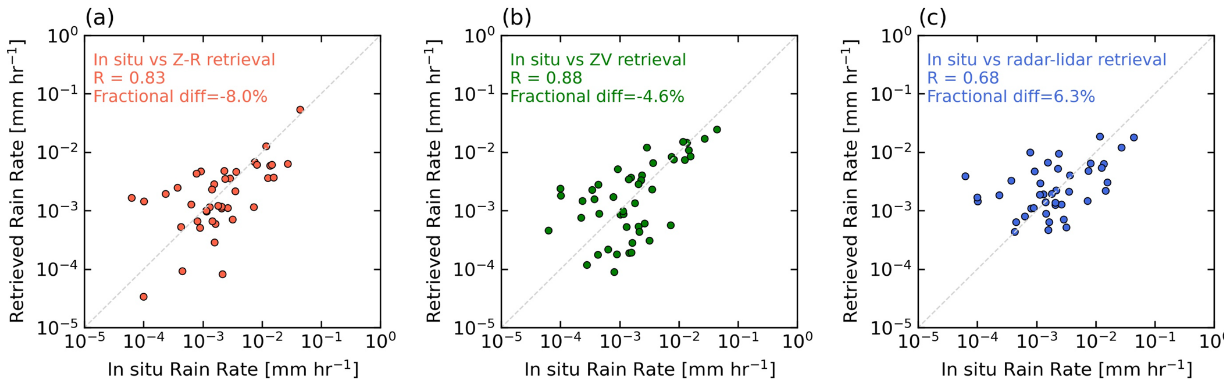

Figure 9. Comparison of in situ estimates with (a) Z-R retrieval, (b) ZV retrieval, and (c) radar-lidar retrieval for the entire campaign. The retrieved rain rates plotted here that were extrapolated to the aircraft level (see Figure 8, S11) to compare with the in situ data. Fractional difference is calculated as the difference between the retrieved and in situ median value divided by the average of the medians.

5 Vertical distribution of precipitation properties

In this section, we will apply the precipitation observations and retrievals to study the vertical distribution of precipitation properties.

Figure 10 shows a violin plot of in situ measured precipitation properties at different altitudes and retrieved precipitation properties below the lidar-inferred cloud base. For each dataset, the white dot represents the median value, while the black bar represents the interquartile range. Perhaps surprisingly rain rate decreases going downward from the top half of the cloud (i.e. the largest rain rates are in the upper portion of the cloud). Medians of rain rate at the cloud top half, cloud bottom half and below the cloud are of 0.021 mm hr^{-1}, 0.008 mm hr^{-1}, and 0.001 mm hr^{-1}. Similar to rain rate, there is also a decrease in precipitation number concentration (N_{precip}) and precipitation liquid water content (LWC_{precip}) moving downward from the top half of the cloud. In contrast, D_{precip} and σ_{precip} increase moving downward, that is bigger particles in the bottom half, and (just) below cloud. Overall, the retrieved precipitation properties (below the cloud base) compare well with the in situ estimates from the sawtooth below-cloud segments.

How do precipitation properties vary below cloud base? Figure 11 provides a more detailed view on the vertical distribution of precipitation properties below cloud base. Here, the column shows rain rate, N_{precip}, LWC_{precip}, D_{precip}, and σ_{precip}, respectively. The first two rows are histograms for radar-lidar and ZV retrievals, respectively. The last row is a box plot that summarizes both retrievals by binning the data vertically every 100 meters. Here, we only consider data in those radar columns where rain extend at least 400m below cloud base. Overall, both the mean rain rate and LWC_{precip} decrease exponentially with distance (as the change in the position of the distribution peak is roughly linear with distance on a log-scale). Both retrievals have similar values and rates of decrease (panel k and panel m). The e-folding distance over which the rain rate decrease to 1/e

(37%) of its initial value is about 260m for radar-lidar retrieval and 340 m for ZV retrieval. N_{precip} also decreases with distance, but we find the radar-lidar retrieval decreases more rapidly within the 200m below the cloud base, and the ZV retrieval shows higher N_{precip} than radar-lidar retrieval at different levels. This is consistent with (a result of) assuming a shape factor of zero in the ZV retrievals. The mean D_{precip} and σ_{precip} both increase with distance. Compared to radar-lidar retrieved D_{precip}, ZV retrieved D_{precip} is smaller overall (again consistent with the assumed shape factor), and has much less spread (variation) at any given altitude. Figure 10d shows that radar-lidar retrieved D_{precip} compare better with the in situ estimated D_{precip} from the below-cloud portion of the sawtooth legs than the ZV retrieved D_{precip}.

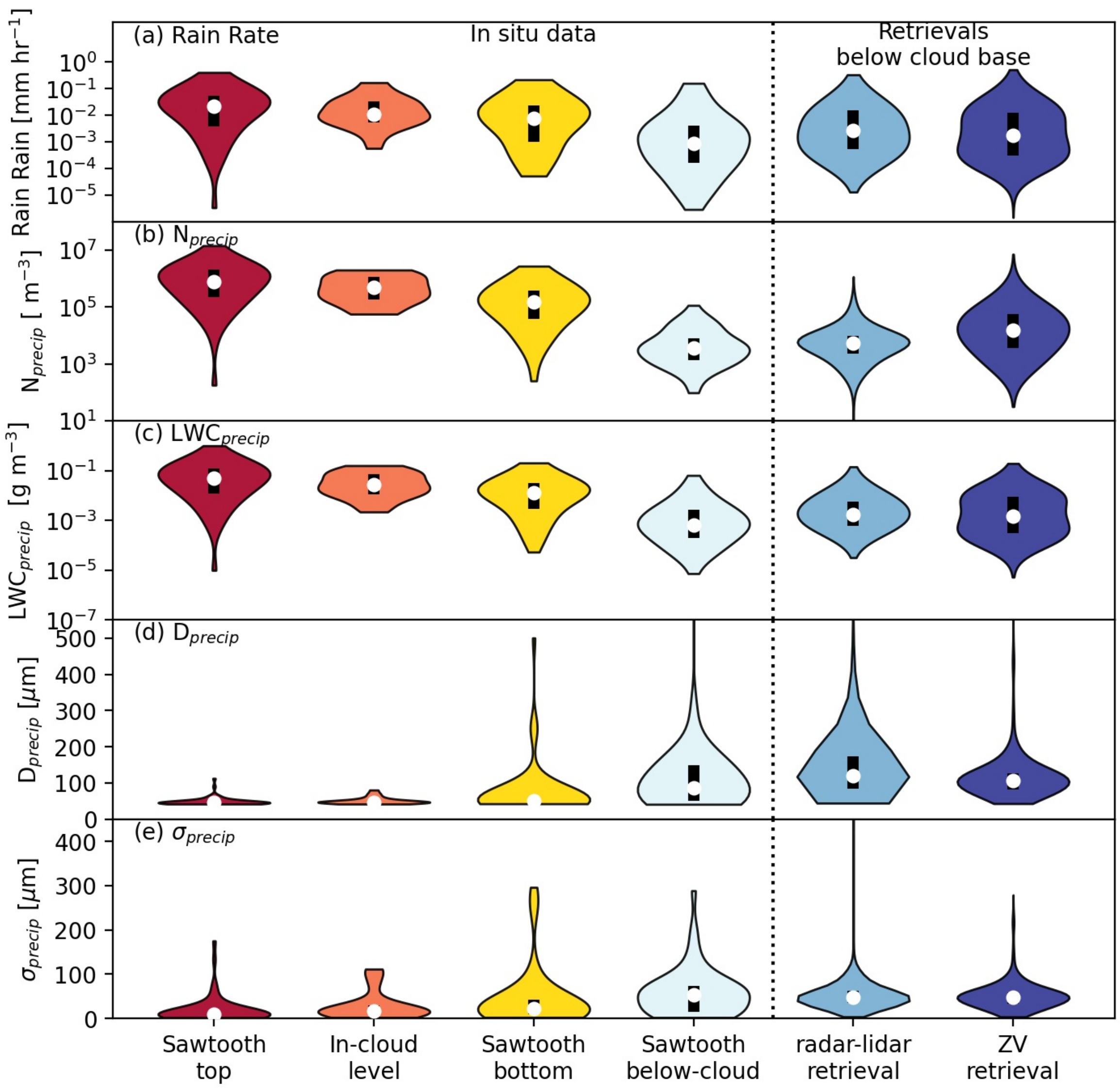

Figure 10. Violin plot for in situ measured precipitation properties at different altitudes and retrieved precipitation properties below cloud base: (a) rain rate (or precipitation liquid water flux), (b) precipitation number concentration N_{precip}, (c) precipitation liquid water content LWC_{precip}, (d) precipitation liquid water content weighted mean diameter D_{precip}, (e) precipitation liquid water content weighted width σ_{precip}. A violin plot can be regarded as a hybrid of a boxplot

and a kernel density plot. For each dataset, the white dot represents the median value, while the black bar represents the interquartile range, and the outer shape is the kernel density estimation to show the distribution of the data. In situ measured precipitation properties are from these legs (as marked in Figure S1): the top half of the cloud layer from sawtooth legs (sawtooth top); the bottom half of the cloud layer from sawtooth legs (sawtooth bottom); the below-cloud portion of the sawtooth legs (sawtooth below-cloud); and in-cloud level legs.

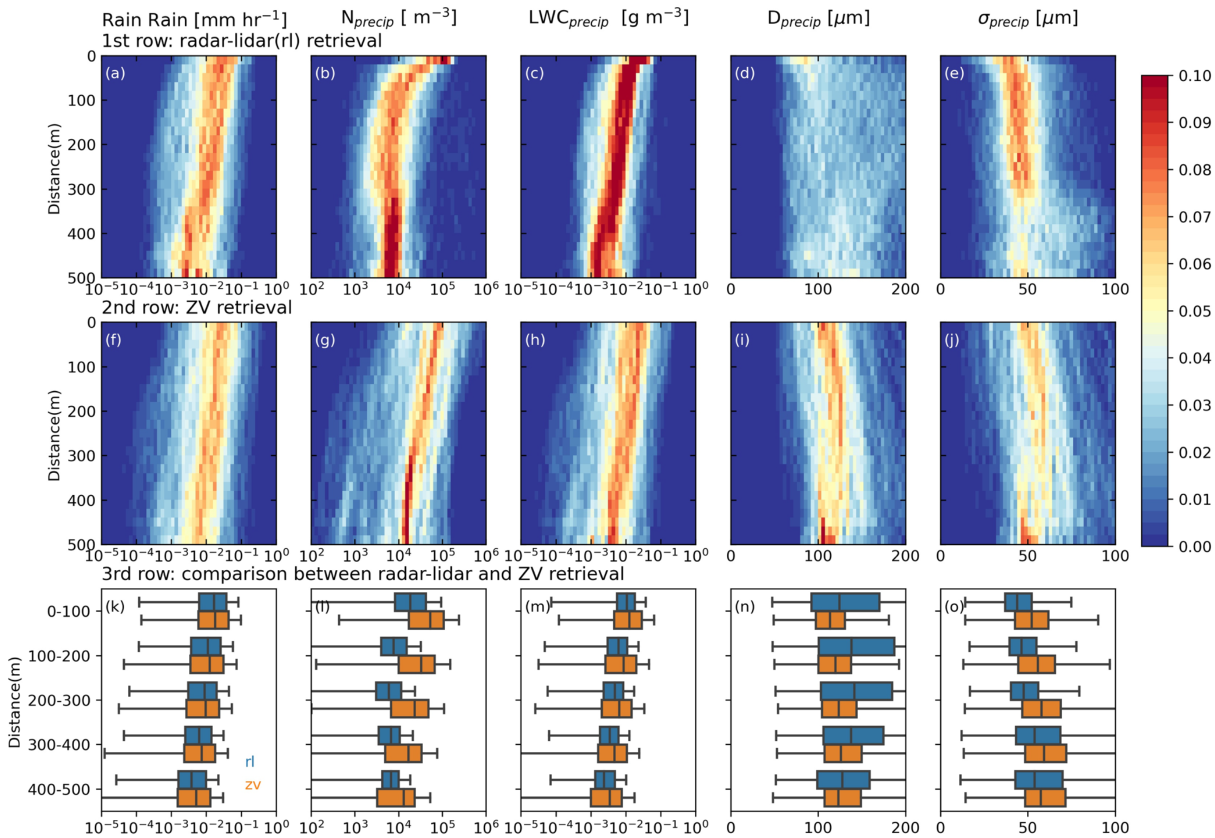

Figure 11. Vertical distributions of below-cloud-base precipitation properties from retrievals (each column is rain rate, N_{precip}, LWC_{precip}. D_{precip}, σ_{precip} respectively). The first and second row is the histogram of retrieved precipitation properties below-cloud-base (data are normalized at each level), and y axis is the distance away from the cloud-base. First row is the results from radar-lidar retrievals, the second row is the results from ZV retrievals. The last row is the box plot that summarized the data in the first two rows by binned the data vertically every 100 meters, where blue boxes are from radar-lidar retrievals, and orange boxes are from ZV retrievals.

6 Rain rate dependence on cloud depth and aerosol concentration

In this section, we examine the degree to which precipitation can be diagnosed from cloud depth and cloud droplet or aerosol number concentration in the form (e.g. Comstock et al., 2004; Terai et al.,2012; Mann et al., 2014)

$$R_{CB} = k\, H^{\alpha}\, N^{\beta} \tag{11}$$

where N is usually the cloud droplet (N_d) or aerosol number concentrations (N_a), and H is cloud depth or liquid water path, and R_{CB} is rain rate at cloud base. To our knowledge, such a relationship has not been examined over the SO, except by Mace and Avey (2007) who used satellite retrievals. To examine this relationship over the SO, we use radar-lidar retrieved rain rate for R_{CB} , use the difference between cloud top and cloud base for H, and use accumulation mode aerosol concentrations with diameters larger than 70 nm from UHSAS for N_a.

First, we broadly examine the rain rate dependence on either cloud depth or aerosol concentration, individually. Figure 12a shows a joint histogram of rain rate at cloud base and cloud depth. The histogram shows that rain rate (at cloud base) scales with cloud depth, such that thicker clouds are associated with higher rain rates. This is consistent with previous studies (e.g. vanZanten et al., 2005; Pawlowska and Brenguier, 2003; Geoffroy et al., 2008). And to demonstrate the rain rate dependence on aerosol concentration, Figure 12b shows the probability density function of rain rate partitioned for conditions with low aerosol concentrations (lower than the first quartile, marked as blue) and high aerosol concentrations (higher than the third quartile, marked as red). Figure 12b shows that overall higher aerosol concentrations are associated with lower rain rates, consistent with aerosol suppression of precipitation.

How does rain rate relate to both cloud depth and aerosol concentration? To derive the coefficients in equation (11), we divided cloud depth (H) up to 600m into 6 bins, and divided aerosol concentrations (N_a) into 4 bins, and calculated the median rain rate for each H and N_a pair. Then we performed linear least square regression on the natural logarithms of data from these 24 bins (Figure 12c). The derived relationship is $R_{CB} = 1.73 \times 10^{-10}\, H^{3.6}\, N_a^{-1}$, with H in m, N_a in cm^{-3}, and R_{CB} in mm hr^{-1}. Using bootstrap resampling technique, we estimate that the exponent α (one sigma uncertainty) for H range from 3.4 to 3.9, while the exponent β for N_a range from -1.3 to -0.8. The relationship we derive here is broadly similar to previous studies for stratocumulus in other regions. Exponent α for cloud depth typically is about 3 (vanZanten et al., 2005; Pawlowska and Brenguier, 2003; Lu et al., 2009), and the exponent β for number concentration (cloud droplet concentration or cloud condensation nuclei) typically ranges between -1.75 to -0.66 (vanZanten et al 2005; Mann et al., 2014; Lu et al., 2009; Comstock et al., 2004). The exponent β of -1 for aerosol concentration we derived here is smaller than exponent β of -0.32 in Mace and Avey (2017, hereafter M17), estimated using satellite-estimated cloud droplet number concentration, liquid water path, and rain rate for the SO. We will discuss this difference further at the of the next section.

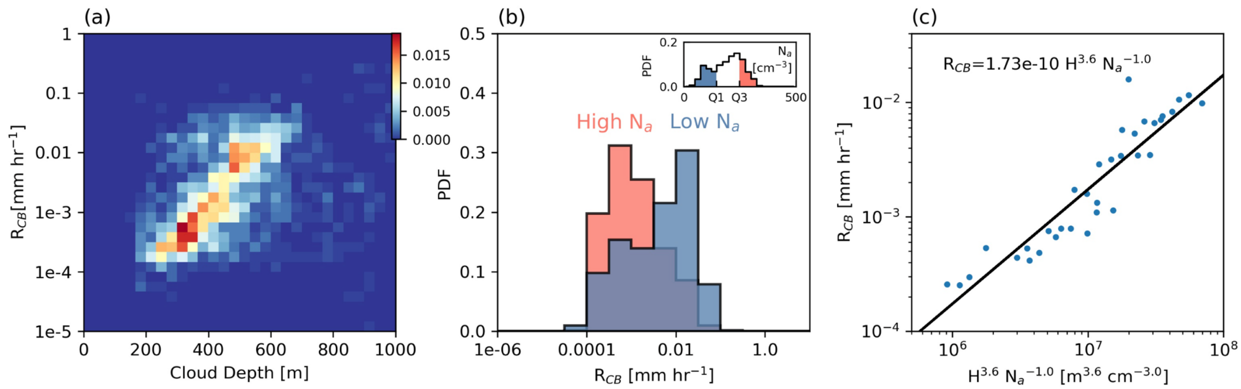

Figure 12. (a) Histogram of rain rate plotted as a function of cloud depth. (b) The probability density function of rain rate for conditions with low aerosol concentrations (lower than the first quartile, marked as blue) and high aerosol concentrations (higher than the third quartile, marked as red). (c) The rain rate at the cloud base is plotted as a function of the cloud depth, H, and aerosol concentration, N_a. Here H and N_a are the middle points for each cloud depth and aerosol concentration bin, while the rain rate at the cloud base is taken as the median value of rain rates in each cloud depth and aerosol concentration bin. The solid line shows the parametrization described in the main text.

7 Conclusions

In this study, we examine in-and-below-cloud precipitation properties for stratocumulus over the Southern Ocean (SO), leveraging data collected from airborne W-band Cloud Radar (HCR), High Spectral Resolution Lidar (HSRL), and various in situ probes during the Southern Ocean Clouds Radiation Aerosol Transport Experimental Study (SOCRATES) in January-February 2018.

Overall, we find that about 60% of the stratocumulus were precipitating, and about 80% of the stratocumulus to be cold-topped (with a cloud top temperature < 0^{o}C) based on periods where the aircraft were flying below cloud and the radar and lidar pointing toward zenith. We determine the precipitation phase using the lidar particle linear depolarization ratio PLDR and find that about 60% of the precipitation is liquid phase, and about 20% of the precipitation is ice phase, with the remaining 20% being ambiguous. While we can not rule out the possibility that any individual ambiguous cases is pure liquid, most of such cases are likely to have ice or mixed phase precipitation present. Further, for cold-topped cloud, we find that when the reflectivity factor is less than about -10 dBZ, the precipitation is predominately liquid, while reflectivity factors greater than 0 dBZ, precipitation is predominately ice. This results is similar to what was found by Mace and Protat (2018) based on CAPRICORN data the during March-April 2016, as well as a recent study by Tansey et al. (2023) based on surface data collected at Macquarie Island (54.5 ^{o}S) between March and November 2016. The SOCRATES data, collected in the Southern Hemisphere Summer, in January and February 2018, suggest this relationship is likely characteristic of SO low clouds through the year, and suggests that the measured reflectivity factor might be used as a proxy to determine the precipitation phase for *cold-topped Southern Ocean stratocumulus* with CloudSat (or other "radar only") retrievals where no other information is available to constrain the precipitation phase.

For liquid-phase precipitation, we performed retrievals for precipitation rain rate and other microphysical parameters based on cloud radar and lidar, with the goal to testing a hierarchy of retrieval methods, from the simplest Z-R relationship approach where only radar reflectivity (Z) is used to estimate the rain rate, to a reflectivity-velocity (ZV) retrieval where there are two observables (inputs to the retrieval), to a radar-lidar retrieval with three observables. Our evaluation show that rain rate from the Z-R, ZV, and radar-lidar retrievals all compare well with the in situ, with Pearson correlation coefficient of 0.83. 0.88 and. 0.68, and fractional difference (difference between the retrieved and in situ median value divided by the average of the medians) of only -8.0%, -4.6%, and 6.3%, respectively. In addition to rain rate, ZV and radar-lidar retrievals can retrieve other precipitation properties, such as, precipitation number concentration, precipitation liquid water content, number concentration, size and width. The overall statistics and distribution of these retrieved precipitation properties below the cloud base, also compare well with in situ estimates from the sawtooth below-cloud segments. This good performance gives us some confidence in using these retrieval techniques for SO stratocumulus, including in our recently published manuscript that examines coalescence scavenging in SO stratocumulus [Kang et al., 2022].

Despite the good retrieval performance overall, there are important caveats. When developing the power-law relationships between reflectivity (Z) and rain rate (R) following $Z = aR^b$ we found the *b* exponent varied little with altitude and had a value around 1.3 to 1.4. This is similar to values obtained in previous studies for stratocumulus in other regions (Comstock et al., 2004; vanZanten et al., 2005). The a coefficient, on the other hand, increases as one moves from the cloud layer to the surface. In general, one can derived a power-law relationship between Z and R based on the assumption of a modified gamma distribution (e.g., Rosenfeld and Ulbrich 2003) and doing so shows that one should expected the a coefficient to depend on the total droplet number concentration. Given the vertical variations in the precipitation droplet number concentration (see Figures 10 and 11), the vertical variation in the a coefficient is not surprising. But such also hints that the a coefficient may well vary with the accumulation mode aerosol concentration or other factors than control the cloud droplet number concentration. So Z-R relationships should be used with some caution in studies intending to establish relationships between rain rates and aerosols. We also find that the derived the derived Z-R relationships are sensitive to whether ones exclude drops with diameters around 10-40 μm when in cloud, because these drops make a non-trivial contribution to drizzle flux, as perhaps first noted by Nicholls (1984). Our analysis suggests that below-cloud Z-R equations should be applied with caution to in-cloud reflectivity measurements, and should be expected to underestimate the total liquid water flux in cloud.

Comparing the ZV retrieval with radar-lidar retrieval shows that both retrievals capture the mean vertical structure of precipitation microphysics below cloud. Based on in situ data and retrievals, we found that rain rate, precipitation number concentration (N_{precip}), precipitation liquid water (LWC_{precip}) all decreases as one get closer to the surface, while precipitation liquid water content weighted mean diameter (D_{precip}) and width(σ_{precip}) increases. The e-folding distance over which the rain rate decrease to 1/e (37%) of its initial value is about 260m for radar-lidar retrieval and 340 m for ZV retrieval. However, we find that both D_0 and N_{precip} from the ZV retrieval have less spatial variability than that from the radar-lidar retrieval, and assuming a shape factor of $\mu = 0$, results in the ZV retrieved mean D_0 being a bit too small and N_{precip} being too large as compared to the radar-lidar retrieval. This is because the shape factor is not constant and in particular, because the shape factor in the stronger precipitation shafts below the thicker portion of the clouds should be larger than zero (because the precipitation DSD is narrower with a more well defined peaked rather than a broad exponential-like distribution).

This study also explored rain rate dependence on cloud depth and aerosol concentration. Rain rate at cloud base (R_{CB}) increases with cloud depth (H) and decreases with aerosol concentration (N_a). Using a least-squares regression, we found R_{CB} varies as $H^{3.6}\ N_a^{-1}$, which is broadly consistent with estimates for stratocumulus in previous studies over other regions (vanZanten et al., 2005; Pawlowska & Brenguier, 2003; Lu et al., 2009; Mann et al., 2014; Lu et al., 2009; Comstock et al., 2004). However as noted in section 6, our results differ with the satellite-based estimates for the SO by Mace and Avey (2007), hereafter M17, who suggest an exponent of -0.32 for the aerosol concentration based on satellite retrievals. M17 also noted that their estimates differ from previous studies in other regions. There are a variety of potential reasons for the different results in our study and in M17. The first obvious reason is different data sources. Our study used in situ measured N_a and retrieved rain rate with airborne radar and lidar measurements, while M17 used N_d, liquid water path and rain rate derived from MODIS and Cloudsat based on an optimal estimation algorithm. Another reason might be different cloud populations; where in our study about 80% of the clouds are cold-topped, M17 restricted their analysis to warm-topped clouds. Data collected during the Macquarie Island Cloud and Radiation Experiment (MICRE), suggest that warm topped SO clouds are geometrically thinner and closer to the surface than cold-topped clouds [Tansey et al., 2023, submitted]. As-is, we end this study here, leaving a regime-dependent analysis of precipitation susceptibility for a future study. As more data is collected, including in future campaigns such as the upcoming Clouds And Precipitation Experiment at Kennaook (CAPE-K) that will begin in March 2024, the aerosol sensitivity of low altitude SO clouds is certain to be focus of future multi- or cross-experiments studies.

Acknowledgments

This work was supported by the U.S. National Science Foundation on grant AGS-2124993. We would like to thank the contribution from the many individuals and teams associated with the NCAR Earth Observing Laboratory, SOCRATES Science and Aircraft Instrument Teams. We thank Dr. Ulrike Romatschke for helping with radar data processing. We also would like to thank open-source codes such as miepython and CloudnetPy.

Open Research

The authors would like to acknowledge the SOCRATES Project for providing data through the SOCRATES Data Archive Center (SDAC) at NCAR's Earth Observing Laboratory: (1) low rate (1 Hz) navigation, state parameter, and microphysics flight-level data (contain data from many probes, including CDP and UHSAS) version 1.4 https://data.eol.ucar.edu/dataset/552.002; (2) 2DS data version 1.1 (1 Hz) https://data.eol.ucar.edu/dataset/552.047; (3) HCR radar and HSRL lidar moments data (2 Hz) https://data.eol.ucar.edu/dataset/552.034. Miepython is avaliable at https://miepython.readthedocs.io/en/latest/.

References

Arabzadeh, A., Ehsani, M. R., Guan, B., Heflin, S., & Behrangi, A. (2020). Global Intercomparison of Atmospheric Rivers Precipitation in Remote Sensing and Reanalysis Products. *Journal of Geophysical Research: Atmospheres*, *125*(21), e2020JD033021. https://doi.org/10.1029/2020JD033021

Bai, H., Gong, C., Wang, M., Zhang, Z., & L'Ecuyer, T. (2018). Estimating precipitation susceptibility in warm marine clouds using multi-sensor aerosol and cloud products from A-Train satellites. *Atmospheric Chemistry and Physics*, *18*(3), 1763–1783. https://doi.org/10.5194/acp-18-1763-2018

Beard, K. V. (1976). Terminal Velocity and Shape of Cloud and Precipitation Drops Aloft. *Journal of the Atmospheric Sciences*, *33*(5), 851–864. https://doi.org/10.1175/1520-0469(1976)033<0851:TVASOC>2.0.CO;2

Behrangi, A., Lebsock, M., Wong, S., & Lambrigtsen, B. (2012). On the quantification of oceanic rainfall using spaceborne sensors. *Journal of Geophysical Research: Atmospheres*, *117*(D20). https://doi.org/10.1029/2012JD017979

Behrangi, A., Stephens, G., Adler, R. F., Huffman, G. J., Lambrigtsen, B., & Lebsock, M. (2014). An Update on the Oceanic Precipitation Rate and Its Zonal Distribution in Light of Advanced Observations from Space. *Journal of Climate*, *27*(11), 3957–3965. https://doi.org/10.1175/JCLI-D-13-00679.1

Bellouin, N., Quaas, J., Gryspeerdt, E., Kinne, S., Stier, P., Watson-Parris, D., et al. (2020). Bounding Global Aerosol Radiative Forcing of Climate Change. *Reviews of Geophysics*, *58*(1), e2019RG000660. https://doi.org/10.1029/2019RG000660

Bjordal, J., Storelvmo, T., Alterskjær, K., & Carlsen, T. (2020). Equilibrium climate sensitivity above 5 °C plausible due to state-dependent cloud feedback. Nature Geoscience, 13(11), 718–721. https://doi.org/10.1038/s41561-020-00649-1

Bodas-Salcedo, A., Hill, P. G., Furtado, K., Williams, K. D., Field, P. R., Manners, J. C., et al. (2016). Large Contribution of Supercooled Liquid Clouds to the Solar Radiation Budget of the Southern Ocean. *Journal of Climate*, *29*(11), 4213–4228. https://doi.org/10.1175/JCLI-D-15-0564.1

Bohren, C. F., & Huffman, D. R. (1983). Absorption and scattering of light by small particles. Weinheim: Wiley : Wiley Online Library.

Bromwich, D. H., Nicolas, J. P., & Monaghan, A. J. (2011). An Assessment of Precipitation Changes over Antarctica and the Southern Ocean since 1989 in Contemporary Global Reanalyses. *Journal of Climate*, *24*(16), 4189–4209. https://doi.org/10.1175/2011JCLI4074.1

Cesana, G. V., Khadir, T., Chepfer, H., & Chiriaco, M. (2022). Southern Ocean Solar Reflection Biases in CMIP6 Models Linked to Cloud Phase and Vertical Structure Representations. *Geophysical Research Letters*, *49*(22), e2022GL099777. https://doi.org/10.1029/2022GL099777

Comstock, K. K., Wood, R., Yuter, S. E., & Bretherton, C. S. (2004). Reflectivity and rain rate in and below drizzling stratocumulus. *Quarterly Journal of the Royal Meteorological Society*, *130*(603), 2891–2918. https://doi.org/10.1256/qj.03.187

de Lavergne, C., Palter, J. B., Galbraith, E. D., Bernardello, R., & Marinov, I. (2014). Cessation of deep convection in the open Southern Ocean under anthropogenic climate change. *Nature Climate Change*, *4*(4), 278–282. https://doi.org/10.1038/nclimate2132

DMT. (2013). Ultra high sensitivity aerosol spectrometer (UHSAS) Operator Manual.

Eastman, R., Lebsock, M., & Wood, R. (2019). Warm Rain Rates from AMSR-E 89-GHz Brightness Temperatures Trained Using CloudSat Rain-Rate Observations. Journal of Atmospheric and Oceanic Technology, 36(6), 1033–1051. https://doi.org/10.1175/JTECH-D-18-0185.1

Ellis, S. M., Tsai, P., Burghart, C., Romatschke, U., Dixon, M., Vivekanandan, J., et al. (2019). Use of the Earth's Surface as a Reference to Correct Airborne Nadir-Looking Radar Radial Velocity Measurements for Platform Motion. Journal of Atmospheric and Oceanic Technology, 36(7), 1343–1360. https://doi.org/10.1175/JTECH-D-19-0019.1

Ellis, T. D., L'Ecuyer, T., Haynes, J. M., & Stephens, G. L. (2009). How often does it rain over the global oceans? The perspective from CloudSat. *Geophysical Research Letters*, *36*(3). https://doi.org/10.1029/2008GL036728

Eloranta, E. E. (2005). High Spectral Resolution Lidar. In C. Weitkamp (Ed.), *Lidar: Range-Resolved Optical Remote Sensing of the Atmosphere* (pp. 143–163). New York, NY: Springer. https://doi.org/10.1007/0-387-25101-4_5

Feingold, G., McComiskey, A., Rosenfeld, D., & Sorooshian, A. (2013). On the relationship between cloud contact time and precipitation susceptibility to aerosol. *Journal of Geophysical Research: Atmospheres*, *118*(18), 10,544-10,554. https://doi.org/10.1002/jgrd.50819

Frisch, A. S., Fairall, C. W., & Snider, J. B. (1995). Measurement of Stratus Cloud and Drizzle Parameters in ASTEX with a Kα-Band Doppler Radar and a Microwave Radiometer. *Journal of the Atmospheric Sciences*, *52*(16), 2788–2799. https://doi.org/10.1175/1520-0469(1995)052<2788:MOSCAD>2.0.CO;2

Frölicher, T. L., Sarmiento, J. L., Paynter, D. J., Dunne, J. P., Krasting, J. P., & Winton, M. (2015). Dominance of the Southern Ocean in Anthropogenic Carbon and Heat Uptake in CMIP5 Models. *Journal of Climate*, *28*(2), 862–886. https://doi.org/10.1175/JCLI-D-14-00117.1

Fyfe, J. C., Gillett, N. P., & Marshall, G. J. (2012). Human influence on extratropical Southern Hemisphere summer precipitation. *Geophysical Research Letters*, *39*(23). https://doi.org/10.1029/2012GL054199

Ghate, V. P., & Cadeddu, M. P. (2019). Drizzle and turbulence below closed cellular marine stratocumulus clouds. Journal of Geophysical Research-Atmospheres, 124(11), 2018JD030141. https://doi.org/10.1029/2018JD030141

Grecu, M., Olson, W. S., Munchak, S. J., Ringerud, S., Liao, L., Haddad, Z., et al. (2016). The GPM Combined Algorithm. *Journal of Atmospheric and Oceanic Technology*, *33*(10), 2225–2245. https://doi.org/10.1175/JTECH-D-16-0019.1

Hamilton, D. S., Lee, L. A., Pringle, K. J., Reddington, C. L., Spracklen, D. V., & Carslaw, K. S. (2014). Occurrence of pristine aerosol environments on a polluted planet. *Proceedings of the National Academy of Sciences*, *111*(52), 18466–18471. https://doi.org/10.1073/pnas.1415440111

Hayden, L., & Liu, C. (2018). A Multiyear Analysis of Global Precipitation Combining CloudSat and GPM Precipitation Retrievals. *Journal of Hydrometeorology*, *19*(12), 1935–1952. https://doi.org/10.1175/JHM-D-18-0053.1

Haynes, J. M., L'Ecuyer, T. S., Stephens, G. L., Miller, S. D., Mitrescu, C., Wood, N. B., & Tanelli, S. (2009). Rainfall retrieval over the ocean with spaceborne W-band radar.

Journal of Geophysical Research: Atmospheres, *114*(D8). https://doi.org/10.1029/2008JD009973

Kang, L., Marchand, R. T., Wood, R., & McCoy, I. L. (2022). Coalescence Scavenging Drives Droplet Number Concentration in Southern Ocean Low Clouds. *Geophysical Research Letters*, *49*(7), e2022GL097819. https://doi.org/10.1029/2022GL097819

Kang, L., Marchand, R., & Smith, W. (2021). Evaluation of MODIS and Himawari-8 Low Clouds Retrievals Over the Southern Ocean With In Situ Measurements From the SOCRATES Campaign. *Earth and Space Science*, *8*(3), e2020EA001397. https://doi.org/10.1029/2020EA001397

Khatiwala, S., Primeau, F., & Hall, T. (2009). Reconstruction of the history of anthropogenic CO2 concentrations in the ocean. *Nature*, *462*(7271), 346–349. https://doi.org/10.1038/nature08526

Klepp, C., Michel, S., Protat, A., Burdanowitz, J., Albern, N., Kähnert, M., et al. (2018). OceanRAIN, a new in-situ shipboard global ocean surface-reference dataset of all water cycle components. *Scientific Data*, *5*(1), 180122. https://doi.org/10.1038/sdata.2018.122

Lance, S., Brock, C. A., Rogers, D., & Gordon, J. A. (2010). Water droplet calibration of the Cloud Droplet Probe (CDP) and in-flight performance in liquid, ice and mixed-phase clouds during ARCPAC. *Atmospheric Measurement Techniques*, *3*(6), 1683–1706. https://doi.org/10.5194/amt-3-1683-2010

Lang, F., Huang, Y., Siems, S. T., & Manton, M. J. (2018). Characteristics of the Marine Atmospheric Boundary Layer Over the Southern Ocean in Response to the Synoptic Forcing. *Journal of Geophysical Research: Atmospheres*, *123*(15), 7799–7820. https://doi.org/10.1029/2018JD028700

Lee, L. A., Reddington, C. L., & Carslaw, K. S. (2016). On the relationship between aerosol model uncertainty and radiative forcing uncertainty. *Proceedings of the National Academy of Sciences*, *113*(21), 5820–5827. https://doi.org/10.1073/pnas.1507050113

Lu, M.-L., Sorooshian, A., Jonsson, H. H., Feingold, G., Flagan, R. C., & Seinfeld, J. H. (2009). Marine stratocumulus aerosol-cloud relationships in the MASE-II experiment: Precipitation susceptibility in eastern Pacific marine stratocumulus. *Journal of Geophysical Research: Atmospheres*, *114*(D24). https://doi.org/10.1029/2009JD012774

Mace, G. G., & Avey, S. (2017). Seasonal variability of warm boundary layer cloud and precipitation properties in the Southern Ocean as diagnosed from A-Train data. Journal of Geophysical Research: Atmospheres, 122(2), 1015–1032. https://doi.org/10.1002/2016JD025348

Mace, G. G., & Protat, A. (2018). Clouds over the Southern Ocean as Observed from the R/V Investigator during CAPRICORN. Part I: Cloud Occurrence and Phase Partitioning. Journal of Applied Meteorology and Climatology, 57(8), 1783–1803. https://doi.org/10.1175/JAMC-D-17-0194.1

Mace, G. G., Heymsfield, A. J., & Poellot, M. R. (2002). On retrieving the microphysical properties of cirrus clouds using the moments of the millimeter-wavelength Doppler spectrum. *Journal of Geophysical Research: Atmospheres*, *107*(D24), AAC 22-1-AAC 22-26. https://doi.org/10.1029/2001JD001308

Mann, J. A. L., Christine Chiu, J., Hogan, R. J., O'Connor, E. J., L'Ecuyer, T. S., Stein, T. H. M., & Jefferson, A. (2014). Aerosol impacts on drizzle properties in warm clouds from ARM Mobile Facility maritime and continental deployments. *Journal of Geophysical Research: Atmospheres*, *119*(7), 4136–4148. https://doi.org/10.1002/2013JD021339

Manton, M. J., Huang, Y., & Siems, S. T. (2020). Variations in Precipitation across the Southern Ocean. *Journal of Climate*, *33*(24), 10653–10670. https://doi.org/10.1175/JCLI-D-20-0120.1

Marchand, R. T., Ackerman, T. P., & Moroney, C. (2007). An assessment of Multiangle Imaging Spectroradiometer (MISR) stereo-derived cloud top heights and cloud top winds using ground-based radar, lidar, and microwave radiometers. *Journal of Geophysical Research: Atmospheres*, *112*(D6). https://doi.org/10.1029/2006JD007091

Marchand, R., Mace, G. G., Ackerman, T., & Stephens, G. (2008). Hydrometeor Detection Using Cloudsat—An Earth-Orbiting 94-GHz Cloud Radar. *Journal of Atmospheric and Oceanic Technology*, *25*(4), 519–533. https://doi.org/10.1175/2007JTECHA1006.1

McCoy, I. L., McCoy, D. T., Wood, R., Regayre, L., Watson-Parris, D., Grosvenor, D. P., et al. (2020). The hemispheric contrast in cloud microphysical properties constrains aerosol forcing. *Proceedings of the National Academy of Sciences of the United States of America*, *117*(32), 18998–19006. https://doi.org/10.1073/pnas.1922502117

McFarquhar, G. M., Bretherton, C. S., Marchand, R., Protat, A., DeMott, P. J., Alexander, S. P., et al. (2021). Observations of Clouds, Aerosols, Precipitation, and Surface Radiation over the Southern Ocean: An Overview of CAPRICORN, MARCUS, MICRE, and SOCRATES. *Bulletin of the American Meteorological Society*, *102*(4), E894–E928. https://doi.org/10.1175/BAMS-D-20-0132.1

Mitrescu, C., L'Ecuyer, T., Haynes, J., Miller, S., & Turk, J. (2010). CloudSat Precipitation Profiling Algorithm—Model Description. *Journal of Applied Meteorology and Climatology*, *49*(5), 991–1003. https://doi.org/10.1175/2009JAMC2181.1

Mohrmann, J., Wood, R., McGibbon, J., Eastman, R., & Luke, E. (2018). Drivers of Seasonal Variability in Marine Boundary Layer Aerosol Number Concentration Investigated Using a Steady State Approach. *Journal of Geophysical Research: Atmospheres*, *123*(2), 1097–1112. https://doi.org/10.1002/2017JD027443

Montoya Duque, E., Huang, Y., Siems, S. T., May, P. T., Protat, A., & McFarquhar, G. M. (2022). A Characterization of Clouds and Precipitation Over the Southern Ocean From Synoptic to Micro Scales During the CAPRICORN Field Campaigns. *Journal of Geophysical Research: Atmospheres*, *127*(17), e2022JD036796. https://doi.org/10.1029/2022JD036796

Mülmenstädt, J., Salzmann, M., Kay, J. E., Zelinka, M. D., Ma, P.-L., Nam, C., et al. (2021). An underestimated negative cloud feedback from cloud lifetime changes. *Nature Climate Change*, *11*(6), 508–513. https://doi.org/10.1038/s41558-021-01038-1

NCAR/EOL HCR Team. 2022. SOCRATES: NCAR HCR radar moments data. Version 3.1. UCAR/NCAR - Earth Observing Laboratory. https://doi.org/10.5065/D68914PH.

Nicholls, S. (1984). The dynamics of stratocumulus: Aircraft observations and comparisons with a mixed layer model. Quarterly Journal of the Royal Meteorological Society, 110(466), 783–820. https://doi.org/10.1002/qj.49711046603

Nicolas, J. P., & Bromwich, D. H. (2011). Precipitation Changes in High Southern Latitudes from Global Reanalyses: A Cautionary Tale. *Surveys in Geophysics*, *32*(4), 475–494. https://doi.org/10.1007/s10712-011-9114-6

O'Connor, E. J., Hogan, R. J., & Illingworth, A. J. (2005). Retrieving Stratocumulus Drizzle Parameters Using Doppler Radar and Lidar. *Journal of Applied Meteorology and Climatology*, *44*(1), 14–27. https://doi.org/10.1175/JAM-2181.1

Orr, B. W., & Kropfli, R. A. (1999). A Method for Estimating Particle Fall Velocities from Vertically Pointing Doppler Radar. *Journal of Atmospheric and Oceanic Technology*, *16*(1), 29–37. https://doi.org/10.1175/1520-0426(1999)016<0029:AMFEPF>2.0.CO;2

Pauling, A. G., Bitz, C. M., Smith, I. J., & Langhorne, P. J. (2016). The Response of the Southern Ocean and Antarctic Sea Ice to Freshwater from Ice Shelves in an Earth System Model. *Journal of Climate*, *29*(5), 1655–1672. https://doi.org/10.1175/JCLI-D-15-0501.1

Pawlowska, H., & Brenguier, J.-L. (2003). An observational study of drizzle formation in stratocumulus clouds for general circulation model (GCM) parameterizations. *Journal of Geophysical Research: Atmospheres*, *108*(D15). https://doi.org/10.1029/2002JD002679

Protat, A., Klepp, C., Louf, V., Petersen, W. A., Alexander, S. P., Barros, A., et al. (2019a). The Latitudinal Variability of Oceanic Rainfall Properties and Its Implication for Satellite Retrievals: 1. Drop Size Distribution Properties. *Journal of Geophysical Research: Atmospheres*, *124*(23), 13291–13311. https://doi.org/10.1029/2019JD031010

Protat, A., Klepp, C., Louf, V., Petersen, W. A., Alexander, S. P., Barros, A., et al. (2019b). The Latitudinal Variability of Oceanic Rainfall Properties and Its Implication for Satellite Retrievals: 1. Drop Size Distribution Properties. *Journal of Geophysical Research: Atmospheres*, *124*(23), 13291–13311. https://doi.org/10.1029/2019JD031010

Romatschke, U., Dixon, M., Tsai, P., Loew, E., Vivekanandan, J., Emmett, J., & Rilling, R. (2021). The NCAR Airborne 94-GHz Cloud Radar: Calibration and Data Processing. Data, 6(6), 66. https://doi.org/10.3390/data6060066

Rosenfeld, D., & Ulbrich, C. W. (2003). Cloud Microphysical Properties, Processes, and Rainfall Estimation Opportunities. *Meteorological Monographs*, *30*(52), 237–258. https://doi.org/10.1175/0065-9401(2003)030<0237:CMPPAR>2.0.CO;2

Sanchez, K. J., Roberts, G. C., Saliba, G., Russell, L. M., Twohy, C., Reeves, J. M., et al. (2021). Measurement report: Cloud processes and the transport of biological emissions affect southern ocean particle and cloud condensation nuclei concentrations. *Atmospheric Chemistry and Physics*, *21*(5), 3427–3446. https://doi.org/10.5194/acp-21-3427-2021

Sarkar, M., Zuidema, P., & Ghate, V. (2021). Clarifying Remotely Retrieved Precipitation of Shallow Marine Clouds from the NSF/NCAR Gulfstream V. *Journal of Atmospheric and Oceanic Technology*, *38*(9), 1657–1670. https://doi.org/10.1175/JTECH-D-20-0166.1

Sarmiento, J. L., Hughes, T. M. C., Stouffer, R. J., & Manabe, S. (1998). Simulated response of the ocean carbon cycle to anthropogenic climate warming. *Nature*, *393*(6682), 245–249. https://doi.org/10.1038/30455

Sassen, K., & Liao, L. (1996). Estimation of Cloud Content by W-Band Radar. *Journal of Applied Meteorology and Climatology*, *35*(6), 932–938. https://doi.org/10.1175/1520-0450(1996)035<0932:EOCCBW>2.0.CO;2

Schwartz, M. C., Ghate, V. P., Albrecht, B. A., Zuidema, P., Cadeddu, M. P., Vivekanandan, J., et al. (2019). Merged Cloud and Precipitation Dataset from the HIAPER GV for the Cloud System Evolution in the Trades (CSET) Campaign. *Journal of Atmospheric and Oceanic Technology*, *36*(6), 921–940. https://doi.org/10.1175/JTECH-D-18-0111.1

Seto, S., Iguchi, T., & Oki, T. (2013). The Basic Performance of a Precipitation Retrieval Algorithm for the Global Precipitation Measurement Mission’s Single/Dual-Frequency Radar Measurements. *IEEE Transactions on Geoscience and Remote Sensing*, *51*(12), 5239–5251. https://doi.org/10.1109/TGRS.2012.2231686

Smalley, K. M., Lebsock, M. D., Eastman, R., Smalley, M., & Witte, M. K. (2022). A Lagrangian analysis of pockets of open cells over the southeastern Pacific. *Atmospheric Chemistry and Physics*, *22*(12), 8197–8219. https://doi.org/10.5194/acp-22-8197-2022

Stephens, G. L., L'Ecuyer, T., Forbes, R., Gettelmen, A., Golaz, J.-C., Bodas-Salcedo, A., et al. (2010). Dreary state of precipitation in global models. *Journal of Geophysical Research: Atmospheres*, *115*(D24). https://doi.org/10.1029/2010JD014532

Swart, N. C., Gille, S. T., Fyfe, J. C., & Gillett, N. P. (2018). Recent Southern Ocean warming and freshening driven by greenhouse gas emissions and ozone depletion. *Nature Geoscience*, *11*(11), 836–841. https://doi.org/10.1038/s41561-018-0226-1

Tan, I., Storelvmo, T., & Zelinka, M. D. (2016). Observational constraints on mixed-phase clouds imply higher climate sensitivity. *Science*, *352*(6282), 224–227. https://doi.org/10.1126/science.aad5300

Tansey, E., Marchand, R. T., Alexander, S. P., Klekociuk, A. R., & Protat, A. (2023). Southern Ocean low cloud and precipitation phase observed during the Macquarie Island Cloud and Radiation Experiment (MICRE) (preprint). Preprints. https://doi.org/10.22541/essoar.168394768.89694625/v1

Tansey, E., Marchand, R., Protat, A., Alexander, S. P., & Ding, S. (2022). Southern Ocean Precipitation Characteristics Observed From CloudSat and Ground Instrumentation During the Macquarie Island Cloud & Radiation Experiment (MICRE): April 2016 to March 2017. *Journal of Geophysical Research: Atmospheres*, *127*(5), e2021JD035370. https://doi.org/10.1029/2021JD035370

Terai, C. R., Wood, R., Leon, D. C., & Zuidema, P. (2012). Does precipitation susceptibility vary with increasing cloud thickness in marine stratocumulus? *Atmospheric Chemistry and Physics*, *12*(10), 4567–4583. https://doi.org/10.5194/acp-12-4567-2012

Trenberth, K. E., & Fasullo, J. T. (2010). Simulation of Present-Day and Twenty-First-Century Energy Budgets of the Southern Oceans. *Journal of Climate*, *23*(2), 440–454. https://doi.org/10.1175/2009JCLI3152.1

UCAR/NCAR - Earth Observing Laboratory. 2022. SOCRATES: Low Rate (LRT - 1 sps) Navigation, State Parameter, and Microphysics Flight-Level Data. Version 1.4. UCAR/NCAR - Earth Observing Laboratory. https://doi.org/10.5065/D6M32TM9.

Vali, G., Kelly, R. D., French, J., Haimov, S., Leon, D., McIntosh, R. E., & Pazmany, A. (1998). Finescale Structure and Microphysics of Coastal Stratus. *Journal of the Atmospheric Sciences*, *55*(24), 3540–3564. https://doi.org/10.1175/1520-0469(1998)055<3540:FSAMOC>2.0.CO;2

vanZanten, M. C., Stevens, B., Vali, G., & Lenschow, D. H. (2005). Observations of Drizzle in Nocturnal Marine Stratocumulus. *Journal of the Atmospheric Sciences*, *62*(1), 88–106. https://doi.org/10.1175/JAS-3355.1

Vivekanandan, J., Ellis, S., Tsai, P., Loew, E., Lee, W.-C., Emmett, J., et al. (2015). A wing pod-based millimeter wavelength airborne cloud radar. *Geoscientific Instrumentation, Methods and Data Systems*, *4*(2), 161–176. https://doi.org/10.5194/gi-4-161-2015

von Terzi, L., Dias Neto, J., Ori, D., Myagkov, A., & Kneifel, S. (2022). Ice microphysical processes in the dendritic growth layer: a statistical analysis combining multi-frequency and polarimetric Doppler cloud radar observations. *Atmospheric Chemistry and Physics*, *22*(17), 11795–11821. https://doi.org/10.5194/acp-22-11795-2022

Wang, H., & Feingold, G. (2009). Modeling Mesoscale Cellular Structures and Drizzle in Marine Stratocumulus. Part I: Impact of Drizzle on the Formation and Evolution of Open

Cells. *Journal of the Atmospheric Sciences*, *66*(11), 3237–3256. https://doi.org/10.1175/2009JAS3022.1

Wilks, D. S. (1997). Resampling Hypothesis Tests for Autocorrelated Fields. *Journal of Climate*, *10*(1), 65–82. https://doi.org/10.1175/1520-0442(1997)010<0065:RHTFAF>2.0.CO;2

Wiscombe, J. (1979). Mie Scattering Calculations: Advances in Technique and Fast, Vector-speed Computer Codes. https://doi.org/10.5065/D6ZP4414

Wood, R. (2005). Drizzle in Stratiform Boundary Layer Clouds. Part II: Microphysical Aspects. *Journal of the Atmospheric Sciences*, *62*(9), 3034–3050. https://doi.org/10.1175/JAS3530.1

Wood, R., Bretherton, C. S., Leon, D., Clarke, A. D., Zuidema, P., Allen, G., & Coe, H. (2011). An aircraft case study of the spatial transition from closed to open mesoscale cellular convection over the Southeast Pacific. *Atmospheric Chemistry and Physics*, *11*(5), 2341–2370. https://doi.org/10.5194/acp-11-2341-2011

Wu, W., McFarquhar, G. 2019. NSF/NCAR GV HIAPER 2D-S Particle Size Distribution (PSD) Product Data. Version 1.1. UCAR/NCAR - Earth Observing Laboratory. https://doi.org/10.26023/8HMG-WQP3-XA0X.

Yamaguchi, T., & Feingold, G. (2015). On the relationship between open cellular convective cloud patterns and the spatial distribution of precipitation. *Atmospheric Chemistry and Physics*, *15*(3), 1237–1251. https://doi.org/10.5194/acp-15-1237-2015

Yang, F., Luke, E. P., Kollias, P., Kostinski, A. B., & Vogelmann, A. M. (2018). Scaling of drizzle virga depth with cloud thickness for marine stratocumulus clouds. Geophysical Research Letters, 45(8), 3746–3753. https://doi.org/10.1029/2018GL077145

Zelinka, M. D., Myers, T. A., McCoy, D. T., Po-Chedley, S., Caldwell, P. M., Ceppi, P., et al. (2020). Causes of Higher Climate Sensitivity in CMIP6 Models. *Geophysical Research Letters*, *47*(1), e2019GL085782. https://doi.org/10.1029/2019GL085782

Zhang, D., Wang, Z., Luo, T., Yin, Y., & Flynn, C. (2017). The occurrence of ice production in slightly supercooled Arctic stratiform clouds as observed by ground-based remote sensors at the ARM NSA site. *Journal of Geophysical Research: Atmospheres*, *122*(5), 2867–2877. https://doi.org/10.1002/2016JD026226

Zhou, X., Atlas, R., McCoy, I. L., Bretherton, C. S., Bardeen, C., Gettelman, A., et al. (2021). Evaluation of Cloud and Precipitation Simulations in CAM6 and AM4 Using Observations Over the Southern Ocean. *Earth and Space Science*, *8*(2), e2020EA001241. https://doi.org/10.1029/2020EA001241

Journal of Geophysical Research: Atmospheres

Supporting Information for

Stratocumulus Precipitation Properties over the Southern Ocean Observed from Aircraft during the SOCRATES campaign

L. Kang[1], R. T. Marchand [1], and R. Wood[1]

1 Department of Atmospheric Sciences, University of Washington, Seattle, Washington, USA

Contents of this file

Figures S1 to S11

Introduction

Figure S1 is a schematic showing the typical flight module during the SOCRATES campaign. Figure S2 shows an example of the zenith pointing Doppler velocity fields from RF13 before and after the correction of the zenith pointing data. Figure S3 shows the comparison between mean velocity profiles for nadir pointing and zenith pointing data from RF13 before and after the correcting the zenith pointing data. Figure S4 shows the Mie-to-Rayleigh backscatter ratio. Figure S5 shows probability and cumulative density functions of below-cloud lidar particle linear depolarization ratio (PLDR) for all warm-topped clouds. Figure S6 shows an example case from research flight 10 (RF10) on 2018 Feb. 8th during 02:42-02:52 UTC. Figure S7 shows Z-R relationships derived rain rate. Figure S8-10 shows ZV retrieved the median equivolumetric diameter D_0, precipitation number N_{precip}, and rain rate, respectively, assuming different shape factor μ. Figure S11 shows an example case with radar-lidar retrieved rain rate and rain rate derived from the exponential fitting the retrieved rain rates and extrapolate to the aircraft level.

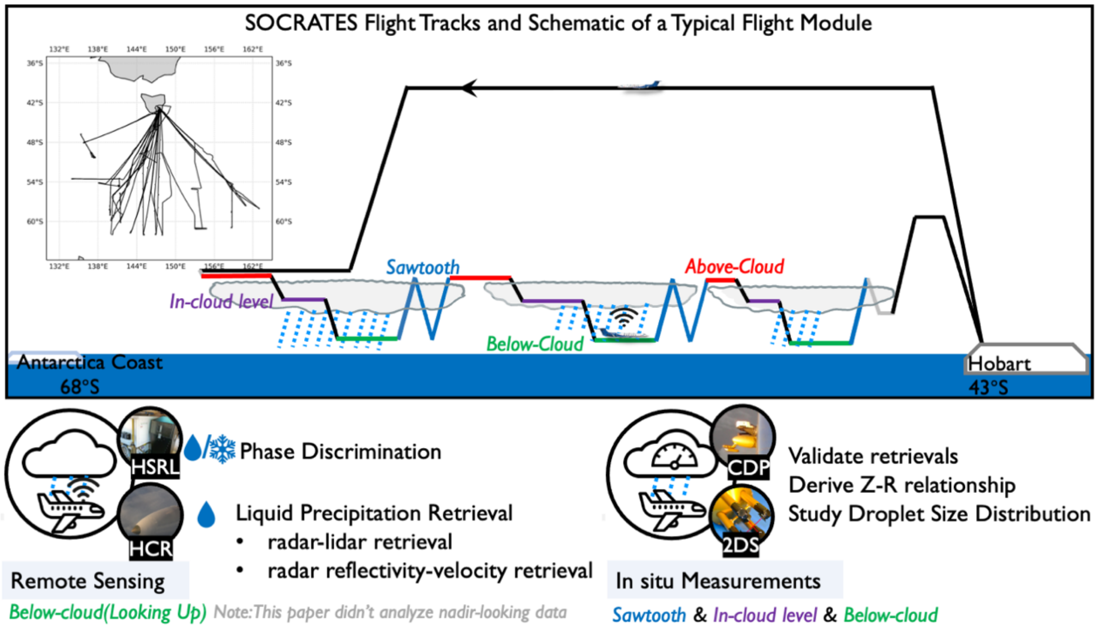

Figure S1. A schematic showing the typical flight module during the SOCRATES campaign (with flight tracks map embedded). The black lines show the flight tracks, with different segments highlighted: below-cloud level legs in green; above-cloud level legs in red; sawtooth legs in blue; in-cloud level legs in purple. The graphics below the schematic summarize the main instruments and how the remote sensing and in situ data from different segments were used in this study.

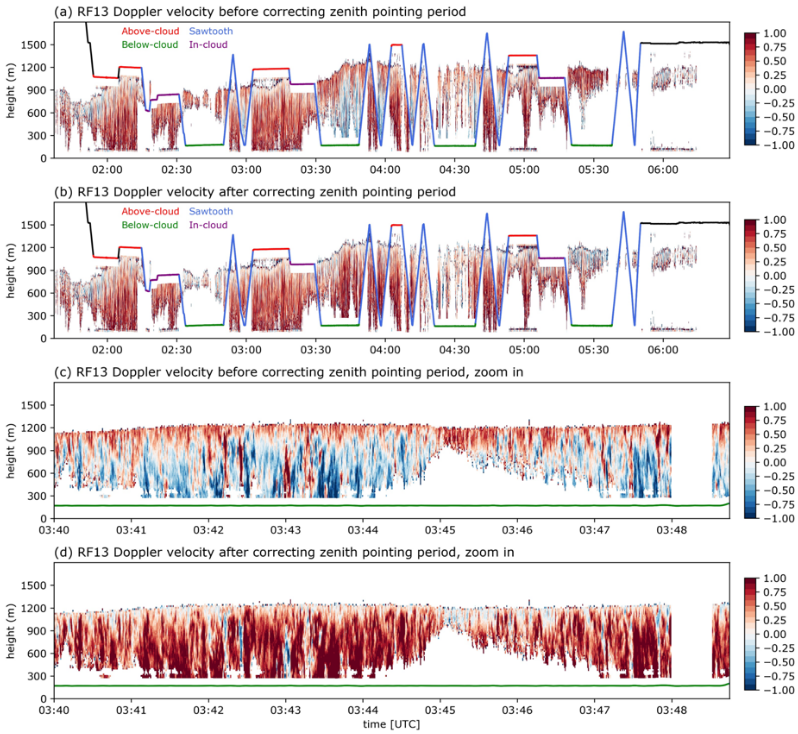

Figure S2. An example of the zenith pointing Doppler velocity fields from RF13 (a) before and (b) after the correction of the zenith pointing data, as well as the zoom in view for zenith-pointing period starting from 03:40 UTC time (c) before and (d) after the correction.

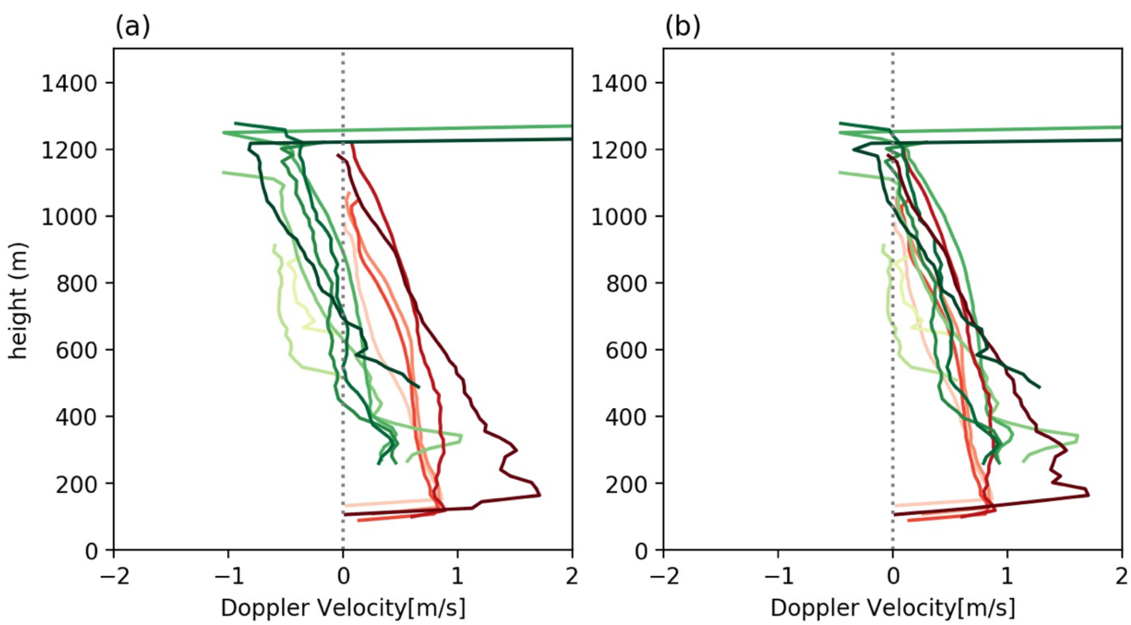

Figure S3. Mean velocity profiles for nadir pointing and zenith pointing data from RF13

(a) before the correcting and (b) after the correcting the zenith pointing data. Here each profile represents the average mean velocity profile averaged over either nadir pointing times (denoted as red) or zenith pointing times (denoted as green). The vertical dashed line represents the 0 m s^{-1} for reference.

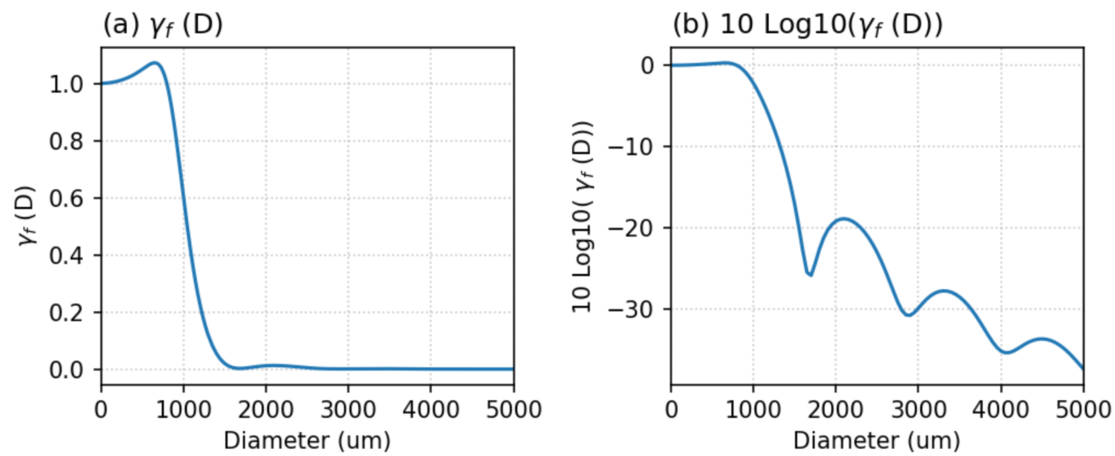

Figure S4. The Mie-to-Rayleigh backscatter ratio (a) $\boldsymbol{\gamma_f(D)}$, and (b) 10 $\boldsymbol{log_{10}(\gamma_f(D))}$. $\boldsymbol{\gamma_f(D)}$ is the ratio of the backscatter efficiency of Mie scattering for W-band (94-GHz), calculated using miepython package that based on Wiscombe(1979), and backscatter efficiency of Rayleigh scattering (Bohren & Huffman, 1983).

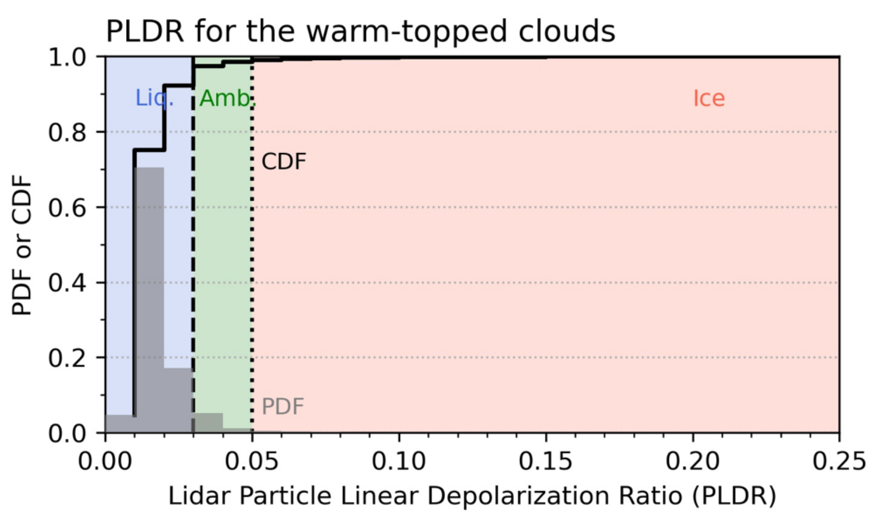

Figure S5. Probability and cumulative density functions of below-cloud lidar particle linear depolarization ratio (PLDR) for all warm-topped clouds (when cloud top temperature >

0°C). To distinguish different precipitation type, liquid precipitation is marked as blue, ice precipitation is marked as red, and ambiguous precipitation is marked as green.

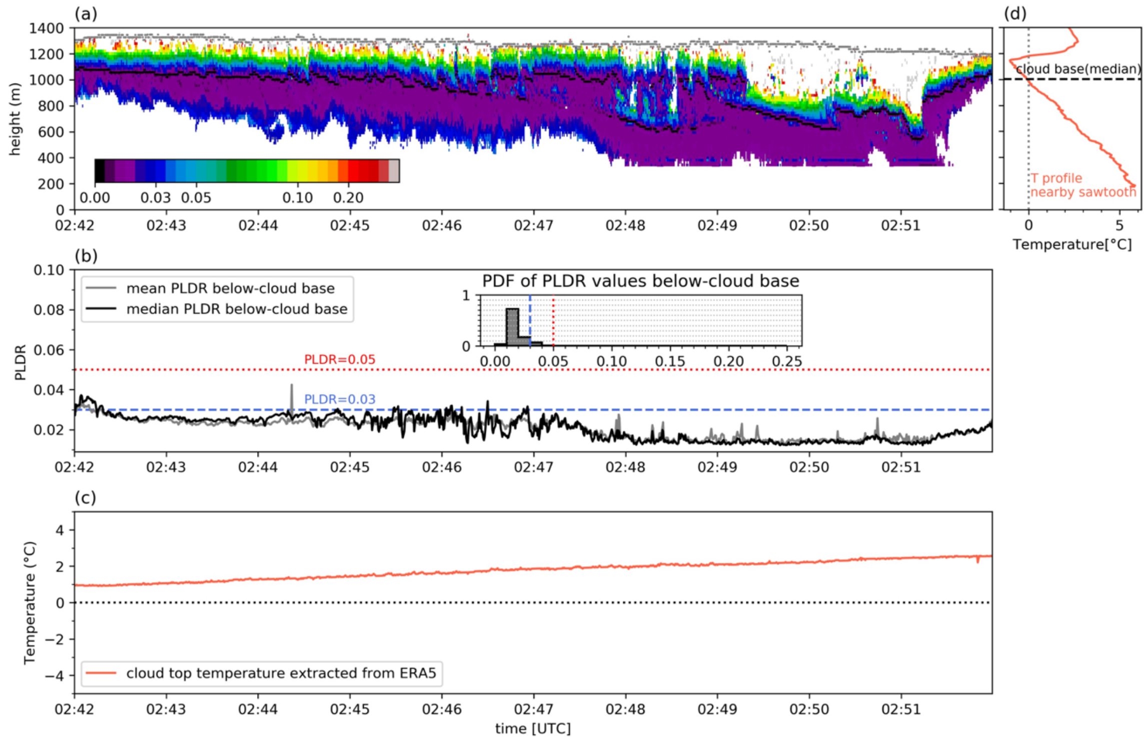

Figure S6. An example case from research flight 10 (RF10) on 2018 Feb. 8th during 02:42-02:52 UTC with (a) lidar particle linear depolarization ratio (PLDR), (b) time series of median PLDR (black) or mean PLDR (grey) values below-cloud base, and the probability density function (PDF) of PLDR values below-cloud base, (c) the cloud top temperature extracted from ERA5 reanalysis data, and (d) temperature profile measured by aircraft from a adjacent sawtooth leg (2018 Feb. 8th during 02:52-02:58 UTC). The grey dotted line in panel c and d represents 0°C for reference. Blue and red line on panel b shows the threshold or PLDR equals 0.03 or 0.05.

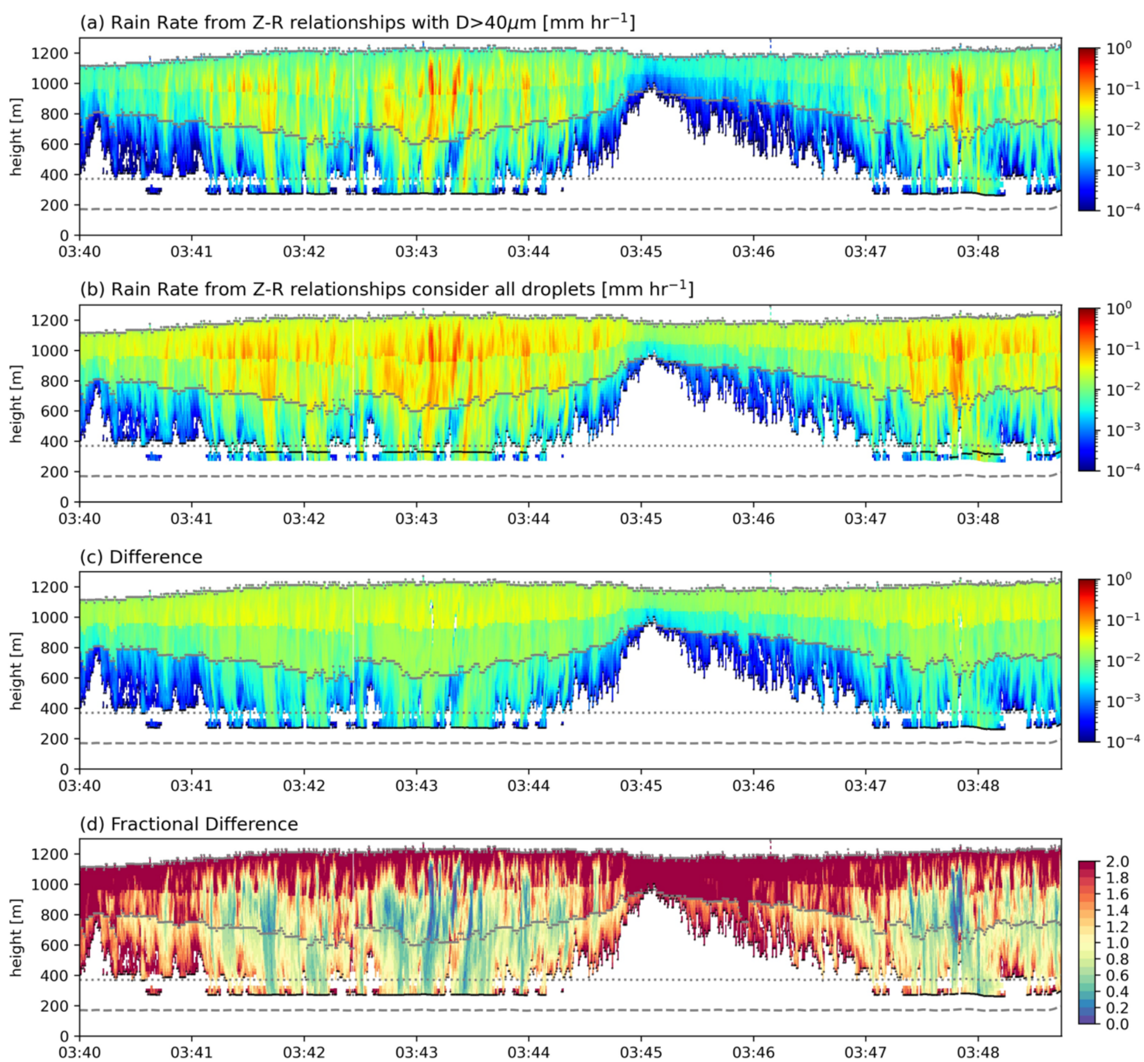

Figure S7. Z-R relationships derived rain rate. Panel a use the Z-R relationships that has D >40 μm cutoff, while Z-R relationships used in panel b does not apply any cutoff, and considers all droplet sizes. Panel c shows difference calculated as $RR_{panel\ b} - RR_{panel\ a}$. Panel d shows the fractional difference calculated as $(RR_{panel\ b} - RR_{panel\ a}) / RR_{panel\ a}$

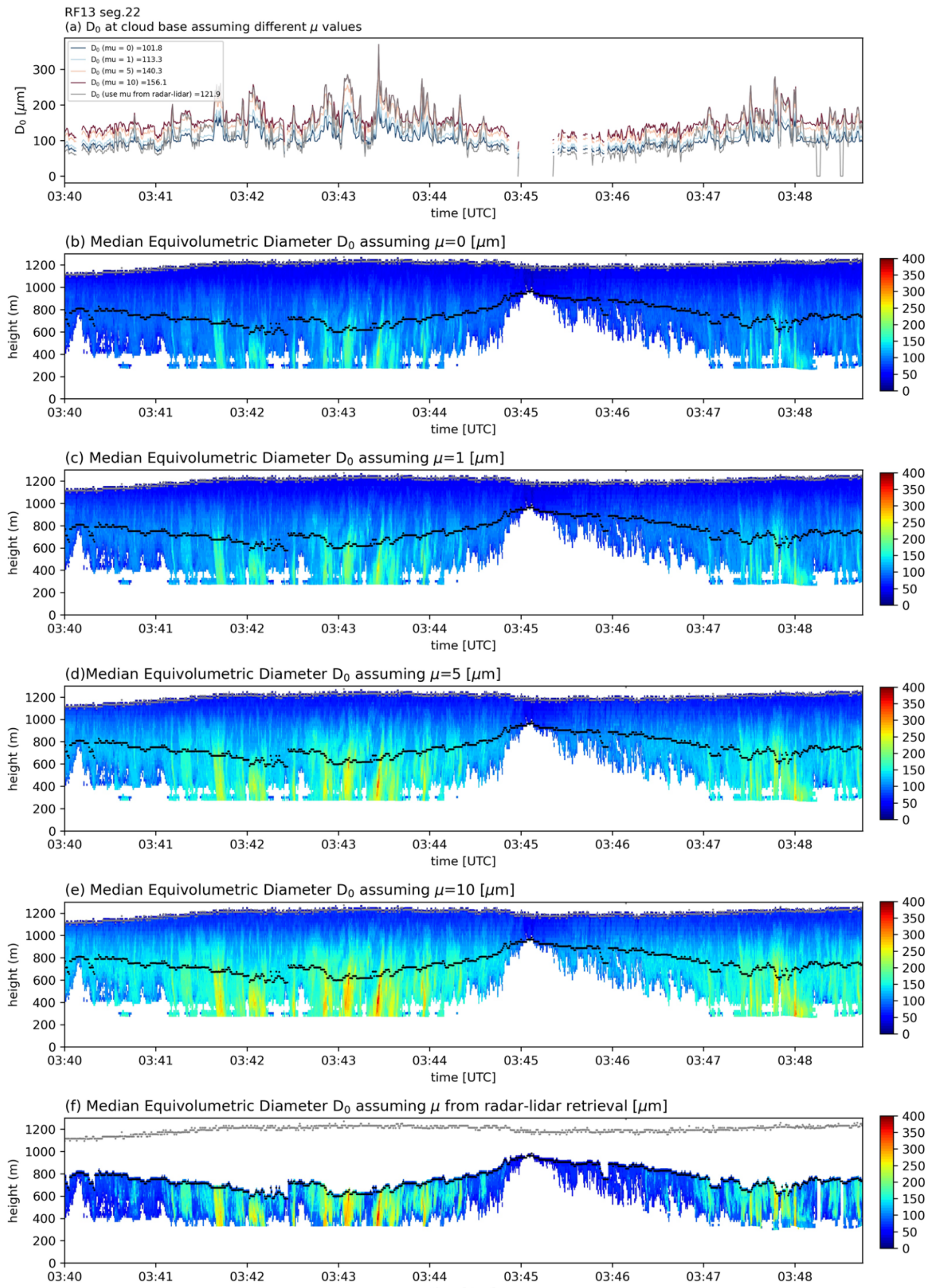

Figure S8. ZV retrieved median equivolumetric diameter D_0 assuming different shape factor $\boldsymbol{\mu}$

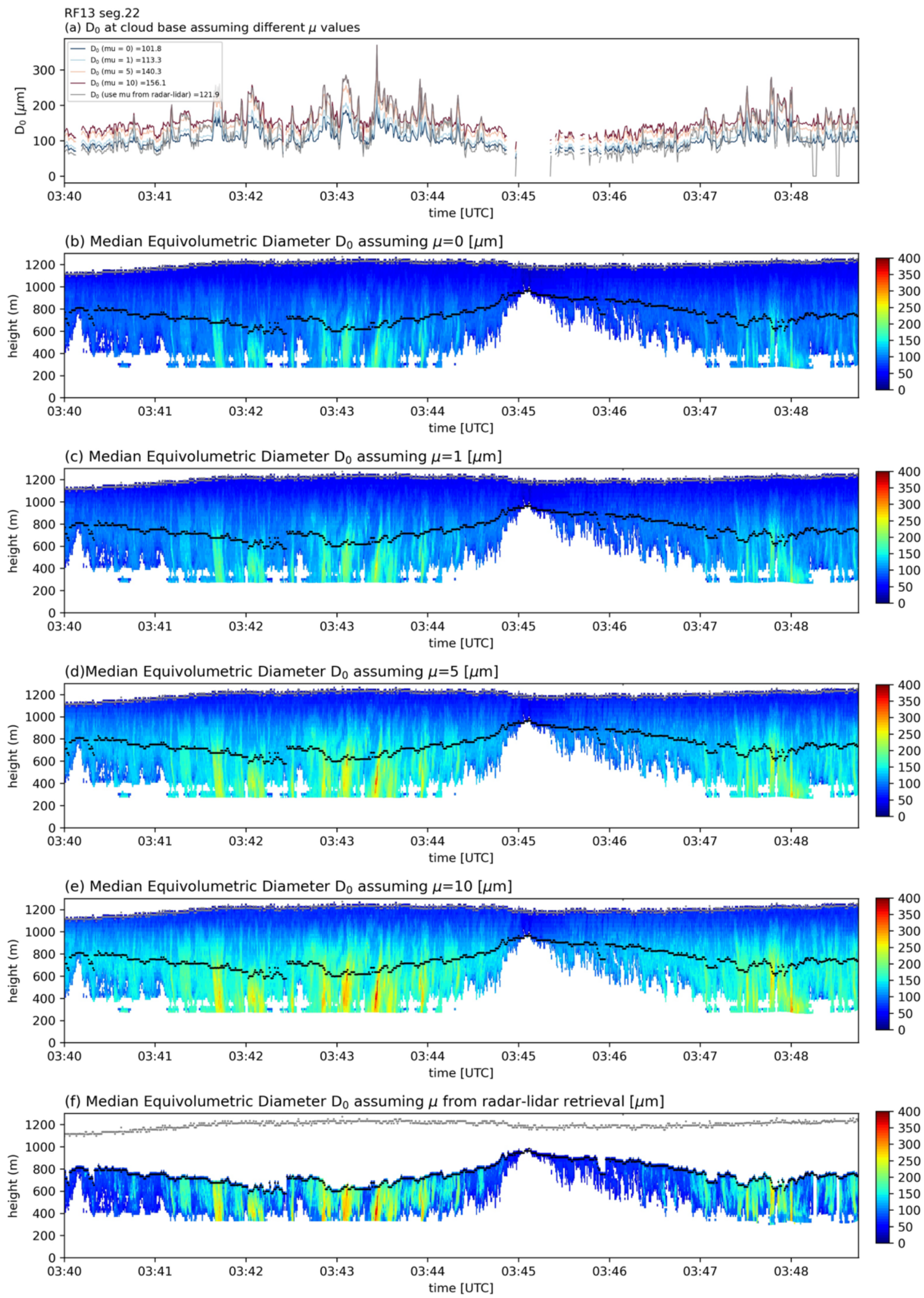

Figure S9. ZV retrieved precipitation number concentration N_{precip} assuming different shape factor $\boldsymbol{\mu}$

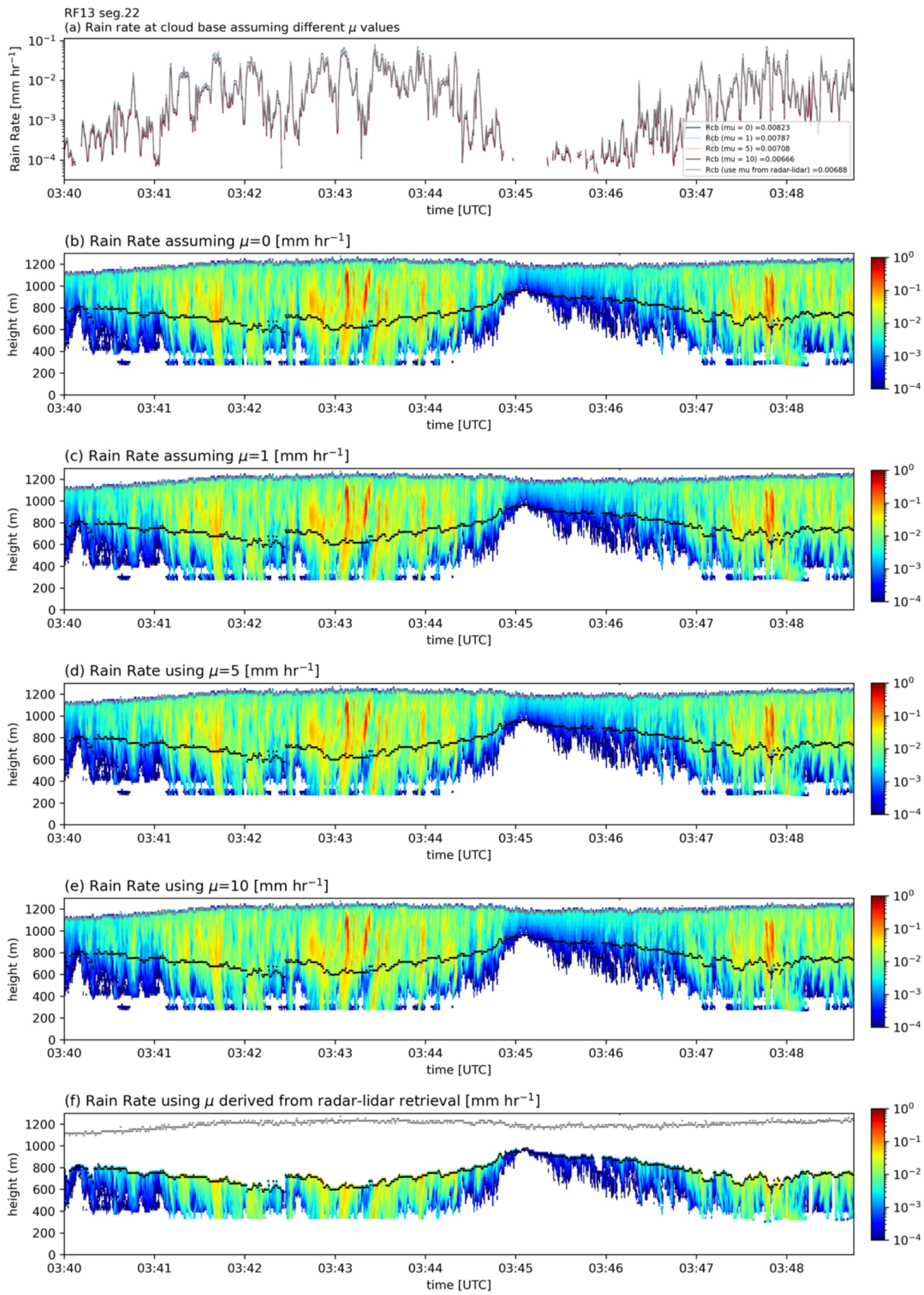

Figure S10. ZV retrieved rain rate assuming different shape factor $\boldsymbol{\mu}$

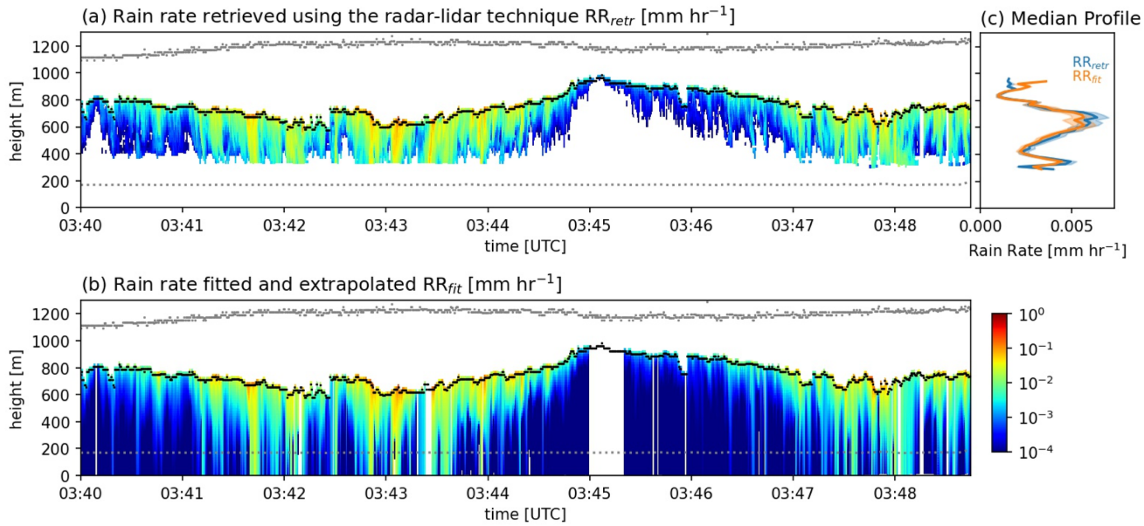

Figure S11. An example case with (a) radar-lidar retrieved rain rate, (b) rain rate derived from the exponential fitting the retrieved rain rates and extrapolate to the aircraft level (marked as the dashed line), and (c) median rain rate profiles of from radar-lidar retrieval (blue) or exponentially fit (orange). In the panel c, the median profiles are calculated over the area where radar-lidar retrieved rain rate are available.